Structural investigations of ytterbium dopant sites and elpasolite nanocrystal structure

Kyle Thompson Kluherz

A dissertation
submitted in partial fulfillment of the
requirements for the degree of

Doctor of Philosophy

University of Washington

2023

Reading Committee:
Daniel R. Gamelin, Chair
James J. De Yoreo, Chair
Scott T. Dunham

Program Authorized to Offer Degree:
Chemistry

University of Washington

Abstract

Structural investigations of ytterbium dopant sites and elpasolite nanocrystal structure

Kyle Thompson Kluherz

Co-Chairs of the Supervisory Committee:
Daniel R. Gamelin
Department of Chemistry

James J. De Yoreo
Department of Chemistry

The relationship between molecular and materials structure and observed properties is a pillar of chemistry and materials science. Understanding the structural character of materials at both the bulk and nanoscale is critical for establishing these relationships, and often requires non-traditional techniques to properly elucidate microstructure and local behavior. This is especially true in the perovskites and elpasolites, which exhibit a wide array of interesting optical, electronic, and magnetic properties, all of which are fine-tunable by minor changes to structure or the addition of dopants. This dissertation describes my research in three studies using X-ray total scattering, pair distribution function analysis, X-ray absorption, and transmission electron microscopy to understand the local structure of lanthanide dopants in cesium lead chloride perovskites and chromium trihalides, and determine the crystal structure and stability of a new iodide elpasolite nanocrystal. These various projects highlight the importance of local structure in leading to the unique optical and magnetic properties of ytterbium-doped cesium lead chloride and chromium trihalides, and the ability of surface free energy to stabilize structures at the nanoscale which are unstable in the bulk. Together these results expand our understanding of the structural origins of optical, magnetic, and

stability properties of these energy-relevant materials.

DEDICATION

To Lee and Tommy Thompson, who have inspired, encouraged, and supported me all my life. I thank God for having given me such wonderful and loving grandparents. May this be a tribute to how deeply you have mattered to me.

ACKNOWLEDGMENTS

A great many people of have helped me along my PhD journey, and I have been very lucky to have them in my life. First and foremost, Daniel and Jim have been excellent co-advisors, and I am very thankful to both of them for their guidance, support, and advice which has led me to this dissertation. Being co-advised in this way was a great boon to my studies, and I thank both Jim and Daniel for how well they worked together in this regard. Thank you to all of my labmates in both groups, who provided a great professional community and group of friends throughout my studies in Seattle and Richland. It has been very nice to have people to chat with around the lab and office, and who appreciate (or at least tolerate) my sense of humor. Sid Creutz was especially helpful as my first lab mentor, and his thorough and careful work continues to set an example for me. Thanks to Matt Smith for telling me to "do it right the first time." Special thanks to Sebastian Mergelsberg, who has probably taught me more technical knowledge than any other single person, and doesn't mind my 'quick questions' that turn into two-hour discussions. Thank you to my good friend Guomin Zhu, who was both my mentor at PNNL and my friend in Richland, especially during the isolating times of the pandemic and quarantine. May we continue to stay in touch throughout our lives. Thanks to Dongsheng Li, Lili Liu, and Libor Kovarik for their instruction and assistance with a variety of TEM techinques. Thank you very much to John Linehan for letting me use your lab space and doing so much to get me setup for synthesis in PSL. I'm very glad there are people like you in chemistry. And to Micah Prange, Sarah Saslow, and all the great folks at PNNL, who taught me so much about research and the scientific life. Thanks to the hard-working and decdicated staff at APS, Leighanne Gallington, Steve Heald, Olaf

Borkiewicz, and Shelly Kelly, who helped me both collect and understand most of the critical data for this dissertation. Back in Seattle, thanks to Ellen Lavoie and the other MAF staff for their help with the MAF user instruments. Thank you to Lochlan Hickok, Ella Miltner and the research stockroom staff, whose assistance with shipping samples was absolutely critical for all my synchrotron work, and whose good humor makes life better for all of us in the department.

Thank you to my friends, near and far, in and out of the chemistry program. To the great community at university presbyterian church, which I have been blessed to be a part of, who have made my life better in so many ways, and been a constant reminder of all the good things happening outside the lab. Thank you for involving me in all the other things life has to offer beyond my studies, and walking with me in these chapters of my life. Thanks also to all my friends in the chemistry program. It has been great to have you all with me on my PhD journey. I knew our first year that I had found a good community here. Thank you to Katya Grishuk, my mentor and friend throughout my education, who never fails to give good advice and help me make good choices. Most of all, thank you to my family, to Joyce and Kendall Kluherz, and Lee Thompson, who have always been there to help, support, and encourage me, to listen to all the things that have happened in my life each week, and loved me all the way.

TABLE OF CONTENTS

LIST OF FIGURES

LIST OF TABLES

Chapter 1

INTRODUCTION: PUTTING THE STRUCTURE IN STRUCTURE-PROPERTY RELATIONSHIPS

1.1 Overview

My PhD research has focused primarily on the structural characterization of perovskite semiconductor materials, mainly employing X-ray total scattering and Pair Distribution Function (PDF) analysis, Extended X-ray Absorption Fine Structure (EXAFS), and transmission electron microscopy (TEM). Through the combination of these techniques with other characterization methods as well as materials syntheses I have deeply investigated dopant site structure in Yb^{3+}-doped $CsPbCl_3$ perovskites and determined the structure of Cs_2AgBiI_6 elpasolites. These and related perovskite materials constitute a class of semiconductor ionic solids of great interest for photovoltaics, optoelectronics, X-ray detection, lighting, and other applications. Understanding the nature of their structure-property relationships is critical for achieving these applications. That is where my work lies: probing the detailed local structure of materials at dopant sites and at the nanoscale; putting the structure in structure-property relationships.

1.2 Perovskite semiconductor materials

The perovskites represent a large class of ionic solids with the structure ABX_3, where A is a monovalent cation, B is a divalent cation, and X is a monovalent anion. They derive their name from a class of minerals exhibiting this structure and stoichiometry, first discovered

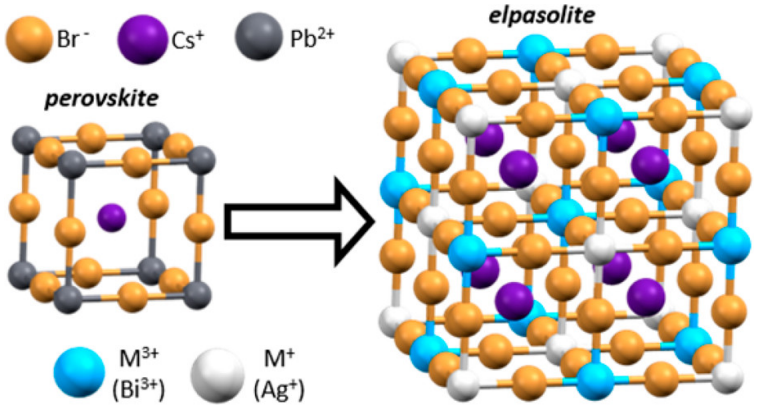

Figure 1.1: Comparison of the perovskite structure (left) and the double perovskite or elpasolite structure (right). The elpasolite structure replaces a single B^{2+} cation with alternating B^{+} and B^{3+} cations, thus doubling the dimensions of the unit cell. Source: Creutz et al.[5]

in 1840 and named after a Russian mineralogist, Lev Perovski, by German mineralogist Gustav Rose.[1] Among this large family of materials there are several subclasses which are generally considered to be perovskites, ranging from traditional perovskites with the exact stoichiometry and cubic structure through several variations on the structural symmetry and stoichiometry.[2,3] Among the traditional perovskites, the lead halide perovskites in particular have recently garnered great interest due to their many outstanding properties, enjoying a great renewal of interest since their original report in 1893.[4] I shall discuss these in detail in 1.2.1. Another related subclass are the double perovskites or elpasolites. These materials substitute a single B-site cation for two B-site cations, one monovalent, the other trivalent, as seen in Figure 1.1. The elpasolites offer several attractive properties, particularly greater stability and lower toxicity, discussed in 1.2.2.

1.2.1 $CsPbX_3$ (X = Cl,Br,I) Perovskites

The lead halide perovskites in general exhibit numerous advantageous properties, including high photoluminescence quantum yields, narrow emission linewidths, broad tunability, ease of synthesis, and suitability as hosts for a variety of dopants. All-inorganic cesium lead halides in particular have higher stabilities than their mixed organic-inorganic counterparts, and have been extensively studied in both the bulk and nanoscale.[2,6–24] Colloidal $CsPbX_3$ (X = Cl, Br, I) perovskite nanocrystals have attracted a great deal of interest since their discovery in 2015 due to their bright, narrow emission, high photoluminesence quantum yields, tunable band gap, defect tolerance, and suitability for doping with transition metals and lanthanides.[7,18,25–32] These properties, some of which are showcased in Figure 1.2, make them highly attractive for solar cell and optics applications, including as down-converters in novel solar-cell architectures, as lasers, as emitters for LEDs, and even as X-ray detectors.[33,34] An understanding of the structure of these materials and their dopant sites is particularly useful for providing insight into their unique structure-property relationships.

Numerous studies have investigated the structural nature of the lead halide perovskites.[35–38] In bulk, their structure has been reported numerous times as cubic (Pm3m), with corner-sharing lead halide octahedra which dominate the structure of the bandgap. However, in the nanocrystals a more complex picture has gradually emerged as more precise techniques have been applied to study these materials. Initially, their structure was believed to be identical to the bulk,[25], but further investigation revealed it to be a lower-symmetry orthorhombic (Pnma) structure, likely the result of nanocrystal surface relaxation.[38–40] This investigation received greater attention as electronic structure modeling efforts progressed, driving the need for a precise understanding of structure in these nanocrystals.[41] Furthermore, diverse post-synthetic structural engineering may be performed on these materials (Figure 1.3), further complicating the structural picture. However, understanding the structure of nanoparticles is a challenging question, and requires the application of techniques beyond

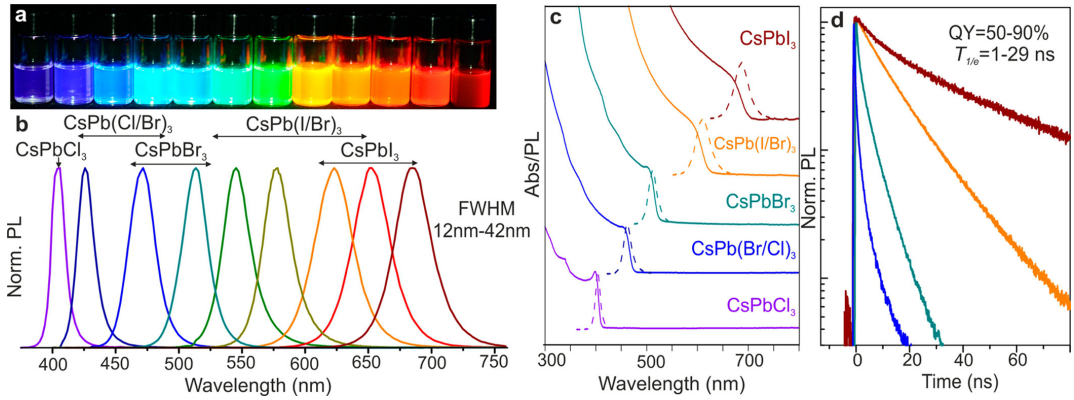

Figure 1.2: Optical properties of $CsPbX_3$ (X = Cl, Br, I) perovskite nanocrystals, from the first report of these materials by Protesescu et al.[25]. **(a)** Colloidal solutions in toluene, excited by UV lamp. **(b)** Representative PL spectra. **(c)** Absorption and PL spectra. **(d)** Time-resolved PL decays for samples in (c).

traditional XRD to properly probe the local variations in structure which routinely occur in these materials.[40,42–44]

To better investigate the structure of lead halide perovskite nanocrystals, two main techniques have emerged: X-ray total scattering for atomic Pair Distribution Function (PDF) analysis, and Transmission Electron Microscopy. Both are powerful techniques with the ability to probe local structural features which are not observable in traditional X-ray diffraction. A PDF study of $CsPbBr_3$ nanocrystals by Bertolotti et al.[42] (Figure 1.4) was able to discern the presence of multiple nanotwin domains within single nanocrytals via a careful analysis of minor peaks in the total scattering and several features in the PDF. A further study by Cottingham and Brutchey[44] observed changes to the orthorhombic distortion of $CsPbX_3$ (X = Cl, Br, I) NCs underlying the changes observable in the average structure. This allowed for a greatly improved understanding of the order-disorder transitions in these materials and the evolution of their structure during heating.

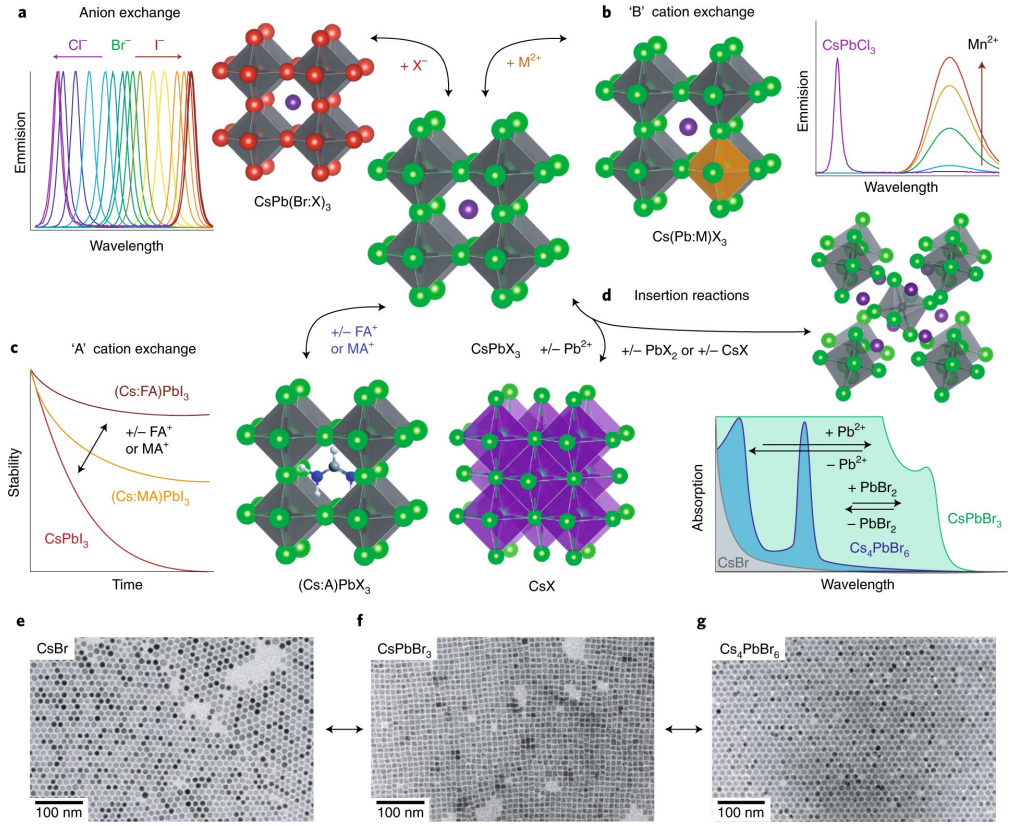

Figure 1.3: The diverse post-synthetic structural engineering of lead halide perovskites. This can be done via multiple routes: (a) anion exchange, (b) B-site cation exchange, (c) A-site cation exchange, and (d) insertion reactions. (e-g) NCs obtained from transformation between different compounds.[3]

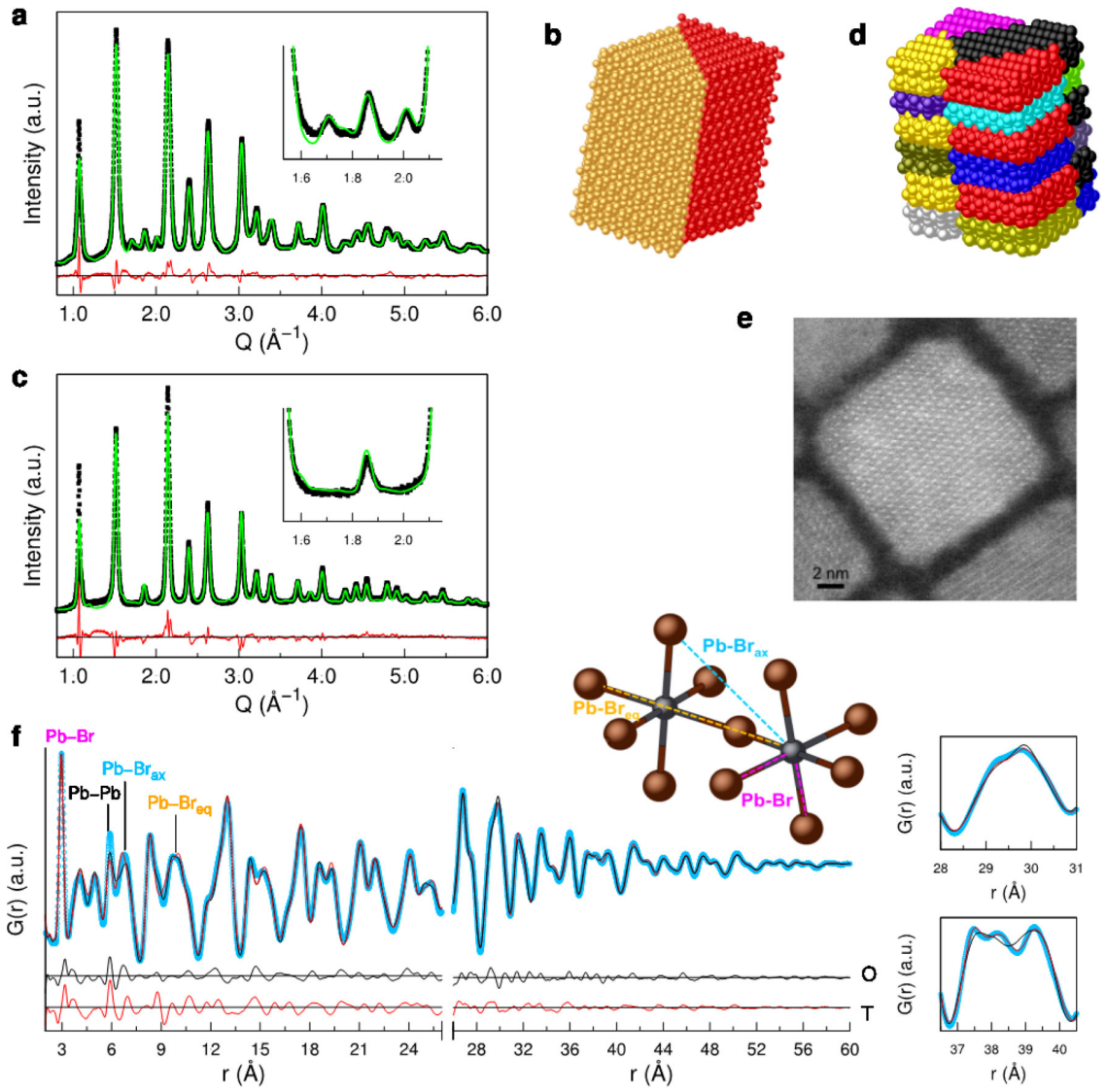

Figure 1.4: Using X-ray synchrotron data and PDF to identify the presence of nanotwin domains in $CsPbBr_3$ nanocrystals. By careful analysis of their scattering data at 298 K (a) and 410 K (c) in conjunction with models (b,d) and PDF analysis (f), Bertolotti et al.[42] were able show evidence of cubic nanotwins with dynamic disorder in $CsPbBr_3$ nanocrystals leading to an overall orthorhombic structure. (e) shows a HR-STEM image of the $CsPbBr_3$ nanocrystals.

Further insight into the local structure of individual nanocrystals has been provided by the use of high-resolution transmission electron microscopy (HRTEM).[45] This technique is particularly advantageous because it can be used to study individual nanocrystals instead of an ensemble, and thus can be highly complimentary to the aforementioned X-ray scattering techniques. Additionally, TEM can provide a wealth of information about the sample, including particle size, morphology, crystal structure, and even composition via emitted X-rays. However, collecting high-quality HRTEM data was initially very challenging due to the extensive damage to these materials caused primarily by capture of electrons from the electron beam.[46–49] This required extensive efforts on the part of the research community to overcome, but via a combination of careful sample preparation and cleaning, high accelerating voltages, and low electron doses, high-quality HRTEM images were acquired by numerous groups.[40,50–61] Figure 1.5 shows an example of the use of HR-STEM to investigate polar-solvent induced structural changes to $CsPbI_3$ nanocrystals.[57]

A good example of nanocrystal structure investigation is the recent use by Brennan et al.[40] of HRTEM in combination with FFT of images. This was employed (Figure 1.6) to distinguish between cubic and orthorhombic structures for individual nanocrystals. By comparing FFTs of HRTEM images of single $CsPbBr_3$ NCs with cubic and orthorhombic simulations, they were able to find the coexistence of both lattices within single nanocrystals. It should be mentioned this was a particularly impressive study due to the great degree of similarity between these structures, with only subtle differences being distinguishable in their inverse space. This result is especially interesting as it highlights the ability of TEM to do what no other technique can: conclusively reveal structural features coming from a single nanocrystal rather than from multiple different structures within the same nanocrystal population.

Another powerful technique for the investigation of local structure in both molecules, clusters, and crystals is Extended X-ray Absorption Fine Structure (EXAFS). This technique

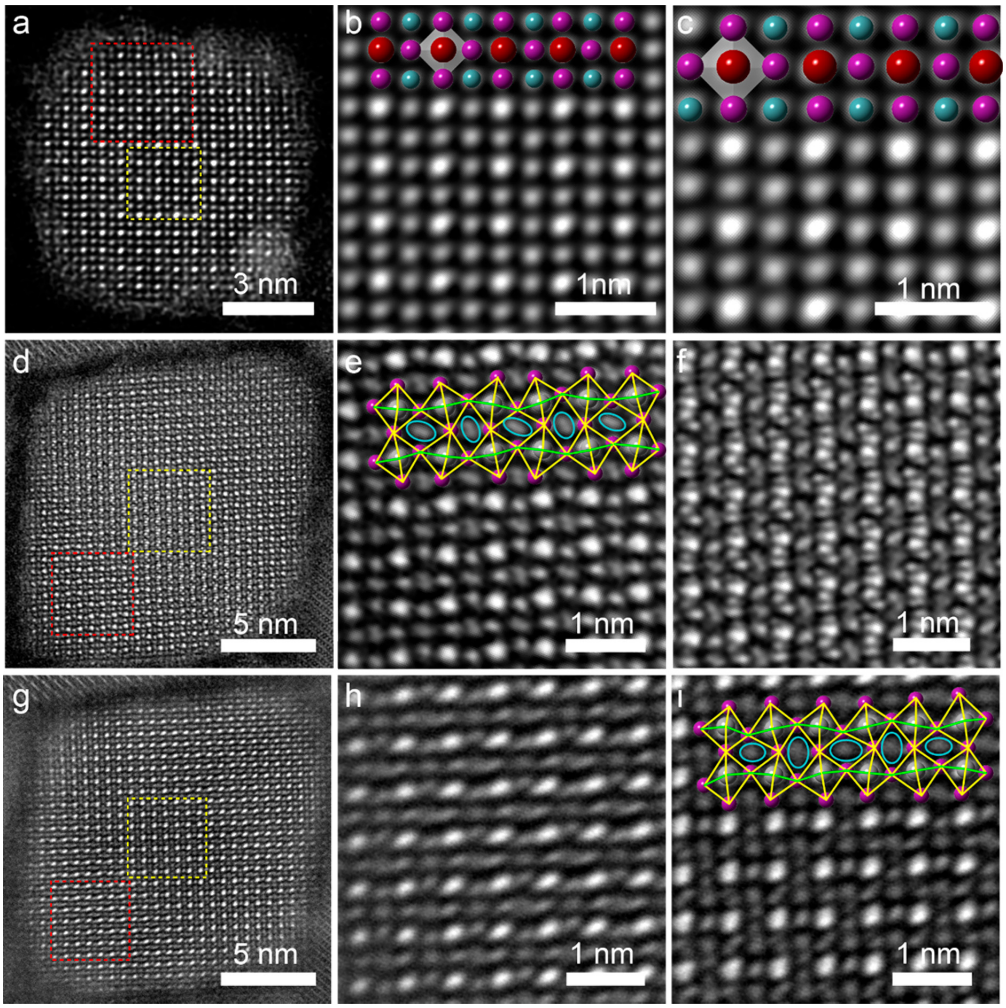

Figure 1.5: HAADF-STEM images of polar solvent induced lattice distortion of the $CsPbI_3$ nanocrystal lattice. (a) HAADF image of pristine $CsPbI_3$.(b,c) Zoom-in views of the outer and inner areas shown in (a). (d-i) HAADF images of ethanol-exposed $CsPbI_3$ nanocrystals, showing distortion of the lattice caused by exposure to the polar solvent. Source: Sun et al.[57]

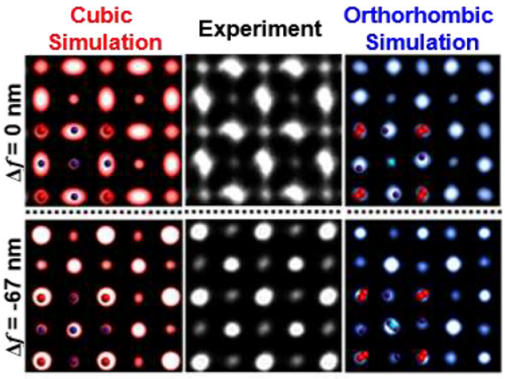

Figure 1.6: Example use of TEM to study the structure of individual $CsPbBr_3$ nanocrystals by Brennan et al.[40]. By comparing HRTEM images with cubic and orthorhombic simulations, the authors were able to determine the coexistence of both lattices within single nanocrystals.

is a subset of X-ray absorption which focuses specifically on the area of the spectrum resulting from transitions from core states to continuum states.[62,63] Analysis of this region provides insight into the local structure around the absorber atom, and is especially powerful when combined with structural models that can be used to fit the data. EXAFS has been applied for many years on a wide variety of materials,[64–68] and is complimentary to other techniques such as XRD or PDF which provide more general structural information.[69–71] Numerous studies have employed EXAFS to investigate the local structure of both the host lattice and of dopants in the lead halide perovskites,[72–75] as well as size variation[76] and gradients in core/shell nanocrystals.[77] Chapter 2 focuses on my own work combining these techniques to probe local structure in Yb^{3+}:$CsPbCl_3$ perovskites.

1.2.2 Elpasolites

The great success of the lead halide perovskites has motivated explorations into related classes of materials, particularly in search of lower toxicity and greater stability while maintaining some or all of their advantageous optical and electronic properties. One such class of materials investigated are the double perovskites or elpasolites, wherein a single divalent B-site cation is replaced with a monovalent cation (M^+) and a trivalent cation (M^{3+}): $AM^+M^{3+}X_6$. This doubles the size of the unit cell along each dimension, hence the name 'double perovskites'. While these materials have not been able to successfully reproduce the outstanding optical properties of the lead halides perovskites, they have been found to exhibit superior stability to both water and temperature, while generally being composed of less toxic materials, bismuth being especially prominent.[14,78–89] Additionally, the bismuth elpasolites exhibit high carrier mobilities, long carrier lifetimes, and large extinction coefficients, making them well-suited to photovoltaics applications.[81–83,87,90]

In addition to the elpasolites, there are several related classes of materials shown in Figure 1.7, including the $A_3B_2X_9$ and A_3BX_6 (A^+, B^{3+}, X^-) which exist in the same phase space and are often observed as the primary transformation or decomposition products of the elpasolite materials. While they have also been investigated for their optoelectronic properties, these related materials generally do not exhibit the same level of utility as the elpasolites, likely a result of their different band structure.[5,83,84,87]

While elpasolites have been reported in both the bulk and nanoscale, here I focus specifically on the nanocrystals. There are relatively few reports of elpasolite nanocrystals, and they may be divided into two general categories based on their synthesis method: hot-injection[5,92–95] and anti-solvent recrystallization.[96–100] Both have been shown to yield nanocrystals of consistent size and morphology, but the hot-injection method tends to yield superior crystal quality.[78,83,89] Among these reports, the Gamelin group previously reported both a hot-injection procedure and an anion-exchange method employing the trimethylsilane

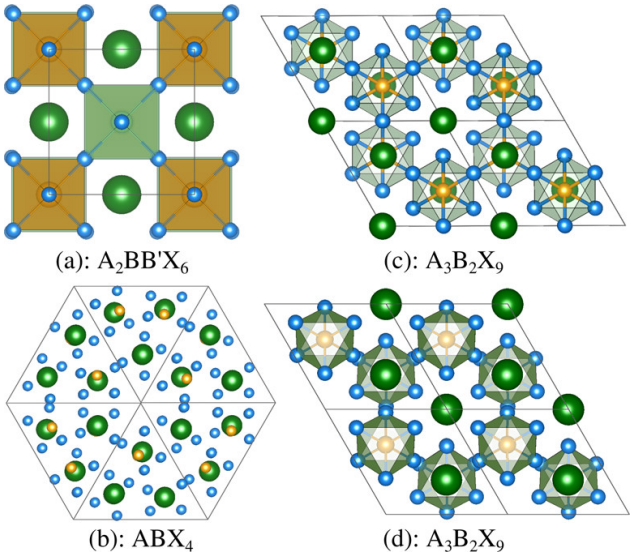

Figure 1.7: Elpasolites and related structures: (a) Double perovskites, (b) 2-D perovskites, (c) 0-D perovskites and (d) polymorphs.[91]

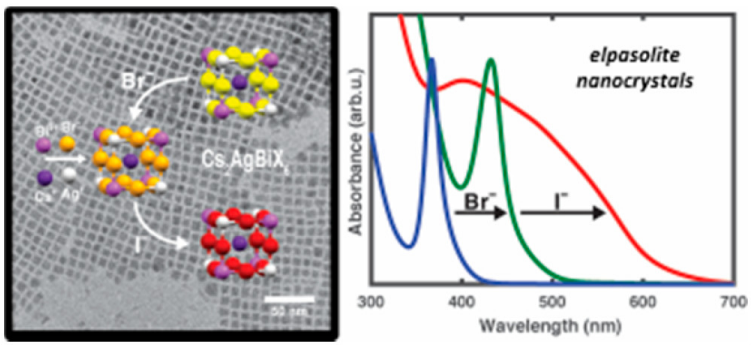

Figure 1.8: Synthesis and anion exchange of Cs_2AgBiX_6 (X = Cl, Br, I) nanocrystals by Creutz et al..[5]

halides to achieve the synthesis of Cs_2AgBiX_6 (X = Cl, Br, I)[5]. Figure 1.8 shows an overview of this method, including the progression of the absorbance from Cl to Br to I. While these nanocrystals do not exhibit observable emission at room temperature, via low-temperature measurements (20 K) they were able to investigate their opto-electronic properties. Most importantly for my research, they were able to access a previously unreported material in $CsAgBiI_6$ via this anion exchange process, one of the first forays into the iodide elpasolite phase space. Chapter 3 of my thesis will focus on the structural investigations which have resulted from this discovery.

1.3 Structural Characterization Techniques

During the course of my PhD, I have learned a variety of techniques for the characterization of compounds and materials, including absorption, photoluminescence, X-ray diffraction, electron microscopy, X-ray absorption, X-ray scattering, and inductively-coupled plasma mass spectrometry. However, I have specialized in several which require a substantial knowledge investment to use to their full potential: PDF, EXAFS, and TEM. In this section I will provide a basic overview of each of these techniques, including some of their applications.

1.3.1 Atomic Pair Distribution Function (PDF)

X-ray total scattering and the atomic pair distribution function (PDF) are excellent techniques for the study of a variety of structures, phases, and phenomena, including dopant sites, nanomaterials,[101,102] exsolved phases, amorphous materials,[70,103,104] nucleation and crystallization in solution,[105,106] surface structure,[107] and even gases.[108–111] This technique is especially powerful because it collects all the scattering information in the sample, not just the Bragg diffraction peaks like in a standard XRD experiment. The addition of diffuse scattering, orders of magnitude less intense than the Bragg peaks, allows for far greater sensitivity to minority species and non-periodic features. Thanks to the intensities and energies of syn-

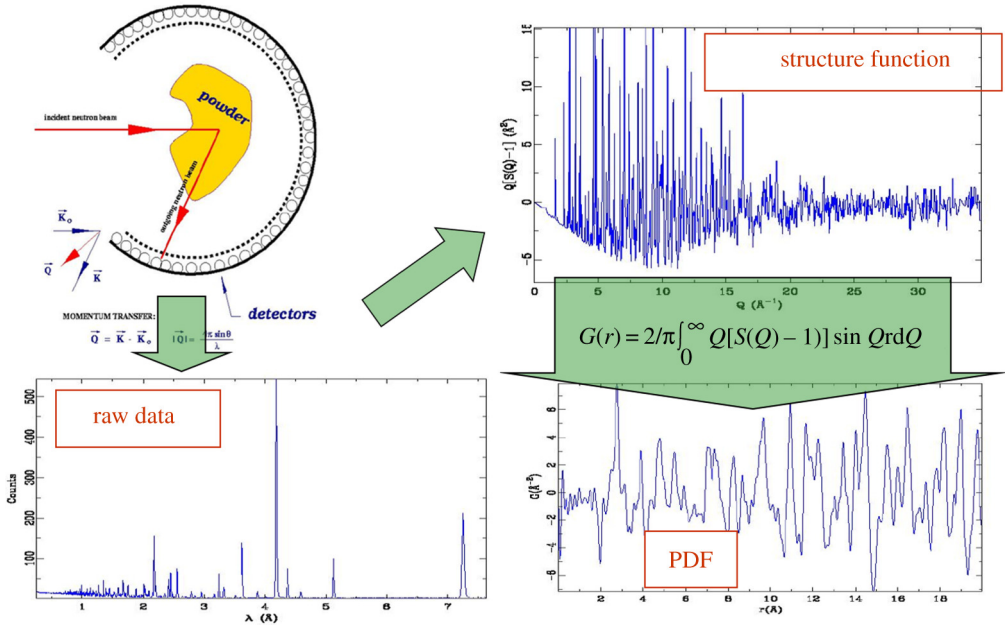

Figure 1.9: Overview of the process for obtaining atomic pair distribution functions. Powder or nanoparticle scattering data are collected, integrated, then corrected and normalized to yield the structure function. A specific Fourier transform then yields the PDF. Source: Billinge[115]

chrotron sources, it can even detect carbon-carbon bonds from solvents and surface ligands, something which I have needed to account for in some of my measurements. It is this broad sensitivity that makes PDF especially useful in the field of nanomaterials, as it can be used as a probe of surface structure as well as defects and dopants in the material. Several studies have reported PDF for the investigation of the structure of nanocrystals,[42,44,112–114] and were able to provide insight that would not be possible using other techniques.

Originally developed by Debye, Zernike, and Prins in the early 20th century,[115–118] the PDF is a method for extracting real-space structure information from X-ray total scattering data via a Fourier transform method. A good introduction to the technique and its history

can be found in Billinge[115] and Proffen et al.[111]. In brief, integrated data are background subtracted, corrected, and normalized to yield the structure function, which is then Fourier transformed to the PDF. An overview of this process from Billinge[115] is shown in Figure 1.9. There are subtle intricacies in each step, but that is the general method. The PDF itself can be very straightforward to interpret, as it is essentially the likelihood of finding an atom pair at a particular distance from one another in the sample, whether crystalline or not. There are three main regions in the PDF: short-, medium-, and long-range order, corresponding (unsurprisingly) to increasing distance in r. In the short-range regime, there are few enough atom pairs present at such distances that peaks may be assigned to individual atom pairs, and shoulders or new peaks are especially indicative of additional phases or defects. Analysis of the PDF and comparison with calculated PDFs for different models allows for a wide range of applications studying structure, local dopant sites, defects, and exsolved phases in bulk and nanomaterials.

In my PhD research, I have primarily leveraged PDF for the study of dopant sites in $CsPbCl_3$, along with studying the structure and stability of Cs_2AgBiI_6 nanocrystals. Both of theses studies (see Chapters 2 and 3, respectively) highlight the utility of this technique for studying properties that are otherwise inaccessible by more traditional structural techniques.

1.3.2 EXAFS

X-ray Absorption Fine Structure (XAFS) or Extended X-ray Absorption Fine Structure (EXAFS) (the two terms may generally be used interchangeably, although I have seen a few sources that use XAFS as a broader category than EXAFS) is a specific type of X-ray absorption spectroscopy (XAS), focusing on the extended fine structure region of the X-ray absorption spectrum.[62,63,119] Figure 1.10 shows an example X-ray absorption spectrum for K edge absorption, showing the XANES and EXAFS regions of the spectrum along with the electronic transitions responsible for the signal in each region. X-ray absorption

transitions originate from core electrons of the absorbing atom, and are labeled based on the principle quantum number of the orbital they originate from: K for n=1, L for n=2, M for n=3, etc. I found Evans[119] chapter 2 to have a good explanation of this notation. The majority of XAS data measure either the K or the L edges.[62,63,119,120] In the XANES region, electrons undergo dipole (LaPorte) allowed transitions to valence states of the absorbing atom, often including a sharp 'white line' from a highly allowed resonant transition to the LUMO or valence band of the material.[62] This allows XANES to be especially useful in determining the oxidation state of the absorbing atom, as each oxidation state will have a unique energy for the absorption edge. Pre-edge features in the XANES can provide additional information about the hybridization of the absorbing atom.[119] In the EXAFS region, electrons undergo similar transitions to the continuum region, completely escaping the absorbing atom as an electron wave. It is this free electron wave which allows EXAFS to probe the local environment of the absorbing atom.[62,63,119] The electron wave scatters off the neighboring atoms and returns to the absorber, creating an interference pattern whose features are determined by the interactions resulting from all nearby scatterers. In practice this is highly dominated by the nearest neighbor and second nearest neighbor species, allowing specific information about the local structure to be extracted from the EXAFS data. Equation 1.1 shows the general EXAFS equation. Several excellent derivations[62] and detailed explanations[62,63,119] can be found in the literature, but I will give a short explanation.

$$\chi(k) = \sum_j S_o^2 N_j \frac{|f_j(k)|}{kR_j^2} \sin(2kR_j + 2\delta_c + \phi) e^{-2R_j/\lambda(k)} e^{-2\sigma_j^2 k^2} \tag{1.1}$$

Essentially the EXAFS equation is a sum of all the scattering paths from each of the neighboring scattering atoms, as a function of interatomic distance (R_j), number of scattering atoms (N_j), and the wavevector (k). This is modulated by the amplitude (S_o), mean free path, and several other factors to account for the various scattering behaviors which are possible but do not lead to an EXAFS signal.

EXAFS has many uses for determining the local structure or environment in both molecules

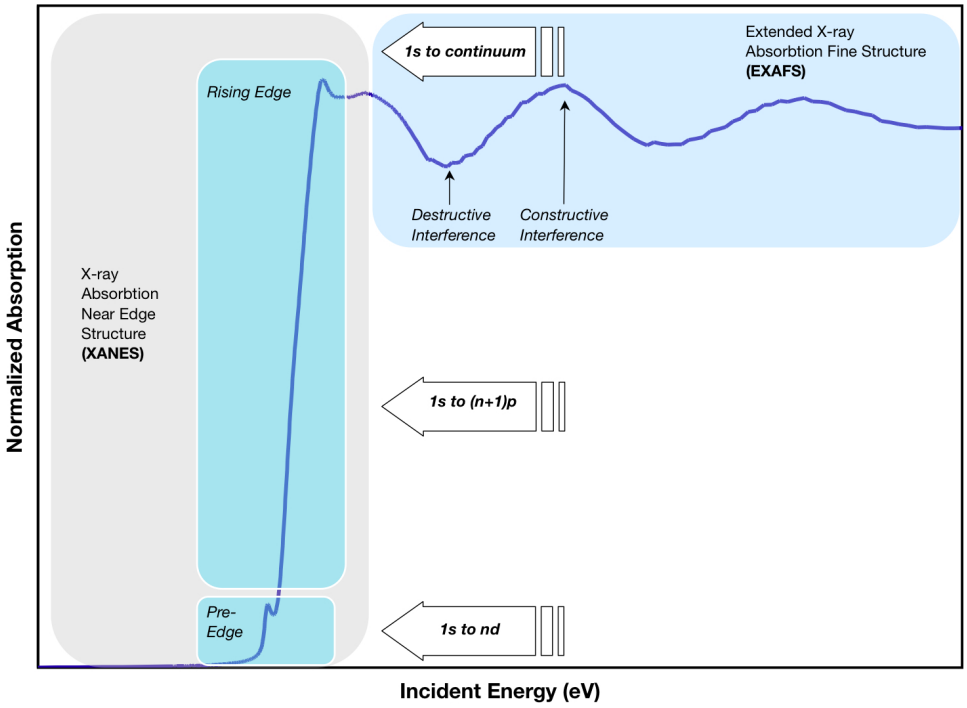

Figure 1.10: Regions of X-ray absorption data, including XANES and EXAFS, and the electronic transitions for a K edge absorption spectrum. Source: Munzarin at English Wikipedia via Wikimedia commons.

and materials, such as the analysis of dopants,[64,66,71,73,121,122] local structure,[64,66,67,71,73,76,120,122–126] bonding,[66,71] and strain[76,120,122,127–131] in materials, molecules, and solutions. It is a powerful technique for such investigations, and can provide information unavailable to traditional XRD or other structural techniques. Its ability to be site-specific, depending on the absorber atom, is especially useful for answering questions regarding geometry and strain around different points in crystals and compounds, as well as dopant-induced defects. However, robust interpretation of EXAFS does require good structural models to use for fitting the data, as qualitative interpretation of EXAFS provides only limited information. It is thus best used when some information is already known about the system, and so specific structural or chemical questions can be answered by the application of EXAFS. In my PhD research, I have primarily used EXAFS in the study of dopant site structure of Yb^{3+} in perovskite ($CsPbCl_3$) and chromium (CrX_3) lattices.

1.3.3 Transmission Electron Microscopy (TEM)

Another highly useful technique for the study of nanomaterials is transmission electron microscopy (TEM). TEM is *the* go-to technique for identifying the size, morphology, distribution, and crystallinity of nanomaterial samples, due to its ability to directly observe each of these properties on the individual nanocrystal level. It is also, by far, my favorite instrument to use. Being able to see, actually *see*, nanocrystals and even atoms is incredibly exciting!

TEM is a highly technical technique, with a large number of interactions occurring between the electron beam and the sample, each of which can be used to provide information about the sample. Fundamentally, it is an electron scattering experiment, as the incident beam of electrons is elastically and inelastically scattered by the atoms in the sample (as well as the grid). This gives rise to numerous phenomena: the direct beam, diffracted electrons, high-angle scattering, X-ray emissions, and others. Each of these contains some information about the sample, but the main ones of interest are the scattered electrons, which are

used for imaging (either bright field, dark field, or high-angle annular dark field (HAADF)) and electron diffraction, and the emitted X-rays, which are used for element identification via EDX. Williams and Carter[132] provides an excellent introduction to the technique and its many applications, and I would highly recommend their books for anyone interested in learning more about TEM.

In terms of nanomaterials, the main utility of TEM is in its ability to distinguish individual nanoparticles, and, for aberration-corrected instruments, single atomic columns within individual nanoparticles. This allows for many useful applications, including size-property relationships, study of core-shell structure and interfaces,[133] nanocrystal superlattice packing,[134–136] and many others. These applications are greatly expanded by the use of *in situ* TEM,[50,137,138] where particle growth,[139] morphology, orientation,[140] and other properties can be monitored in real time during heating,[141–143] in gas, or in liquid, depending on the type of *in situ* holder used. Numerous studies have pioneered these techniques for the study of a wide variety of systems, including recently perovskite nanomaterials,[144] and they are likely to see further use in the future as detailed investigation into challenging questions about structure, nucleation and growth, and morphology of nanoparticle systems receive further interest. I have spent extensive time using both *ex situ* and *in situ* TEM during my PhD, although the main project I was working on ultimately did not work out due to beam-induced contamination issues.

1.4 Probing Structure at the Nanoscale

While challenging, investigating structure at the nanoscale is rapidly becoming a critical technique for understanding a variety of nanomaterial and material systems, from dopants and defects in bulk perovskite semiconductors to the structure of individual nanocrystals of $CsPbBr_3$ or Cs_2AgBiI_6. My PhD research has focused on the synthesis and characterization of these materials, and their investigation using PDF, EXAFS, and TEM in order to better

understand the unique nature of structure at the nanoscale. These three techniques in particularly can be highly complimentary: EXAFS and PDF are both ensemble techniques, with PDF giving information about all the structural elements of a sample while EXAFS provides local structure information around specific elements. TEM in turn provides information on the nanocrystals scale, from hundreds or thousands of nanocrystals at a time down to single nanocrystals and even, in a few cases, single atom dopants.[145] Together these techniques allow for a near-comprehensive understanding of local structure, and stand to make great inroads in our fundamental understanding of a variety of critical materials systems.

BIBLIOGRAPHY

[1] Rose, G. Ueber einige neue Mineralien des Urals. *Journal fur Praktische Chemie* **1840**, *19*, 459–468.

[2] Mitzi, D. B.; B. Mitzi, D. Introduction: Perovskites. *Chemical Reviews* **2019**, *119*, 3033–3035.

[3] Akkerman, Q. A.; Rainò, G.; Kovalenko, M. V.; Manna, L. Genesis, challenges and opportunities for colloidal lead halide perovskite nanocrystals. *Nature Materials* **2018**, *17*, 394–405.

[4] Wells, H. L. Über die Cäsium- und Kalium-Bleihalogenide. *Zeitschrift für anorganische Chemie* **1893**, *3*, 195–210.

[5] Creutz, S. E.; Crites, E. N.; De Siena, M. C.; Gamelin, D. R. Colloidal Nanocrystals of Lead-Free Double-Perovskite (Elpasolite) Semiconductors: Synthesis and Anion Exchange To Access New Materials. *Nano Letters* **2018**, *18*, 1118–1123.

[6] Li, W.; Wang, Z.; Deschler, F.; Gao, S.; Friend, R. H.; Cheetham, A. K. Chemically diverse and multifunctional hybrid organic-inorganic perovskites. *Nature Reviews Materials* **2017**, *2*, 16099.

[7] Kovalenko, M. V.; Protesescu, L.; Bodnarchuk, M. I. Properties and potential optoelectronic applications of lead halide perovskite nanocrystals. *Science* **2017**, *358*, 745–750.

[8] Goetz, K. P.; Taylor, A. D.; Paulus, F.; Vaynzof, Y. Shining Light on the Photoluminescence Properties of Metal Halide Perovskites. *Advanced Functional Materials* **2020**, 1910004.

[9] Xiang, W.; Tress, W. Review on Recent Progress of All-Inorganic Metal Halide Perovskites and Solar Cells. *Advanced Materials* **2019**, *31*, 1902851.

[10] Wang, X.; Lian, X.; Zhang, Z.; Gao, H. Could Nanocomposites Continue the Success of Halide Perovskites? *ACS Energy Letters* **2019**, *4*, 1446–1454.

[11] Almutlaq, J.; Yin, J.; F. Mohammed, O.; M. Bakr, O. The Benefit and Challenges of Zero-Dimensional Perovskites. *The Journal of Physical Chemistry Letters* **2018**, *9*, 4131–4138.

[12] Xu, Q.; Yang, D.; Lv, J.; Sun, Y.-Y.; Zhang, L. Perovskite Solar Absorbers: Materials by Design. *Small Methods* **2018**, *2*, 1700316.

[13] Pradhan, N. Journey of Making Cesium Lead Halide Perovskite Nanocrystals: What's Next. *The Journal of Physical Chemistry Letters* **2019**, *10*, 5847–5855.

[14] Igbari, F.; Wang, Z.; Liao, L. Progress of Lead-Free Halide Double Perovskites. *Advanced Energy Materials* **2019**, *9*, 1803150.

[15] Zhou, Y.; Zhao, Y. Chemical stability and instability of inorganic halide perovskites. *Energy & Environmental Science* **2019**, *12*, 1495–1511.

[16] Stoumpos, C. C.; Kanatzidis, M. G. The Renaissance of Halide Perovskites and Their Evolution as Emerging Semiconductors. *Accounts of Chemical Research* **2015**, *48*, 2791–2802.

[17] McDonald, C.; Ni, C.; Maguire, P.; Connor, P.; Irvine, J. T. S.; Mariotti, D.; Svrcek, V. Nanostructured Perovskite Solar Cells. *Nanomaterials* **2019**, *9*, 1481.

[18] Dey, A. et al. State of the Art and Prospects for Halide Perovskite Nanocrystals. *ACS Nano* **2021**, *15*, 10775–10981.

[19] Sytnyk, M.; Deumel, S.; Tedde, S. F.; Matt, G. J.; Heiss, W. A perspective on the bright future of metal halide perovskites for X-ray detection. *Applied Physics Letters* **2019**, *115*.

[20] Huang, H.; Bodnarchuk, M. I.; Kershaw, S. V.; Kovalenko, M. V.; Rogach, A. L. Lead Halide Perovskite Nanocrystals in the Research Spotlight: Stability and Defect Tolerance. *ACS Energy Letters* **2017**, *2*, 2071–2083.

[21] Chouhan, L.; Ghimire, S.; Subrahmanyam, C.; Miyasaka, T.; Biju, V. Synthesis, optoelectronic properties and applications of halide perovskites. *Chemical Society Reviews* **2020**, *49*, 2869–2885.

[22] de Weerd, C.; Gregorkiewicz, T.; Gomez, L. All-Inorganic Perovskite Nanocrystals: Microscopy Insights in Structure and Optical Properties. *Advanced Optical Materials* **2018**, *6*, 1800289.

[23] Miyasaka, T.; Kulkarni, A.; Kim, G. M.; Öz, S.; Jena, A. K. Perovskite Solar Cells: Can We Go Organic-Free, Lead-Free, and Dopant-Free? *Advanced Energy Materials* **2020**, *10*, 1902500.

[24] Service, R. F. Perovskite LEDs begin to shine. *Science* **2019**, *364*, 918–918.

[25] Protesescu, L.; Yakunin, S.; Bodnarchuk, M. I.; Krieg, F.; Caputo, R.; Hendon, C. H.; Yang, R. X.; Walsh, A.; Kovalenko, M. V. Nanocrystals of Cesium Lead Halide Perovskites (CsPbX3 , X = Cl, Br, and I): Novel Optoelectronic Materials Showing Bright Emission with Wide Color Gamut. *Nano Letters* **2015**, *15*, 3692–3696.

[26] He, L.; Meng, J.; Feng, J.; Liu, X.; Zhang, H. Unveiling the mechanism of rare earth doping to optimize the optical performance of the CsPbBr 3 perovskite. *Inorganic Chemistry Frontiers* **2020**, *7*, 4669–4676.

[27] Yang, H.; Zhang, Y.; Pan, J.; Yin, J.; Bakr, O. M.; Mohammed, O. F. Room-Temperature Engineering of All-Inorganic Perovskite Nanocrsytals with Different Dimensionalities. *Chemistry of Materials* **2017**, *29*, 8978–8982.

[28] ten Brinck, S. et al. Surface Termination, Morphology, and Bright Photoluminescence of Cesium Lead Halide Perovskite Nanocrystals. *ACS Energy Letters* **2016**, *1*, 1266–1272.

[29] Wu, Y.; Li, X.; Zeng, H. Highly Luminescent and Stable Halide Perovskite Nanocrystals. *ACS Energy Letters* **2019**, *4*, 673–681.

[30] Seth, S.; Ahmed, T.; De, A.; Samanta, A. Tackling the Defects, Stability, and Photoluminescence of CsPbX 3 Perovskite Nanocrystals. *ACS Energy Letters* **2019**, *4*, 1610–1618.

[31] Kovalenko, M. V.; Bodnarchuk, M. I. Lead Halide Perovskite Nanocrystals: From Discovery to Self-assembly and Applications. *CHIMIA International Journal for Chemistry* **2017**, *71*, 461–470.

[32] Ling, X.; Yuan, J.; Ma, W. The Rise of Colloidal Lead Halide Perovskite Quantum Dot Solar Cells. *Accounts of Materials Research* **2022**, *3*, 866–878.

[33] Chen, H.; Li, Y.; Zhao, B.; Ming, J.; Xue, D. Nanocrystals of metal halide perovskites and their analogues as scintillators for x-ray detection. *Nano Futures* **2022**, *6*, 012001.

[34] Chaudhary, B.; Kshetri, Y. K.; Kim, H. S.; Lee, S. W.; Kim, T. H. Current status on

synthesis, properties and applications of CsPbX3 (X = Cl, Br, I) perovskite quantum dots/nanocrystals. *Nanotechnology* **2021**,

[35] MØLLER, C. K. Crystal Structure and Photoconductivity of Cæsium Plumbohalides. *Nature* **1958**, *182*, 1436–1436.

[36] Hutton, J.; Nelmes, R. J. Journal of Physics C : Solid State Physics Related content High-resolution studies of cubic perovskites by High-resolution studies of cubic perovskites by elastic neutron diffraction 11 : SrTiO ,, KMnF ,, RbCaF , and. *Journal of Physics C: Solid State Physics* **1981**, *14*, 1713–1736.

[37] López, C. A.; Abia, C.; Alvarez-Galván, M. C.; Hong, B. K.; Martínez-Huerta, M. V.; Serrano-Sánchez, F.; Carrascoso, F.; Castellanos-Gómez, A.; Fernández-DÍaz, M. T.; Alonso, J. A. Crystal Structure Features of CsPbBr3 Perovskite Prepared by Mechanochemical Synthesis. *ACS Omega* **2020**, *5*, 5931–5938.

[38] Linaburg, M. R.; McClure, E. T.; Majher, J. D.; Woodward, P. M. Cs1-xRbxPbCl3 and Cs1-xRbxPbBr3 Solid Solutions: Understanding Octahedral Tilting in Lead Halide Perovskites. *Chemistry of Materials* **2017**, *29*, 3507–3514.

[39] Goubet, N.; Legrand, L.; Barisien, T.; Bernardot, F.; Ramade, J.; Andriambariarijaona, L. M.; Steinmetz, V.; Goubet, N.; Legrand, L.; Barisien, T.; Bernardot, F.; Testelin, C.; Lhuillier, E.; Bramati, A.; Chamarro, M. Fine structure of excitons and electron–hole exchange energy in polymorphic CsPbBr 3 single nanocrystals. *Nanoscale* **2018**, *10*, 6393–6401.

[40] Brennan, M. C.; Kuno, M.; Rouvimov, S. Crystal Structure of Individual CsPbBr 3 Perovskite Nanocubes. *Inorganic Chemistry* **2019**, *58*, 1555–1560.

[41] Pradhan, N. Why Do Perovskite Nanocrystals Form Nanocubes and How Can Their

Facets Be Tuned? A Perspective from Synthetic Prospects. *ACS Energy Letters* **2021**, *6*, 92–99.

[42] Bertolotti, F.; Protesescu, L.; Kovalenko, M. V.; Yakunin, S.; Cervellino, A.; Billinge, S. J. L.; Terban, M. W.; Pedersen, J. S.; Masciocchi, N.; Guagliardi, A. Coherent Nanotwins and Dynamic Disorder in Cesium Lead Halide Perovskite Nanocrystals. *ACS Nano* **2017**, *11*, 3819–3831.

[43] Bertolotti, F.; Vivani, A.; Ferri, F.; Anzini, P.; Cervellino, A.; Bodnarchuk, M. I.; Nedelcu, G.; Bernasconi, C.; Kovalenko, M. V.; Masciocchi, N.; Guagliardi, A. Size Segregation and Atomic Structural Coherence in Spontaneous Assemblies of Colloidal Cesium Lead Halide Nanocrystals. *Chemistry of Materials* **2022**, *34*, 594–608.

[44] Cottingham, P.; Brutchey, R. L. Depressed Phase Transitions and Thermally Persistent Local Distortions in CsPbBr3 Quantum Dots. *Chemistry of Materials* **2018**, *30*, 6711–6716.

[45] Chen, S.; Zhang, Y.; Zhao, J.; Mi, Z.; Zhang, J.; Cao, J.; Feng, J.; Zhang, G.; Qi, J.; Li, J.; Gao, P. Transmission electron microscopy of organic-inorganic hybrid perovskites: myths and truths. *Science Bulletin* **2020**, *65*, 1643–1649.

[46] Dang, Z.; Shamsi, J.; Palazon, F.; Imran, M.; Akkerman, Q. A.; Park, S.; Bertoni, G.; Prato, M.; Brescia, R.; Manna, L. In Situ Transmission Electron Microscopy Study of Electron Beam-Induced Transformations in Colloidal Cesium Lead Halide Perovskite Nanocrystals. *ACS Nano* **2017**, *11*, 2124–2132.

[47] Dang, Z.; Shamsi, J.; Akkerman, Q. A.; Imran, M.; Bertoni, G.; Brescia, R.; Manna, L. Low-Temperature Electron Beam-Induced Transformations of Cesium Lead Halide Perovskite Nanocrystals. *ACS Omega* **2017**, *2*, 5660–5665.

[48] Dang, Z.; Dhanabalan, B.; Castelli, A.; Dhall, R.; Bustillo, K. C.; Marchelli, D.; Spirito, D.; Petralanda, U.; Shamsi, J.; Manna, L.; Krahne, R.; Arciniegas, M. P. Temperature-Driven Transformation of CsPbBr 3 Nanoplatelets into Mosaic Nanotiles in Solution through Self-Assembly. *Nano Letters* **2020**, *20*, 1808–1818.

[49] Deng, Y.-H. Perovskite decomposition and missing crystal planes in HRTEM. *Nature* **2021**, *594*, E6–E7.

[50] Fan, Z.; Zhang, L.; Baumann, D.; Mei, L.; Yao, Y.; Duan, X.; Shi, Y.; Huang, J.; Huang, Y.; Duan, X. In Situ Transmission Electron Microscopy for Energy Materials and Devices. *Advanced Materials* **2019**, *31*, 1–22.

[51] Fernández-Delgado, N.; Herrera, M.; Delgado, F. J.; Tavabi, A. H.; Luysberg, M.; Dunin-Borkowski, R. E.; Juárez-Pérez, E. J.; Hames, B. C.; Mora-Sero, I.; Suárez, I.; Martínez-Pastor, J. P.; Molina, S. I. Structural characterization of bulk and nanoparticle lead halide perovskite thin films by (S)TEM techniques. *Nanotechnology* **2019**, *30*, 135701.

[52] Funk, H.; Shargaieva, O.; Eljarrat, A.; Unger, E. L.; Koch, C. T.; Abou-Ras, D. In Situ TEM Monitoring of Phase-Segregation in Inorganic Mixed Halide Perovskite. *The Journal of Physical Chemistry Letters* **2020**, *11*, 4945–4950.

[53] Griffiths, J. T. et al. Effect of Size on the Luminescent Efficiency of Perovskite Nanocrystals. *ACS Applied Energy Materials* **2019**, *2*, 6998–7004.

[54] Liu, W.; Zheng, J.; Shang, M.; Fang, Z.; Chou, K.-c.; Yang, W.; Hou, X. X.-m. X.; Wu, T. Electron-beam irradiation-hard metal-halide perovskite nanocrystals. *Journal of Materials Chemistry A* **2019**, *7*, 10912–10917.

[55] Song, K.; Liu, J.; Lu, N.; Qi, D.; Qin, W. Direct atomic-scale imaging of a screw

dislocation core structure in inorganic halide perovskites. *Physical Chemistry Chemical Physics* **2022**, *24*, 6393–6397.

[56] Song, K.; Liu, L.; Zhang, D.; Hautzinger, M. P.; Jin, S.; Han, Y. Atomic-Resolution Imaging of Halide Perovskites Using Electron Microscopy. *Advanced Energy Materials* **2020**, *1904006*, 1904006.

[57] Sun, J.-K. et al. Polar Solvent Induced Lattice Distortion of Cubic CsPbI 3 Nanocubes and Hierarchical Self-Assembly into Orthorhombic Single-Crystalline Nanowires. *Journal of the American Chemical Society* **2018**, *140*, 11705–11715.

[58] Yu, Y.; Zhang, D.; Kisielowski, C.; Dou, L.; Kornienko, N.; Bekenstein, Y.; Wong, A. B.; Alivisatos, A. P.; Yang, P. Atomic Resolution Imaging of Halide Perovskites. *Nano Letters* **2016**, *16*, 7530–7535.

[59] Zhang, D.; Zhu, Y.; Liu, L.; Ying, X.; Hsiung, C. E.; Sougrat, R.; Li, K.; Han, Y. Atomic-resolution transmission electron microscopy of electron beam–sensitive crystalline materials. *Science* **2018**, *359*, 675–679.

[60] Zhang, M.; Li, H.; Jing, Q.; Lu, Z.; Wang, P. Atomic Characterization of Byproduct Nanoparticles on Cesium Lead Halide Nanocrystals Using High-Resolution Scanning Transmission Electron Microscopy. *Crystals* **2017**, *8*, 2.

[61] Zhou, Y.; Sternlicht, H.; Padture, N. P. Transmission Electron Microscopy of Halide Perovskite Materials and Devices. *Joule* **2019**, *3*, 1–21.

[62] Calvin, S. *XAFS for Everyone*; CRC Press, 2013.

[63] Newville, M. Fundamentals of XAFS. *Reviews in Mineralogy and Geochemistry* **2014**, *78*, 33–74.

[64] Anjana, R.; Jayaraj, M. K.; Yadav, A. K.; Jha, S. N.; Bhattacharyya, D. Investigating the evolution of local structure around Er and Yb in ZnO:Er and ZnO:Er, Yb on annealing using X-ray absorption spectroscopy. *Journal of Applied Physics* **2018**, *123*.

[65] Rao, L.; Zhang, Z.; Friese, J. I.; Ritherdon, B.; Clark, S. B.; Hess, N. J.; Rai, D. Oligomerization of chromium(III) and its impact on the oxidation of chromium(III) by hydrogen peroxide in alkaline solutions. *Journal of the Chemical Society, Dalton Transactions* **2002**, 267–274.

[66] Lawniczak-Jablonska, K.; Iwanowski, R. J.; Golacki, Z.; Traverse, A.; Pizzini, S.; Fontaine, A.; Winter, I.; Hormes, J. Local electronic structure of ZnS and ZnSe doped by Mn, Fe, Co, and Ni from x-ray-absorption near-edge structure studies. *Physical Review B* **1996**, *53*, 1119–1128.

[67] Yamamoto, T.; Tanaka, T.; Matsuyama, T.; Funabiki, T.; Yoshida, S. XAFS study of the structure of the silica-supported ytterbium oxide catalyst. *Solid State Communications* **1999**, *111*, 137–142.

[68] Saslow, S. A.; Kerisit, S. N.; Varga, T.; Mergelsberg, S. T.; Corkhill, C. L.; Snyder, M. M. V.; Avalos, N. M.; Yorkshire, A. S.; Bailey, D. J.; Crum, J.; Asmussen, R. M. Immobilizing Pertechnetate in Ettringite via Sulfate Substitution. *Environmental Science & Technology* **2020**, *54*, 13610–13618.

[69] Kluherz, K. T.; Mergelsberg, S. T.; Sommer, D. E.; Roh, J. Y. D.; Saslow, S. A.; Biner, D.; Krämer, K. W.; Dunham, S. T.; De Yoreo, J. J.; Gamelin, D. R. Defect structure in quantum-cutting Yb3+-doped CsPbCl 3 perovskites probed by x-ray absorption and atomic pair distribution function analysis. *Physical Review Materials* **2022**, *6*, 074601.

[70] Prange, M. P.; Mergelsberg, S. T.; Kerisit, S. N. Ab Initio Molecular Dynamics Simulations of Amorphous Calcium Carbonate: Interpretation of Pair Distribution Function and X-ray Absorption Spectroscopy Data. *Crystal Growth & Design* **2021**, *21*, 2212–2221.

[71] Lawniczak–Jablonska, K.; Libera, J.; Iwanowski, R. EXAFS determination of local atomic structure of selected transition metals in CdSe matrix. *Journal of Alloys and Compounds* **1999**, *286*, 89–92.

[72] Yong, Z.-J.; Guo, S.-Q.; Ma, J.-P.; Zhang, J.-Y.; Li, Z.-Y.; Chen, Y.-M.; Zhang, B.-B.; Zhou, Y.; Shu, J.; Gu, J.-L.; Zheng, L.-R.; Bakr, O. M.; Sun, H.-T. Doping-Enhanced Short-Range Order of Perovskite Nanocrystals for Near-Unity Violet Luminescence Quantum Yield. *Journal of the American Chemical Society* **2018**, *140*, 9942–9951.

[73] Ma, J.-P.; Chen, Y.-M.; Zhang, L.-M.; Guo, S.-Q.; Liu, J.-D.; Li, H.; Ye, B.-J.; Li, Z.-Y.; Zhou, Y.; Zhang, B.-B.; Bakr, O. M.; Zhang, J.-Y.; Sun, H.-T. Insights into the local structure of dopants, doping efficiency, and luminescence properties of lanthanide-doped CsPbCl 3 perovskite nanocrystals. *Journal of Materials Chemistry C* **2019**, *7*, 3037–3048.

[74] Bi, C.; Wang, S.; Li, Q.; Kershaw, S. V.; Tian, J.; Rogach, A. L. Thermally Stable Copper(II)-Doped Cesium Lead Halide Perovskite Quantum Dots with Strong Blue Emission. *The Journal of Physical Chemistry Letters* **2019**, *10*, 943–952.

[75] Ma, J.; Yao, Q.; McLeod, J. A.; Chang, L.-Y.; Pao, C.-W.; Chen, J.; Sham, T.-K.; Liu, L. Investigating the luminescence mechanism of Mn-doped CsPb(Br/Cl) 3 nanocrystals. *Nanoscale* **2019**, *11*, 6182–6191.

[76] Shinde, A.; Gahlaut, R.; Abharana, N.; Bhattacharyya, D.; Mahamuni, S. Implications

of the size variation on the local structure and polarized emission of CsPbBr3 quantum dots. *Journal of Materials Science* **2021**, *56*, 6977–6986.

[77] Boldt, K.; Bartlett, S.; Kirkwood, N.; Johannessen, B. Quantification of Material Gradients in Core/Shell Nanocrystals Using EXAFS Spectroscopy. *Nano Letters* **2020**, *20*, 1009–1017.

[78] Khalfin, S.; Bekenstein, Y. Advances in lead-free double perovskite nanocrystals, engineering band-gaps and enhancing stability through composition tunability. *Nanoscale* **2019**, *11*, 8665–8679.

[79] Usman, M.; Yan, Q. Recent Advancements in Crystalline Pb-Free Halide Double Perovskites. *Crystals* **2020**, *10*, 62.

[80] Nair, S. S.; Krishnia, L.; Trukhanov, A.; Thakur, P.; Thakur, A. Prospect of double perovskite over conventional perovskite in photovoltaic applications. *Ceramics International* **2022**, *48*, 34128–34147.

[81] Bello, O. O.; Emetere, M. E. Progress and limitation of lead-free inorganic perovskites for solar cell application. *Solar Energy* **2022**, *243*, 370–380.

[82] Li, S.; Luo, J.; Liu, J.; Tang, J. Self-Trapped Excitons in All-Inorganic Halide Perovskites: Fundamentals, Status, and Potential Applications. *The Journal of Physical Chemistry Letters* **2019**, *10*, 1999–2007.

[83] Ghosh, S.; Shankar, H.; Kar, P. Recent developments of lead-free halide double perovskites: a new superstar in the optoelectronic field. *Materials Advances* **2022**, *3*, 3742–3765.

[84] Chen, X.; Jia, M.; Xu, W.; Pan, G.; Zhu, J.; Tian, Y.; Wu, D.; Li, X.; Shi, Z. Recent

Progress and Challenges of Bismuth-Based Halide Perovskites for Emerging Optoelectronic Applications. *Advanced Optical Materials* **2023**, *11*, 2202153.

[85] Sk, M. Recent progress of lead-free halide double perovskites for green energy and other applications. *Applied Physics A* **2022**, *128*, 462.

[86] Stroyuk, O.; Raievska, O.; Hauch, J.; Brabec, C. J. Doping/Alloying Pathways to Lead-Free Halide Perovskites with Ultimate Photoluminescence Quantum Yields. *Angewandte Chemie International Edition* **2023**, *62*, e202212668.

[87] Lei, H.; Hardy, D.; Gao, F. Lead-Free Double Perovskite Cs 2 AgBiBr 6 : Fundamentals, Applications, and Perspectives. *Advanced Functional Materials* **2021**, *31*, 2105898.

[88] Muscarella, L. A.; Hutter, E. M. Halide Double-Perovskite Semiconductors beyond Photovoltaics. *ACS Energy Letters* **2022**, *7*, 2128–2135.

[89] Ravi, V. K.; Singhal, N.; Nag, A. Initiation and future prospects of colloidal metal halide double-perovskite nanocrystals: Cs2AgBiX6 (X = Cl, Br, I). *Journal of Materials Chemistry A* **2018**, *6*, 21666–21675.

[90] Shadabroo, M. S.; Abdizadeh, H.; Golobostanfard, M. R. Elpasolite structures based on A2AgBiX6 (A: MA, Cs, X: I, Br): Application in double perovskite solar cells. *Materials Science in Semiconductor Processing* **2021**, *125*, 105639.

[91] Jain, A.; Voznyy, O.; Sargent, E. H. High-Throughput Screening of Lead-Free Perovskite-like Materials for Optoelectronic Applications. *Journal of Physical Chemistry C* **2017**, *121*, 7183–7187.

[92] Creutz, S. E.; Liu, H.; Kaiser, M. E.; Li, X.; Gamelin, D. R. Structural Diversity in Cesium Bismuth Halide Nanocrystals. *Chemistry of Materials* **2019**, *31*, 4685–4697.

[93] Lee, W.; Hong, S.; Kim, S. Colloidal Synthesis of Lead-Free Silver–Indium Double-Perovskite Cs 2 AgInCl 6 Nanocrystals and Their Doping with Lanthanide Ions. *The Journal of Physical Chemistry C* **2019**, *123*, 2665–2672.

[94] Chen, N.; Cai, T.; Li, W.; Hills-Kimball, K.; Yang, H.; Que, M.; Nagaoka, Y.; Liu, Z.; Yang, D.; Dong, A.; Xu, C.-Y.; Zia, R.; Chen, O. Yb- and Mn-Doped Lead-Free Double Perovskite Cs 2 AgBiX 6 (X = Cl – , Br –) Nanocrystals. *ACS Applied Materials & Interfaces* **2019**, *11*, 16855–16863.

[95] Vashishtha, P.; Griffith, B. E.; Fang, Y.; Jaiswal, A.; Nutan, G. V.; Bartók, A. P.; White, T.; Hanna, J. V. Elucidation of the structural and optical properties of metal cation (Na+, K+, and Bi3+) incorporated Cs2AgInCl6double perovskite nanocrystals. *Journal of Materials Chemistry A* **2022**, *10*, 3562–3578.

[96] Yang, B.; Chen, J.; Hong, F.; Mao, X.; Zheng, K.; Yang, S.; Li, Y.; Pullerits, T.; Deng, W.; Han, K. Lead-Free, Air-Stable All-Inorganic Cesium Bismuth Halide Perovskite Nanocrystals. *Angewandte Chemie International Edition* **2017**, *56*, 12471–12475.

[97] Yang, B.; Chen, J.; Yang, S.; Hong, F.; Sun, L.; Han, P.; Pullerits, T.; Deng, W.; Han, K. Lead-Free Silver-Bismuth Halide Double Perovskite Nanocrystals. *Angewandte Chemie International Edition* **2018**, *57*, 5359–5363.

[98] Dahl, J. C.; Osowiecki, W. T.; Cai, Y.; Swabeck, J. K.; Bekenstein, Y.; Asta, M.; Chan, E. M.; Alivisatos, A. P. Probing the Stability and Band Gaps of Cs 2 AgInCl 6 and Cs 2 AgSbCl 6 Lead-Free Double Perovskite Nanocrystals. *Chemistry of Materials* **2019**, *31*, 3134–3143.

[99] Wu, D.; Zhao, X.; Huang, Y.; Lai, J.; Li, H.; Yang, J.; Tian, C.; He, P.; Huang, Q.; Tang, X. Lead-Free Perovskite Cs 2 AgBiX 6 Nanocrystals with a Band Gap Fun-

nel Structure for Photocatalytic CO 2 Reduction under Visible Light. *Chemistry of Materials* **2021**, *33*, 4971–4976.

[100] Yang, B.; Mao, X.; Hong, F.; Meng, W.; Tang, Y.; Xia, X.; Yang, S.; Deng, W.; Han, K. Lead-Free Direct Band Gap Double-Perovskite Nanocrystals with Bright Dual-Color Emission. *Journal of the American Chemical Society* **2018**, *140*, 17001–17006.

[101] Billinge, S. J.; Levin, I. The problem with determining atomic structure at the nanoscale. *Science* **2007**, *316*, 561–565.

[102] Billinge, S. J. Nanoscale structural order from the atomic pair distribution function (PDF): There's plenty of room in the middle. *Journal of Solid State Chemistry* **2008**, *181*, 1695–1700.

[103] Freese, B. Exploring Extended X-ray Absorption Spectroscopy and Pair-Distribution Function Methods in Amorphous Semiconductors. Ph.D. thesis, DePaul University, 2018.

[104] Geddes, H. S.; Blade, H.; McCabe, J. F.; Hughes, L. P.; Goodwin, A. L. Structural characterisation of amorphous solid dispersions via metropolis matrix factorisation of pair distribution function data. *Chemical Communications* **2019**, *55*, 13346–13349.

[105] Mergelsberg, S. T.; De Yoreo, J. J.; Miller, Q. R.; Marc Michel, F.; Ulrich, R. N.; Dove, P. M. Metastable solubility and local structure of amorphous calcium carbonate (ACC). *Geochimica et Cosmochimica Acta* **2020**, *289*, 196–206.

[106] Mergelsberg, S. T.; Riechers, S. L.; Graham, T. R.; Prange, M. P.; Kerisit, S. N. Effect of Cd on the Nucleation and Transformation of Amorphous Calcium Carbonate. *Crystal Growth and Design* **2021**, *21*, 3384–3393.

[107] Harrington, R.; Hausner, D. B.; Bhandari, N.; Strongin, D. R.; Chapman, K. W.; Chupas, P. J.; Middlemiss, D. S.; Grey, C. P.; Parise, J. B. Investigation of surface structures by powder diffraction: a differential pair distribution function study on arsenate sorption on ferrihydrite. *Inorganic Chemistry* **2010**, *49*, 325–330.

[108] Egami, T.; Billinge, S. J. *Underneath the Bragg peaks : structural analysis of complex materials*, 2nd ed.; Pergamon, 2012.

[109] Billinge, S. J. L.; Kanatzidis, M. G. Beyond crystallography: the study of disorder, nanocrystallinity and crystallographically challenged materials with pair distribution functions. *Chemical Communications* **2004**, 749–760.

[110] Proffen, T.; Billinge, S. J. L.; Egami, T.; Louca, D. Structural analysis of complex materials using the atomic pair distribution function — a practical guide. *Zeitschrift für Kristallographie - Crystalline Materials* **2003**, *218*, 561–565.

[111] Proffen, T.; Billinge, S. J. L.; Egami, T.; Louca, D. Structural analysis of complex materials using the atomic pair distribution funtion - a practical guide. *Zeitschrift für Kristallographie* **2003**, *218*, 132–143.

[112] Masadeh, A. S.; Božin, E. S.; Farrow, C. L.; Paglia, G.; Juhas, P.; Billinge, S. J. L.; Karkamkar, A.; Kanatzidis, M. G. Quantitative size-dependent structure and strain determination of CdSe nanoparticles using atomic pair distribution function analysis. *Physical Review B* **2007**, *76*, 115413.

[113] Ouyang, G.; Li, X. L.; Tan, X.; Yang, G. W. Size-induced strain and stiffness of nanocrystals. *Applied Physics Letters* **2006**, *89*, 031904.

[114] Petkov, V.; Difrancesco, R. G.; Billinge, S. J.; Acharya, M.; Foley, H. C. Local structure of nanoporous carbons. *Philosophical Magazine B: Physics of Condensed Matter; Statistical Mechanics, Electronic, Optical and Magnetic Properties* **1999**, *79*, 1519–1530.

[115] Billinge, S. J. L. The rise of the X-ray atomic pair distribution function method: a series of fortunate events. *Philosophical Transactions of the Royal Society A: Mathematical, Physical and Engineering Sciences* **2019**, *377*, 20180413.

[116] Debye, P. Zerstreuung von Röntgenstrahlen. *Annalen der Physik* **1915**, *351*, 809–823.

[117] Zernike, F.; Prins, J. A. Die Beugung von Röntgenstrahlen in Flüssigkeiten als Effekt der Molekülanordnung. *Zeitschrift für Physik A Hadrons and nuclei* **1927**, *41*, 184–194.

[118] Debye, P.; Menke, H. The determination of the inner structure of liquids by X-ray means. *Physik Z.* **1930**, *31*, 797.

[119] Evans, J. *X-ray Absorption Spectroscopy for the Chemical and Materials Sciences*; John Wiley & Sons, Ltd., 2018.

[120] Ravel, B. Path degeneracy and EXAFS analysis of disordered materials. *Journal of Synchrotron Radiation* **2014**, *21*, 1269–1274.

[121] Wu, J.; Webb, S. M.; Brennan, S.; Haile, S. M. Dopant site selectivity in BaCe 0.85M 0.15O 3-δ by extended x-ray absorption fine structure. *Journal of Applied Physics* **2005**, *97*.

[122] Kelly, T. D.; Kong, L.; Buchanan, D. A.; Brant, A. T.; Petrosky, J. C.; McClory, J. W.; Adamiv, V. T.; Burak, Y. V.; Dowben, P. A. EXAFS and EPR analysis of the local structure of Mn-doped Li 2 B 4 O 7. *physica status solidi (b)* **2013**, *250*, 1376–1383.

[123] Bacewicz, R.; Pietnoczka, A.; Gehlhoff, W.; Voevodin, V. G. Local order in ZnGeP 2 :Mn crystals. *physica status solidi (a)* **2007**, *204*, 2296–2301.

[124] Lei, J.; Chang, L. Y.; Dong, Z.; Liu, L. The role of EuBr2 in modulating the crystallization and luminescence of caesium lead bromide. *Materials Research Bulletin* **2021**, *137*, 111191.

[125] Okazaki, T.; Sekiya, E. H.; Saito, K. The difference in the coordination environment around Yb3+ ions between Yb-Al-doped and Yb-P-doped silica glasses. *Japanese Journal of Applied Physics* **2020**, *59*, 102003.

[126] Yoshida, T.; Tanaka, T.; Yamamoto, T.; Yoshida, S.; Ishitani, H.; Kobayashi, S. XAFS study of ytterbium complexes as new-type Lewis acid catalysts. *Journal of Synchrotron Radiation* **1999**, *6*, 455–457.

[127] McLeod, J. A.; Wu, Z.; Sun, B.; Liu, L. The influence of the I/Cl ratio on the performance of CH3NH3PbI3-x Clx-based solar cells: why is CH3NH3I : PbCl2 = 3:1 the "magic" ratio? *Nanoscale* **2016**, *8*, 6361–6368.

[128] Rehr, J. J.; Kas, J. J.; Vila, F. D.; Prange, M. P.; Jorissen, K. Parameter-free calculations of X-ray spectra with FEFF9. *Physical Chemistry Chemical Physics* **2010**, *12*, 5503–5513.

[129] Ye, T.; Pan, L.; Yang, Y.; Liang, Q.; Lu, Y.; Sui, M.; Golberg, D.; Wang, X. Synthesis of Highly-Oriented Black CsPbI 3 Microstructures for High-Performance Solar Cells. *Chemistry of Materials* **2020**, *32*, 3235–3244.

[130] Levina, A.; Armstrong, R. S.; Lay, P. A. Three-dimensional structure determination using multiple-scattering analysis of XAFS: Applications to metalloproteins and coordination chemistry. *Coordination Chemistry Reviews* **2005**, *249*, 141–160.

[131] Kelly, S. D.; Kemner, K. M.; Fein, J. B.; Fowle, D. A.; Boyanov, M. I.; Bunker, B. A.; Yee, N. X-ray absorption fine structure determination of pH-dependent U-bacterial cell wall interactions. *Geochimica et Cosmochimica Acta* **2002**, *66*, 3855–3871.

[132] Williams, D. B.; Carter, C. B. *Transmission Electron Microscopy: A Textbook for Materials Science*; 2009.

[133] Levy, S.; Khalfin, S.; Pavlopoulos, N. G.; Kauffmann, Y.; Atiya, G.; Shaek, S.; Dror, S.; Shechter, R.; Bekenstein, Y. The Role Silver Nanoparticles Plays in Silver-Based Double-Perovskite Nanocrystals. *Chemistry of Materials* **2021**, *33*, 2370–2377.

[134] Park, J.; Zheng, H.; Lee, W. C.; Geissler, P. L.; Rabani, E.; Alivisatos, A. P. Direct Observation of Nanoparticle Superlattice Formation by Using Liquid Cell Transmission Electron Microscopy. *ACS Nano* **2012**, *6*, 2078–2085.

[135] Brennan, M. C.; Toso, S.; Pavlovetc, I. M.; Zhukovskyi, M.; Marras, S.; Kuno, M.; Manna, L.; Baranov, D. Superlattices are Greener on the Other Side: How Light Transforms Self-Assembled Mixed Halide Perovskite Nanocrystals. *ACS Energy Letters* **2020**, *5*, 1465–1473.

[136] Cherniukh, I.; Rainò, G.; Stöferle, T.; Burian, M.; Travesset, A.; Naumenko, D.; Amenitsch, H.; Erni, R.; Mahrt, R. F.; Bodnarchuk, M. I.; Kovalenko, M. V. Perovskite-type superlattices from lead halide perovskite nanocubes. *Nature* **2021**, *593*, 535–542.

[137] De Yoreo, J. J.; Sommerdijk, N. A. J. M. Investigating materials formation with liquid-phase and cryogenic TEM. *Nature Reviews Materials* **2016**, *1*, 16035.

[138] Zhu, Y.; Yuan, D.; Zhang, H.; Xu, T.; Sun, L. Atomic-scale insights into the formation of 2D crystals from in situ transmission electron microscopy. *Nano Research* **2021**, *14*, 1650–1658.

[139] Zhu, G.; Sushko, M. L.; Loring, J. S.; Legg, B. A.; Song, M.; Soltis, J. A.; Huang, X.; Rosso, K. M.; De Yoreo, J. J. Self-similar mesocrystals form via interface-driven nucleation and assembly. *Nature* **2021**, *590*, 416–422.

[140] Song, M.; Zhou, G.; Lu, N.; Lee, J.; Nakouzi, E.; Wang, H.; Li, D. Oriented attachment induces fivefold twins by forming and decomposing high-energy grain boundaries. *Science* **2020**, *367*, 40–45.

[141] Lyu, J.; Gong, X.; Lee, S.-J.; Gnanasekaran, K.; Zhang, X.; Wasson, M. C.; Wang, X.; Bai, P.; Guo, X.; Gianneschi, N. C.; Farha, O. K. Phase Transitions in Metal–Organic Frameworks Directly Monitored through In Situ Variable Temperature Liquid-Cell Transmission Electron Microscopy and In Situ X-ray Diffraction. *Journal of the American Chemical Society* **2020**, *142*, 4609–4615.

[142] Zhang, Q.; Peng, X.; Nie, Y.; Zheng, Q.; Shangguan, J.; Zhu, C.; Bustillo, K. C.; Ercius, P.; Wang, L.; Limmer, D. T.; Zheng, H. Defect-mediated ripening of core-shell nanostructures. *Nature Communications* **2022**, *13*, 2211.

[143] Boston, R.; Schnepp, Z.; Nemoto, Y.; Sakka, Y.; Hall, S. R. In Situ TEM Observation of a Microcrucible Mechanism of Nanowire Growth. *Science* **2014**, *344*, 623–626.

[144] Qin, F.; Wang, Z.; Wang, Z. L. Anomalous Growth and Coalescence Dynamics of Hybrid Perovskite Nanoparticles Observed by Liquid-Cell Transmission Electron Microscopy. *ACS Nano* **2016**, *10*, 9787–9793.

[145] Spurgeon, S. R.; Du, Y.; Chambers, S. A. Measurement Error in Atomic-Scale Scanning Transmission Electron Microscopy—Energy-Dispersive X-Ray Spectroscopy (STEM-EDS) Mapping of a Model Oxide Interface. *Microscopy and Microanalysis* **2017**, *23*, 513–517.

Chapter 2

DEFECT STRUCTURE IN QUANTUM-CUTTING YB^{3+}-DOPED $CSPBCL_3$ PEROVSKITES PROBED BY X-RAY ABSORPTION AND ATOMIC PAIR DISTRIBUTION FUNCTION ANALYSIS

Reproduced with permission from:

Kluherz, K. T.; Mergelsberg, S. T.; Sommer, D. E.; Roh, J. Y. D.; Saslow, S. A.; Biner, D.; Krämer, K. W.; Dunham, S. T.; De Yoreo, J. J.; Gamelin, D. R. Defect Structure in Quantum-Cutting Yb^{3+}-Doped $CsPbCl_3$ Perovskites Probed by X-Ray Absorption and Atomic Pair Distribution Function Analysis. *Phys. Rev. Mater.* **2022**, 6 (7), 074601. https://doi.org/10.1103/PhysRevMaterials.6.074601.

2.1 Overview

Ytterbium-doping in all-inorganic lead-halide perovskites ($CsPb(Cl_{1-x}Br_x)_3$) generates novel properties including quantum cutting and narrow line emission, making these materials attractive spectral down-converters for solar photovoltaics. The relationship between this optical efficiency and the defect structure(s) associated with Yb^{3+} dopants within perovskites is not well understood. Various charge-neutral doping motifs have previously been proposed and studied computationally, including clusters involving two substitutional Yb^{3+} ions charge-compensated by a single local Pb^{2+} vacancy. Near-band-edge defect states associated with such motifs are believed to play an important mechanistic role in quantum cutting itself. Here, we report the results of X-ray absorption and X-ray total-scattering measurements on ytterbium-doped $CsPbCl_3$. XANES shows that the dopant oxidation state

is exclusively Yb^{3+}, and a combination of Yb L_3 and Pb L_3 EXAFS shows that this Yb^{3+} substitutes exclusively at Pb^{2+} sites, where it adopts a pseudo-octahedral $[YbCl_6]^{3-}$ coordination environment. Shell-by-shell fits to the data show a short Yb-Cl bond distance of 2.58 Å compared to the Pb-Cl bond distance of 2.83 Å. We confirm this finding by X-ray pair distribution function analysis, which also shows evidence of additional Pb^{2+} vacancy formation induced by Yb^{3+} doping. We evaluate whether this is the primary mechanism of charge compensation using simulated EXAFS and pair distribution function data for several computed defect structures. Together, these results resolve the local dopant structures and charge-compensation mechanisms in lanthanide-doped all-inorganic lead-halide perovskites, and, as such, significantly advance the understanding of structure-function relationships in this important class of materials.

2.2 Introduction

Lanthanide doping has been reported to increase lattice stability, expand optical properties, and improve the photovoltaic performance of lead-halide perovskites [1-5]. Yb^{3+} doping into cesium-lead-halide ($CsPb(Cl_{1-x}Br_x)_3$, $0 \leq x \leq 2/3$) perovskites can also produce photoluminescence quantum yields (PLQYs) above 100% via a unique quantum-cutting process, in which the energies of blue or UV photons absorbed by the perovskite are split to yield two emitted near-infrared photons from Yb^{3+} dopants [3,6-9]. Such "quantum cutting" has been demonstrated to markedly improve the power-conversion efficiencies (PCE) of silicon and copper indium gallium selenide photovoltaics [3], and it has the capacity to increase the PCEs of high-efficiency silicon heterojunction and other red-sensitive solar cells by as much as ∼20% (relative) [10].

The specific ytterbium species that enable quantum cutting remain largely unknown. The Yb^{3+} emission from quantum-cutting $CsPbCl_3$ nanocrystals, thin films, and bulk single crystals has been studied in detail [11]. These data provide evidence of multiple Yb^{3+}

species coexisting in these materials, but just one primary Yb^{3+} emission center, identified as having pseudo-octahedral coordination. The Yb^{3+} speciation probed by photoluminescence (PL) is biased toward detection of only those ions participating in quantum cutting, however, and consequently reveals little about associated dopant-induced defects. Specifically, Yb^{3+} ions are believed to substitute for Pb^{2+} in the perovskite lattice, but because of their extra positive charges, such substitution requires charge compensation via defect formation. A charge-neutral defect cluster involving two substitutional Yb^{3+} ions ($[Yb^{3+}]^{+}$) compensated by an adjacent Pb^{2+} vacancy ($[V_{Pb}]^{2-}$) has been proposed as a candidate structure (i.e., $[Yb^{3+}\text{-}V_{Pb}\text{-}Yb^{3+}]^{0}$) [8]. Computational studies [12] support the existence of this defect cluster in doped $CsPbCl_3$, and also predict the co-existence of other defect motifs, most prevalently substitutional $[Yb^{3+}]^{+}$ ions compensated by distal $[V_{Pb}]^{2-}$, and $[Yb^{3+}-V_{Pb}]^{-}$ defects with distal $[Yb^{3+}]^{+}$ for compensation. The speciation distribution depends on the Yb^{3+} concentration and the chemical activities of the other lattice constituents. Near-band-edge states associated with such defect motifs appear to play an important mechanistic role in quantum cutting itself [8,11,13]. PL may also overlook other relevant species. For example, Yb^{3+} is among the most easily reduced of the trivalent lanthanides, raising the possibility of yet-undetected Yb^{2+} species. Indeed, $CsYbI_3$ perovskites with B-site Yb^{2+} are known [14], and an easily reduced Yb^{3+} site has been proposed as a transient intermediate in some quantum-cutting mechanistic schemes [15,16]. To date, X-ray diffraction (XRD) has been inconclusive about the structural changes to $CsPbCl_3$ associated with lanthanide doping, with some reports showing no changes in diffraction until doping exceeds 10% (percentage of total B-site cations) [7,8,11], and others showing small peak shifts and new peaks at only 1% doping [6,17]. Further structural characterization is needed.

Several reports have described the use of X-ray absorption techniques to study the local structures of dopants in metal-halide perovskites, including Mn^{2+}, Cu^{2+}, Ni^{2+}, and Yb^{3+} [18-21]. Although the long-range order (i.e., periodicity) of the lattice is generally not altered

upon doping, the short-range order around the dopant frequently differs from that of the host lattice. For example, Ni^{2+} and Cu^{2+} impurities increase short-range order in metal-halide perovskites, whereas Yb^{3+} is reported to decrease the short-range order [18,19,21]. The accompanying Pb L_3 EXAFS data are largely insensitive to such dopant-induced changes in short-range order. An EXAFS study of Yb^{3+}:$CsPbCl_3$ nanocrystals supports the proposed substitution of Yb^{3+} at Pb^{2+} sites [19], and reports that increased doping causes an increase in anomalous band-edge emission, which the authors attributed to structural defects. Previous work has also investigated the $CsPbBr_3$ perovskite lattice via X-ray total scattering [22,23], identifying short- to medium-range order and domain twinning. To date, there have been no X-ray total scattering studies of doped $CsPbX_3$ perovskites. Such experiments, in conjunction with X-ray absorption spectroscopy, are anticipated to advance our understanding of the microscopic structures of these important opto-electronic materials.

Here, we report structural studies of 0.0%, 0.9% and 7.4% ytterbium-doped $CsPbCl_3$ using extended X-ray absorption fine structure (EXAFS) and pair distribution function (PDF) methods. These structural data are complemented by density functional theory (DFT) and ab initio molecular dynamics (AIMD) calculations. We find conclusive evidence for substitution of Yb^{3+} at Pb^{2+} sites in $CsPbCl_3$, with no detectable Yb^{2+}, and additionally observe the formation of Pb^{2+} vacancies upon doping with Yb^{3+}. These experimental results are discussed in relation to various proposed local defect structures.

2.3 Methods

2.3.1 Materials and Sample Preparation

Yb^{3+}:$CsPbCl_3$ single crystals were grown via the Bridgman technique from melts of stoichiometric admixtures of precursors (see Roh *et al* [11] for details). For the experiments detailed here, three such samples were used; they were obtained using nominal Yb^{3+} concentrations of 0, 2, and 10% during growth, respectively, where Yb^{3+} concentrations are reported as

the percentage of total *B*-site cations, *i.e.*, $\%Yb^{3+} = 100\%*[Yb]/([Yb]^{+}[Pb])$. Optical spectroscopy of these single crystals has been reported previously [11]. Yb^{3+} contents in these crystals were determined analytically *via* ICP-AES (PerkinElmer 8300) and found to be 0.0, 0.9, and 7.4% Yb^{3+}, respectively. For ICP-AES measurements, portions of the three crystals were digested in concentrated nitric acid with sonication, then diluted with nanopure water. For XRD and PDF measurements, portions of the Bridgman crystals were gently crushed under nitrogen atmosphere with mortar and pestle to produce microcrystalline powders. Powder XRD data (Figure A.1) were collected using a Bruker D8 Discover with a Cu Kα source (50 kV, 1 mA). Thin film samples for X-ray absorption spectroscopy (XAS) measurements were made by single-source vapor deposition on quartz substrates followed by thermal annealing in ambient atmosphere at 250 °C for 10 min [25]. A nominal Yb^{3+} content of 5% was used.

2.3.2 XAS Measurements

X-ray Absorption Near Edge Structure (XANES) and Extended X-ray Absorption Fine Structure (EXAFS) spectra were collected at beamlines 20-ID-B and 9-BM at the Advanced Photon Source at Argonne National Laboratory. Yb L_3 edge (8944 eV) and Pb L_3 edge (13035 eV) data were collected in fluorescence mode for single crystals of each sample at room temperature under helium atmosphere with active purging (see Figure A.2). A Si(111) double-crystal monochromator was used to select the incident energy with He filled ion chambers to monitor the flux. The monochromator was calibrated using Cu foil (8979 eV) or Pb foil. The pre-edge region was collected from 200 eV to 30 eV below the edge with a step size of 5 eV and a collection time of 0.5 s at each step. From 30 eV below the edge to 30 eV above the edge, data was collected in 0.50 eV steps for 0.5 s at each step. Post-edge data was collected to 14 keV (for Yb) or 13 keV (for Pb) and obtained with a 0.05 keV step size and a collection time of 0.5 s per step. Ytterbium (II) iodide and ytterbium (III) chloride

hexahydrate Yb L_3 edges were collected in transmission mode for use as XANES fitting standards. Data normalization, energy calibration, and linear-combination fitting (LCF) were performed using ATHENA software [26]. Yb XANES spectra were fit using a linear combination of spectra of the two Yb standards. R-space EXAFS data were corrected in Artemis using a Cl single scattering path from the $CsPbCl_3$ host lattice structure. For sake of clarity, we use R + ΔR to denote the corrected radial distance axis in the EXAFS data. Simulated EXAFS data were calculated from AIMD simulated structures (*vide infra*) using the FEFF10 package [27-29]. Fits to the EXAFS data from proposed defect structures were performed with ARTEMIS software [26].

2.3.3 PDF Measurements

X-ray total scattering data were collected at beamline 11-ID-B at the Advanced Photon Source at Argonne National Laboratory [30]. Powdered single-crystal samples were measured at room temperature under a low-O_2 nitrogen atmosphere using monochromatic X-rays at 86.7 keV (λ = 0.1430 Å). Using a Varex 4343CT area detector (150 x 150 μm^2 pixel size), the sample-to-detector distance and detector non-orthogonality were calibrated with a CeO_2 standard (NIST 674a). X-ray total scattering data were integrated using the GSAS-II software [31] and a radial bin size of 1400. Background subtraction and PDF processing were initially performed using the PDFgetX3 software [32], with additional quantitative processing in PDFgetX2 [33]. For PDF processing, a Q_{max} of 24 $Å^{-1}$ and r_{max} of 30 $Å^{-1}$ were used. Additional corrections account for composition (as determined by ICP), sample absorption, and Compton scattering. The PDFgui [34] package was used to determine the instrument parameters q_{damp} = 0.0364 $Å^{-1}$ and q_{broad} = 0.00118 $Å^{-1}$. Partial PDFs of $CsPbCl_3$ were calculated using a reference $CsPbCl_3$ Pnma structure (ICSD #243734) [35] and the refined instrumental parameters. Differential PDFs (dPDF), D(r), were obtained by subtracting the $CsPbCl_3$ G(r) from the data for each of the two doped Yb^{3+}:$CsPbCl_3$ samples. For clarity,

r in Å is used to denote the absolute radial distance axis in our PDF figures. The synthetic G(r) profiles were calculated from 1 ps AIMD trajectories for each model defect structure using the powder method in the Discus [36] software package, with the refined instrument parameters qdamp and qbroad. Calculated profiles were computed for every 60 fs of simulation time (using 2 fs time steps) and averaged to account for thermal motion of the system over 1 ps. The first and second halves of the trajectory were compared to account for possible sampling bias, but none was found (Fig. A.10). dPDF data for the simulations was calculated by subtracting the synthetic PDF for $CsPbCl_3$ from the synthetic PDF for the respective proposed dopant structure.

2.3.4 Ab Initio Simulations

Details of the simulation methods were previously reported [12]. All first-principles calculations were carried out using the Vienna Ab-Initio Simulation Package (VASP) [37,38]. Plane-wave, Kohn-Sham density functional theory calculations employed the all-electron projector-augmented wave (PAW) method in the generalized gradient approximation (GGA) with the semilocal PBEsol functional [39-41]. In the pseudopotentials, 9 electrons of atomic Cs ($5s^2 5p^6 6s^1$), 4 electrons of atomic Pb ($6s^2 6p^2$), and 7 electrons of atomic Cl ($3s^2 3p^5$) were treated as valence electrons, while 13 f electrons in the $[Xe]4f^{14}6s^2$ valence configuration of atomic Yb were treated as frozen core states. A plane-wave basis cutoff was set to 400 eV, and a Gamma-centered k-point mesh was used for Brillouin-zone integration [42]. The volume, shape, and atomic positions were relaxed until interatomic Hellmann-Feynman forces were less than 0.01 eV/Å.

AIMD simulations were run with VASP for 1 ps durations with 2 fs time steps for each defect structure. Using the Nose-Hoover thermostat and NVT ensemble, the temperature was set to 300 K, and the simulation volume was fixed to the relaxed volume of the defect supercells. All defect calculations were performed on 3x3x2 supercells derived from the

20-atom unit cell in the low-energy Pnma perovskite phase.

2.4 Results and Discussion

2.4.1 XANES and EXAFS Measurements

Figure 2.1 shows Yb L_3-edge XANES data collected for 0.9% and 7.4% Yb-doped $CsPbCl_3$ single crystals, a 5% Yb-doped $CsPbCl_3$ thin film, an ytterbium (III) chloride standard, and an ytterbium (II) iodide standard. The thin film sample was included to account for the possible influence of surface sites on the oxidation state of Yb. The Yb L_3 edges of the doped $CsPbCl_3$ samples agree well with the Yb(III) standard (vertical dashed line). Fitting these data to linear combinations of the two Yb standards allows the conclusion that at least 97% of the Yb dopants are in the Yb(III) oxidation state in both doped samples, and within experimental uncertainty of 100%. A second-derivative analysis (not shown) of the data shows no evidence of any Yb^{2+} peak, consistent with the conclusion that all Yb in these doped $CsPbCl_3$ samples is Yb^{3+}. We therefore henceforth refer to these samples as Yb^{3+}:$CsPbCl_3$.

To probe the local structure of Yb^{3+} in the $CsPbCl_3$ host lattice, Pb L_3-edge (13035 eV) and Yb L_3-edge (8943 eV) EXAFS data were collected for the $CsPbCl_3$, 0.9% Yb^{3+}, and 7.4% Yb^{3+}-doped $CsPbCl_3$ single crystals (Figure A.3). Figure 2.2 shows the scaled, phase-corrected Fourier transform EXAFS data for the Pb L_3 and Yb L_3 edges of the 0.9% and 7.4% Yb^{3+}-doped $CsPbCl_3$ single crystals. For ease of comparison, the Pb data for each sample have been scaled so their peak intensity matches that of the corresponding Yb data, but the Yb L_3 edge data have not been scaled. Only the nearest-neighbor peak, corresponding to Cl single scatterers, is visible in each Pb L_3 measurement, as previously reported for Pb edge data from other perovskite samples [18,19,21,43]. The Yb L_3 data are similar to the Pb L_3 data except that they show a marked decrease in R by 0.2 Å, consistent with shorter Yb^{3+}- Cl^- bond lengths compared to Pb^{2+}-Cl^- bond lengths. Shell-by-shell fitting of these

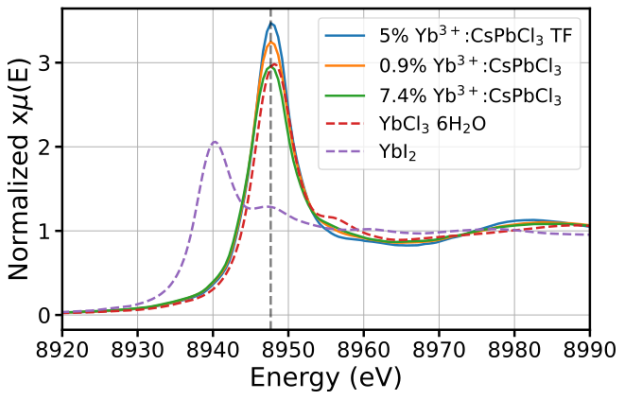

Figure 2.1: Yb L_3-edge XANES spectra for single-crystal and thin-film (TF) samples of Yb^{3+}:CsPbCl3, compared with Yb^{3+} ($YbCl_3 \cdot 6\,H_2O$) and Yb^{2+} (YbI_2) standards. All Yb^{3+}:$CsPbCl_3$ samples show the same dominant peak coinciding with the Yb^{3+} standard peak (vertical dashed line). The second derivatives of the Yb^{3+}:$CsPbCl_3$ spectra (not shown) also show no detectable Yb^{2+}.

data shows good agreement with a structure involving 6 nearest-neighbor Cl^- anions in an octahedral arrangement around Yb^{3+}. For the data from the 7.4% Yb^{3+} sample, the shoulder at 2.0 Å is accounted for well by the Cl single scattering path fits. We attribute the greater shoulder at 2.1 Å in the 0.9% Yb^{3+}:$CsPbCl_3$ Yb L_3 data to Fourier noise, visible in the k-space data (see Figure A.3).

The DFT-optimized defect structures previously identified by Sommer et al. [12] were enlisted to assist further assessment the Yb^{3+}-related structures on an atomic scale. Figure 2.3 shows schematic representations of the four main defect structures considered in this work. In each structure, Yb^{3+} dopants occupy Pb^{2+} sites (Yb_{Pb}) in the $CsPbCl_3$ lattice. The simplest structure is a substitutional Yb^{3+} ion with no other proximal defects, i.e., a $[Yb_{Pb}]^+$ defect. This defect lacks local charge compensation and is predicted to be less prevalent than charge-compensated defect structures, particularly at experimentally relevant Yb^{3+}

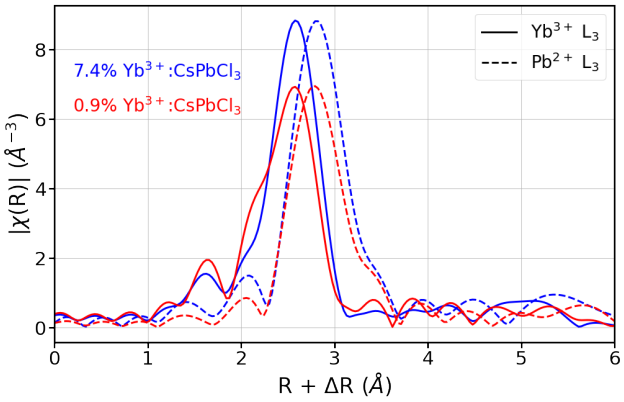

Figure 2.2: Fourier transform (real space) EXAFS spectra from the Yb L_3 (solid) and Pb L_3 (dashed) edges for 7.4%- (blue) and 0.9%-doped (red) Yb^{3+}:$CsPbCl_3$ single crystals. The Pb data have been vertically scaled so the primary peak intensity matches that of the Yb L_3 data for the same sample for comparison. Data have been phase-corrected to the primary peak for each edge, based on M-Cl single scattering paths, where M = Yb or Pb. A window of 1.0 to 2.8 Å was used for shell-by-shell fitting. The peak positions indicate a 0.2 Å contraction of $[YbCl_6]^{3-}$ octahedra relative to $[PbCl_6]^{4-}$ octahedra.

concentrations [12]. Among the more prevalent structures are Yb_{Pb} with an adjacent Pb^{2+} vacancy (V_{Pb}), i.e., a $[Yb_{Pb}\text{-}V_{Pb}]^{-}$ defect (in conjunction with a distal $[Yb_{Pb}]^{+}$), and charge-neutral defect clusters involving 2 Yb_{Pb} ions adjacent to a single V_{Pb}, i.e., a $[Yb_{Pb}\text{-}V_{Pb}\text{-}Yb_{Pb}]^{0}$ "dimer" defect. Two such dimer defect structures are possible, one in a linear arrangement and the other in a bent (orthogonal) arrangement. Such structures may also exist with different orientations relative to the crystallographic axes. DFT calculations predict the energies of these various arrangements to be essentially equivalent [12]. Using these DFT structures, we performed shell-by-shell fits to the Yb EXAFS data using the Artemis package (Figure A.5, Tables A.1 and A.2). All defect structures fit to the nearest-neighbor Yb-Cl scattering path equally well, with the exception of the $[Yb_{Pb}]^{+}$ structure, which yields slightly higher R-factors and χ^2_{red} goodness-of-fit values, indicating a poorer fit.

Figure 2.4 shows simulated EXAFS results for each of the computed Yb^{3+} defect structures, in comparison with the experimental Yb L_3 EXAFS data. These data are plotted in both k-space and R-space. The computed k-space EXAFS data show only small variations in peak shape and position among the various proposed structures, with minor variations around 4, 8, and 9 Å and growing more distinct at 10 Å and beyond. The k-space plot terminates at 11 Å, reflecting the cutoff used in data processing. Similarly, the R-space features are quite similar for each of the 4 computed defect structures, all showing a dominant nearest-neighbor chloride peak at 2.2 Å and only small secondary features. The vertical dashed lines in Figure 2.4b highlight the distances at which the most distinctive differences between computed structures are found. Unfortunately, the differences in the experimental data among these structures in either k- or R-space representations are too slight to enable differentiation between the defect models. Using Athena, the experimental spectra were fit using a linear combination of simulated spectra for each structure. This exercise (not shown) found similar goodness of fit regardless of the simulated structure, likely due to structural similarities particularly in the nearest-neighbor peak, but also extending to the

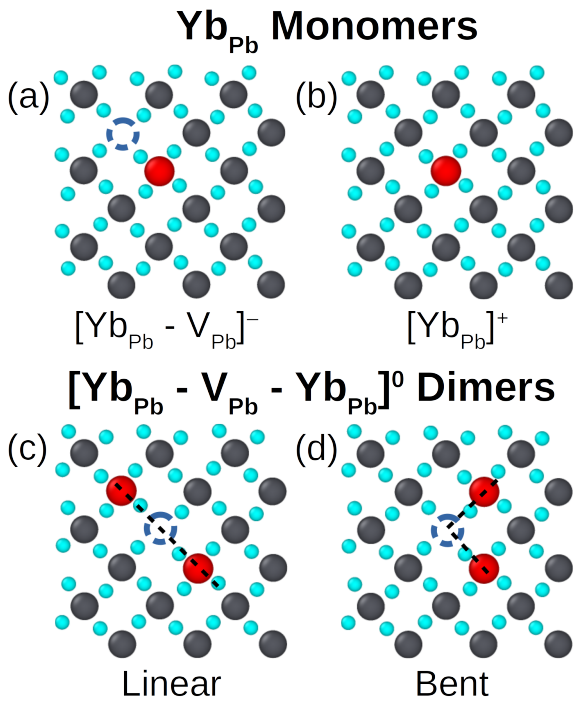

Figure 2.3: Yb^{3+} dopant/defect $CsPbCl_3$ structures (sliced along [110] plane) used in DFT calculations. Red: Yb^{3+} ; Gray: Pb^{2+} ; Blue: Cl^{-}. Cs^{+} ions have been omitted for clarity. (a) $[Yb_{Pb}\text{-}V_{Pb}]^{-}$: A substitutional Yb^{3+} adjacent to a Pb^{2+} vacancy. (b) $[Yb_{Pb}]^{+}$: A single substitutional Yb^{3+}. (c,d) $[Yb_{Pb}\text{-}V_{Pb}\text{-}Yb_{Pb}]^{0}$: Charge-neutral "dimer" structures involving two substitutional Yb^{3+} ions adjacent to a single Pb^{2+} vacancy in (c) a linear arrangement and (d) a bent or orthogonal arrangement.

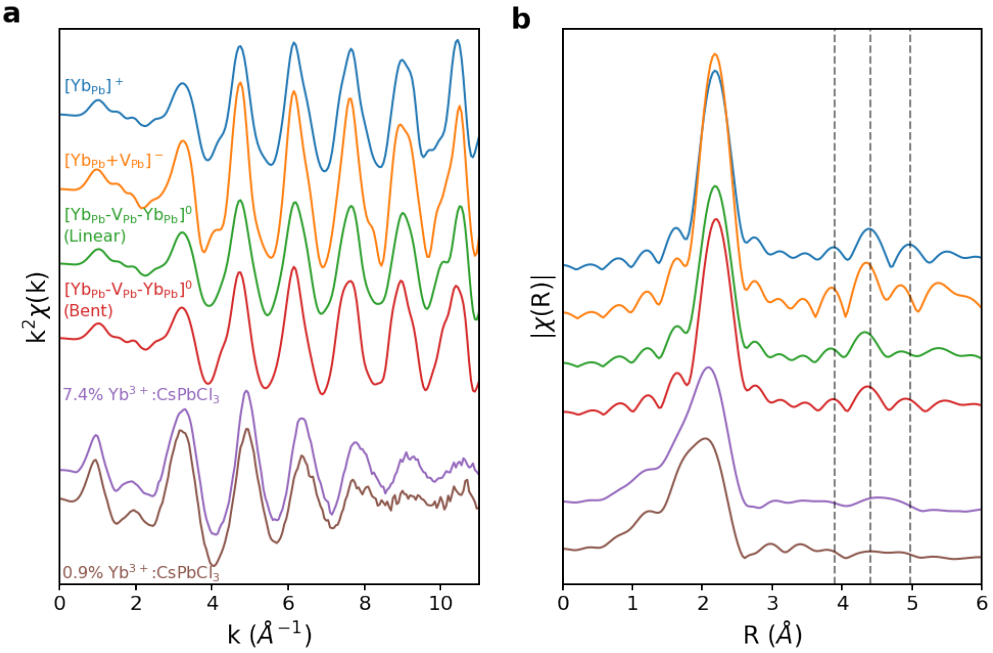

Figure 2.4: EXAFS spectra calculated from AIMD trajectories (top) from each calculated structure of Fig. 2.3, compared with Yb L_3-edge EXAFS data (purple, brown) in (a) k-space and (b) R-space for 7.4%- and 0.9%-doped Yb^{3+}:$CsPbCl_3$ single crystals. Dashed lines in (b) serve as a guide for the eye on minor peak positions.

region where second-nearest neighboring peaks are resolved. EXAFS was thus unable to distinguish among these Yb^{3+} defect structures, and did not yield additional structural insights beyond the nearest-neighbor distances deduced from Figure 2.2. We therefore turned to PDF measurements to probe differences in the short-range order on the bulk scale.

2.4.2 PDF Characterization

Figure 2.5a shows PDF profiles (G(r)) measured from powders of the same $CsPbCl_3$, 0.9% Yb^{3+}:CsPbCl3, and 7.4% Yb^{3+}:$CsPbCl_3$ samples used above. All three curves are qualitatively similar to

those previously reported for undoped $CsPbBr_3$ perovskites, [22,23] with the expected reduction in G(r) intensity due to the use here of Cl^- rather than the more electron-rich Br^-. PDF calculations based on existing crystal structures [35] predict the short-range peaks associated with specific atom pairs: Pb-Cl, Cs-Cl, Pb-Cs, and Pb-Pb (Figure 2.5). The Cs-associated peaks, particularly the Cs-Cl atom pair, show large broadening as expected from the distribution of Cs bond distances in this host lattice [35]. Although the overall PDF results are very similar for all three samples, subtle differences are apparent, particularly in the 7.4% Yb^{3+}:$CsPbCl_3$ data. Notable features include a shoulder on the Pb-Cl peak at ∼2.58 Å and reductions in the peak intensities marked with green and black dashed lines in Figure 2.5. To highlight these differences, Figure 2.5b shows differential PDF (dPDF, D(r)) data obtained by subtracting the $CsPbCl_3$ data from the Yb^{3+}:$CsPbCl_3$ data. These dPDF data reveal a clear increase in intensity of the shoulder near the Pb-Cl peak, as well as negative intensities marked with the black dashed lines. The 0.9% data appear to share the same features as the 7.4% data except with smaller amplitudes and hence lower signal-to-noise ratios. Partial PDF calculations show that the majority of these negative D(r) intensities correspond to Pb-Pb atom pairs (black dashed lines in Figure 2.5, see Figure A.7). These results demonstrate a loss of Pb-Pb atom pair correlation upon Yb^{3+} doping in $CsPbCl_3$.

Figure 2.6 enlarges the PDF and dPDF data for the 7.4% Yb^{3+}:$CsPbCl_3$ sample from Figure 2.5 between 2.3 and 3.2 Å to focus on just the first M-Cl feature. These data highlight the appearance of a shoulder on the left side of the Pb-Cl peak upon Yb^{3+} doping, at r = 2.58 Å. This shoulder coincides with a corresponding decrease in the Pb-Cl peak intensity. No similar shoulder is observed at higher r values. The location of this peak is consistent with the r = 2.6 Å Yb-Cl nearest-neighbor distance observed by EXAFS (Figure 2.2). We thus assign the shoulder at 2.58 Å to Yb-Cl pairs. This distance is slightly shorter than those calculated by DFT for the model system of gas-phase $YbCl_6^{3-}$ (2.680 Å), [44] and those predicted by ground state DFT for Yb-Cl in $CsPbCl_3$ (2.62 Å) [12]. For comparison,

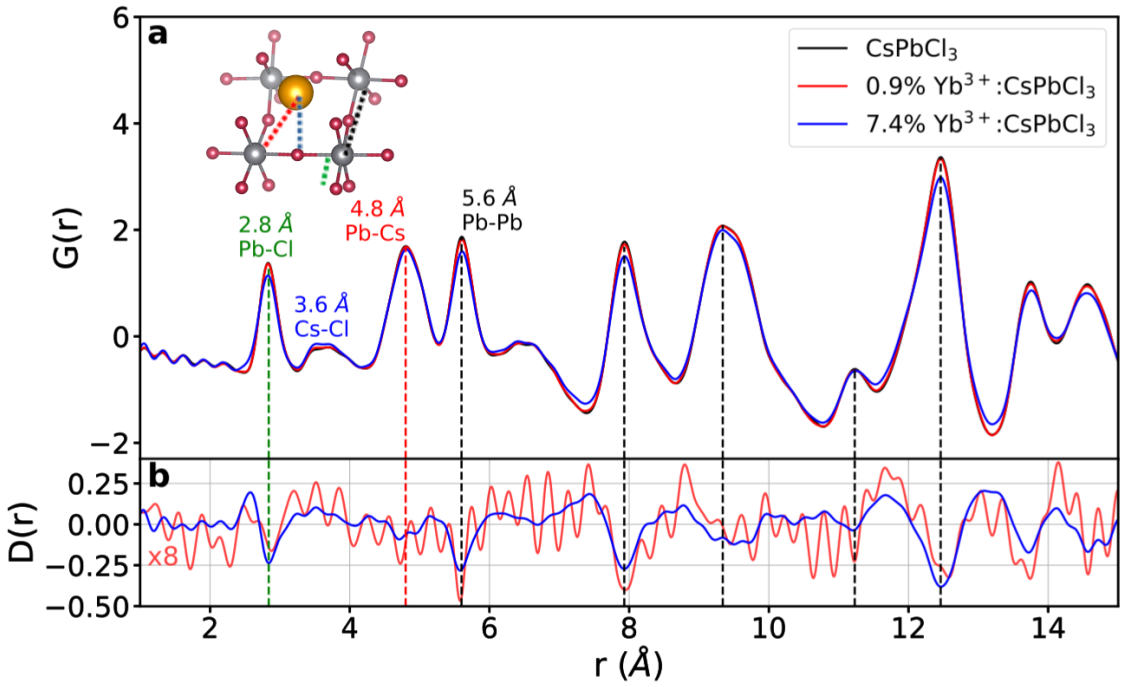

Figure 2.5: (a) Experimental Pair Distribution Function profiles (PDF, G(r)) measured for $CsPbCl_3$, 0.9% Yb^{3+}:$CsPbCl_3$, and 7.4% Yb^{3+}:$CsPbCl_3$ powdered single crystals. Primary short-range-order peaks are labeled. Inset: color-coordinated illustration of key atom pairs in the $CsPbCl_3$ structure. Black dashed lines denote peaks with significant Pb-Pb pair contribution, the green dashed line denotes the Pb-Cl pair peak, and the red dashed line the Pb-Cs pair peak. (b) Differential PDFs (dPDF, D(r)) obtained by subtracting the $CsPbCl_3$ PDF from the PDFs of each of the Yb^{3+}-doped samples. Note that the 0.9% Yb^{3+}:$CsPbCl_3$ D(r) amplitudes are multiplied by 8x to allow representation on the same y scale as the 7.4% Yb^{3+}:$CsPbCl_3$ data.

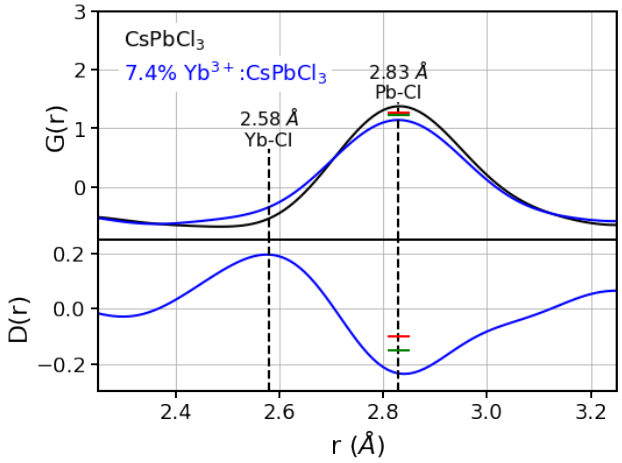

Figure 2.6: Pb-Cl peak region in the PDF of $CsPbCl_3$ (black) and 7.4% Yb^{3+}:$CsPbCl_3$ (blue) and dPDF of 7.4% Yb^{3+}:$CsPbCl_3$ powdered single crystals. The 7.4% Yb^{3+}:$CsPbCl_3$ data show a decrease in the Pb-Cl peak intensity at 2.8 Å and an increase in intensity at ∼2.57 Å, consistent with the loss of Pb^{2+}- Cl^- bonds and the appearance of Yb^{3+}- Cl^- bonds. A similar result is obtained for the 0.9% Yb^{3+}:$CsPbCl_3$ data, but with a diminished signal-to-noise ratio (Figure 2.5b). Red markers indicate predicted changes in the peak intensity for Yb^{3+} substitution without any Pb^{2+} vacancies, and green markers indicate predicted changes with 0.5 Pb^{2+} vacancies per Yb^{3+}.

the red and green markers in Figure 2.6 show the peak values of G(r) and D(r) predicted from PDF simulations based on DFT-calculated defect structures (vide infra).

Figure 2.7 compares the experimental dPDF data for the 7.4% Yb^{3+}:$CsPbCl_3$ sample with dPDFs calculated from each of the AIMD-computed defect structures shown in Figure 2.3. Additionally, two non-local defect scenarios were considered, represented by the sum of two $[Yb_{Pb}]^+$ with one $[V_{Pb}]^{2-}$ and the sum of one $[Yb_{Pb}\text{-}V_{Pb}]^-$ site with one $[Yb_{Pb}]^+$. D(r) profiles were calculated from 1 ps AIMD trajectories run on the various DFT-optimized structures. No difference was observed between the calculated PDFs of the linear vs orthog-

onal $[Yb_{Pb}\text{-}V_{Pb}\text{-}Yb_{Pb}]^0$ arrangements, so the orthogonal was arbitrarily chosen to be shown in these results. Significant features in the data are marked with vertical dashed lines. In general, all simulations give reasonable representations of the data (Figure A.12), reproducing the positions, heights, and peak shapes for the majority of the features. The simulations consistently show a significant decrease of the Cs-Pb distance upon doping, however, whereas the data show a slight increase. This difference is likely due to lattice distortions around the Cs^+ sites, as observed in our DFT calculations [12]. Computational work [12] predicted, for a Yb concentration of 7.4%, 95% of Yb_{Pb} dopants to be within one exciton Bohr radius of a compensating V_{Pb} defect, for example, in the $[Yb_{Pb}\text{-}V_{Pb}\text{-}Yb_{Pb}]^0$ arrangement shown here. Qualitatively, the $[Yb_{Pb}\text{-}V_{Pb}\text{-}Yb_{Pb}]^0$ simulation is most similar to the experimental data, particularly around the Pb-Cl peak. A reduced χ^2 and r-squared goodness-of-fit analysis (not shown) shows statistically similar results for all structures, however, preventing quantitative discrimination between proposed defect structures. This goodness-of-fit is primarily compromised by the difference between experimental and computed distortions of the Cs^+ sub-lattice upon Yb^{3+} doping, which hinders statistical comparisons in the other regions of interest as well.

To compare with the experimental data in Figure 2.5, we also calculated the percent changes in peak intensities (relative to an undoped sample) anticipated from the simulated PDF data for the Pb-Cl, Pb-Cs, and Pb-Pb peaks in the short-range-order region of the data. These results are summarized in Table 2.1 along with the parallel experimental intensity changes, and are illustrated graphically in Figure 2.6 for the Pb-Cl bond distance of the 7.4% Yb^{3+}:$CsPbCl_3$ sample. The Cs-Cl peak was not analyzed due to its breadth and lack of a clear maximum. The selected peaks, marked in Figure 2.5, were chosen to allow quantitative analysis of Pb^{2+} vacancy formation upon Yb^{3+} doping. Although inhomogeneous peak broadening can also decrease peak intensities, peak broadening here results primarily from Yb^{3+} doping and Pb^{2+} vacancy formation (Figure 2.7), thus allowing us to correlate intensity

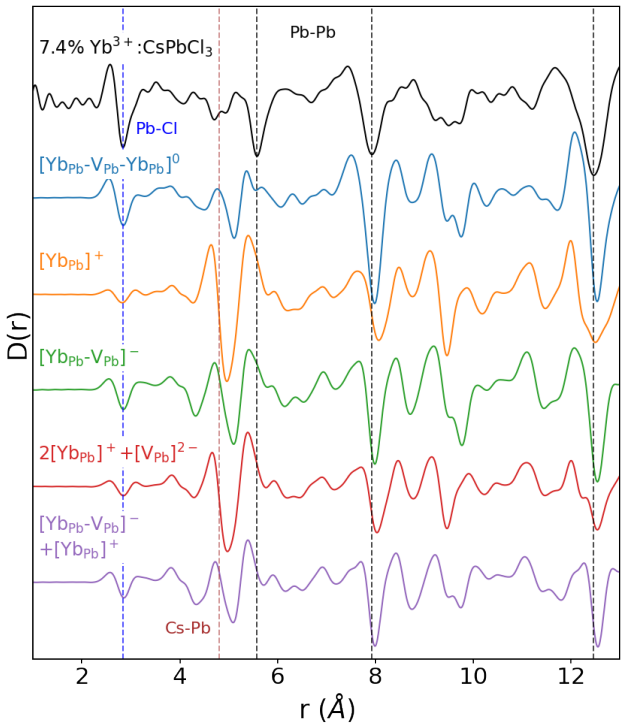

Figure 2.7: Comparison of the experimental differential PDF (dPDF) for 7.4% Yb^{3+}:$CsPbCl_3$ (black) with simulated dPDFs for the various calculated defect structures depicted in Figure 2.3. The bent dimer simulation was arbitrarily chosen for $[Yb_{Pb}\text{-}V_{Pb}\text{-}Yb_{Pb}]^0$. Two additional dPDFs included to account for non-local charge compensation ($2[Yb_{Pb}]^+ + [V_{Pb}]^{2-}$, and $[Yb_{Pb}\text{-}V_{Pb}]^- + [Yb_{Pb}]^+$) were obtained by averaging the PDFs of their specified components. The Pb-Cl peak has been marked with a blue dashed line, and several Pb-Pb peaks are marked with black dashed lines. The position of the Cs-Pb peak in the data, poorly reproduced by the simulations, is marked with a brown dashed line.

Table 2.1: Predicted and experimental percent changes in the intensities of select short-range order peaks in the PDF data (as marked in Figure 2.5) resulting from Yb^{3+} doping. Predicted changes are given for the cases of (i) no Pb^{2+} vacancies (No V_{Pb}) and (ii) 0.5 V_{Pb} per Yb^{3+} dopant (V_{Pb}). The changes observed experimentally are also tabulated. Experimental uncertainties are 0.13 for 0.9% data and 0.12 for 7.4% data.

		0.9% Yb^{3+}:$CsPbCl_3$			**7.4% Yb^{3+}:$CsPbCl_3$**		
		Predicted			Predicted		
	r(Å)	No V_{Pb}	V_{Pb}	Obsd.	No V_{Pb}	V_{Pb}	Obsd.
Pb-Cl	2.83	-0.9	-1.4	-1.2	-7.4	-11.1	-17.0
Pb-Cs	4.80	-0.0	-0.5	-0.8	-0.1	-3.8	-3.6
Pb-Pb	5.60	-0.2	-1.1	-3.0	-1.7	-9.1	-14.9

changes with the presence of Yb_{Pb} and V_{Pb} defects. Expected changes in peak intensities, based on the experimental Yb^{3+} doping levels, are tabulated for the two cases of no Pb^{2+} vacancies (No V_{Pb}) and 0.5 Pb^{2+} vacancies per Yb^{3+} (V_{Pb}), the latter being the expected value for charge neutrality. Critically, V_{Pb} formation is evident from all three Pb-related short-range peaks of both doped samples. Because all three peaks are in the short-range order regime, these changes do not involve contributions from other atom pairs. We therefore conclude that Yb^{3+} doping is accompanied by the formation of Pb^{2+} vacancies in $CsPbCl_3$. Although widely hypothesized and computationally predicted, these data are the first to demonstrate this key structural finding for lanthanide-doped lead-halide perovskites.

Although the PDF data show V_{Pb} formation as the primary charge-compensation mechanism accompanying Yb^{3+} doping, we note that they also appear to show slightly greater peak intensity changes than anticipated for the precise scenario of 0.5 Pb^{2+} vacancies per Yb^{3+} (see Table 2.1). Each peak yields a different quantitative value, but averaging over the

results for all three peaks indicates 0.9 ± 0.6 V_{Pb}/Yb^{3+} in the 0.9% Yb^{3+}:$CsPbCl_3$ sample and 0.9 ± 0.4 V_{Pb}/Yb^{3+} in the 7.4% Yb^{3+}:$CsPbCl_3$ sample, for example. Graphically, Figure 2.6 shows that the experimental change in Pb-Cl peak intensity exceeds that predicted for a ratio of 0.5 V_{Pb}/Yb^{3+}. Such discrepancies could stem from the inability to accurately quantify integrated peak intensities in the PDF data, but in Figure 2.6 we see little evidence of Pb-Cl peak broadening that is not accounted for by the appearance of the neighboring Yb-Cl peak. It is unclear why excess lattice Pb^{2+} vacancies beyond those required for Yb^{3+} charge compensation might form upon Yb^{3+} doping, but there may be other sources of disorder induced by Yb^{3+} doping as well. For example, we observe a reduction in macroscopic single-crystal quality with increasing Yb^{3+} doping that could reflect increased densities of twinning grain boundaries (e.g., Figure A.1). Nevertheless, the average peak-intensity change still falls within experimental uncertainty of that anticipated for 0.5 V_{Pb}/Yb^{3+}, and is consistent with our conclusion that V_{Pb} formation is the primary mode of Yb^{3+} charge compensation.

2.5 Conclusion

A combination of XRD, EXAFS, and PDF data and analysis have been used to measure the structural consequences of doping Yb^{3+} ions into perovskite $CsPbCl_3$ crystal lattices. The results show that ytterbium is incorporated into $CsPbCl_3$ in its 3+ oxidation state, substituting exclusively at Pb^{2+} sites, and adopting a pseudo-octahedral Cl^- coordination environment similar to that of Pb^{2+} but with contracted bond lengths. EXAFS and PDF measurements both show Yb^{3+}-Cl^- bond lengths of 2.58 Å, compared to the Pb^{2+}-Cl^- distances of 2.83 Å. The PDF data also show evidence of extensive Pb^{2+} vacancy formation upon Yb^{3+} doping, indicating this as the primary mechanism for compensation of the excess positive charges of Yb^{3+} dopants. These conclusions are bolstered by comparison of dPDF data with simulations. As such, the results of this study represent the first experimental evidence of correlated Yb^{3+} doping and Pb^{2+} vacancy formation in Yb^{3+}-doped $CsPbCl_3$,

a motif that has been frequently hypothesized but never observed, and that is believed to play an important mechanistic role in the unique quantum cutting displayed by this material. Overall, this work advances our basic structural understanding of lanthanide-doped lead-halide perovskites in ways that will help to develop a deeper understanding of structure/function relationships in this class of materials, from lattice stabilization to quantum cutting.

2.6 Acknowledgements

This research was primarily supported by the UW Molecular Engineering Materials Center, an NSF Materials Research Science and Engineering Center (Grant No. DMR-1719797). This research used resources of the Advanced Photon Source, a U.S. Department of Energy (DOE) Office of Science User Facility operated for the DOE Office of Science by Argonne National Laboratory under Contract No. DE-AC02-06CH11357. We acknowledge Steve Heald from APS Sector 20 (BL 20-ID) (GUPs 69365, 73609, & 74833) and Olaf Borkiewicz and Leighanne Gallington from Sector 11 (BL 11-ID) (GUP 73957) for collecting these data sets. We also thank Micah P. Prange for his assistance with EXAFS theory and calculations.

2.7 References

[1] Y. Zhou, J. Chen, O. M. Bakr, and H.-T. Sun, Chem. Mater. 30, 6589 (2018).

[2] J. Shi, F. Li, J. Yuan, X. Ling, S. Zhou, Y. Qian, and W. Ma, J. Matter. Chem. A 7, 20936 (2019).

[3] D. Zhou, R. Sun, W. Xu, N. Ding, D. Li, X. Chen, G. Pan, X. Bai, and H. Song, Nano Lett. 19, 6904 (2019).

[4] W. J. Mir, T. Sheikh, H. Arfin, Z. Xia, and A. Nag, NPG Asia Mater. 12, 9 (2020).

[5] S. M. Ferro, M. Wobben, and B. Ehrler, Mater. Horiz. 8, 1072 (2021).

[6] D. Zhou, D. Liu, G. Pan, X. Chen, D. Li, W. Xu, X. Bai, and H. Song, Adv. Mater. 29,

1704149 (2017).

[7] G. Pan, X. Bai, D. Yang, X. Chen, P. Jing, S. Qu, L. Zhang, D. Zhou, J. Zhu, W. Xu, B. Dong, and H. Song, Nano Lett. 17, 8005 (2017).

[8] T. J. Milstein, D. M. Kroupa, and D. R. Gamelin, Nano Lett. 18, 3792 (2018).

[9] T. J. Milstein, K. T. Kluherz, D. M. Kroupa, C. S. Erickson, J. J. De Yoreo, and D. R. Gamelin, Nano Lett. 19, 1931 (2019).

[10] M. J. Crane, D. M. Kroupa, and D. R. Gamelin, Energy Environ. Sci. 12, 2486 (2019).

[11] J. Y. D. Roh, M. D. Smith, M. J. Crane, D. Biner, T. J. Milstein, K. W. Krämer, and D. R. Gamelin, Phys. Rev. Mater. 4, 105405 (2020).

[12] D. E. Sommer, D. R. Gamelin, and S. T. Dunham, Phys. Rev. Mater. 6, 025404 (2022).

[13] T. J. Milstein, J. Y. D. Roh, L. M. Jacoby, M. J. Crane, D. E. Sommer, S. T. Dunham, and D. R. Gamelin, Chem. Mater. 34, 3759 (2022).

[14] B. W. Bryant, J. Opt. Soc. Am. 55, 771 (1965).

[15] M. Zeng, F. Artizzu, J. Liu, S. Singh, F. Locardi, D. Mara, Z. Hens, and R. Van Deun, ACS Appl. Nano Mater. 3, 4699 (2020).

[16] W. J. Chang, S. Irgen-Gioro, S. Padgaonkar, R. López-Arteaga, and E. A. Weiss, J. Phys. Chem. C 125, 25634 (2021).

[17] M. Stefanski, V. Boiko, M. Ptak, and W. Strek, J. Alloys Compounds 905, 164216 (2022).

[18] Z.-J. Yong, S.-Q. Guo, J.-P. Ma, J.-Y. Zhang, Z.-Y. Li, Y.-M. Chen, B.-B. Zhang, Y. Zhou, J. Shu, J.-L. Gu, L.-R. Zheng, O. M. Bakr, and H.-T. Sun, J. Am. Chem. Soc. 140, 9942 (2018).

[19] J.-P. Ma, Y.-M. Chen, L.-M. Zhang, S.-Q. Guo, J.-D. Liu, H. Li, B.-J. Ye, Z.-Y. Li, Y. Zhou, B.-B. Zhang, O. M. Bakr, J.-Y. Zhang, and H.-T. Sun, J. Matter. Chem. C 7, 3037 (2019).

[20] J. Ma, Q. Yao, J. A. McLeod, L.-Y. Chang, C.-W. Pao, J. Chen, T.-K. Sham, and L.

Liu, Nanoscale 11, 6182 (2019).

[21] C. Bi, S. Wang, Q. Li, S. V. Kershaw, J. Tian, and A. L. Rogach, J. Phys. Chem. Lett., 943 (2019).

[22] F. Bertolotti, L. Protesescu, M. V. Kovalenko, S. Yakunin, A. Cervellino, S. J. L. L. Billinge, M. W. Terban, J. S. Pedersen, N. Masciocchi, and A. Guagliardi, ACS Nano 11, 3819 (2017).

[23] P. Cottingham, and R. L. Brutchey, Chem. Mater. 30, 6711 (2018).

[24] See Supplemental Material at [URL will be inserted by publisher] for additional characterization figures and tables of EXAFS fitting parameters.

[25] M. J. Crane, D. M. Kroupa, J. Y. Roh, R. T. Anderson, M. D. Smith, and D. R. Gamelin, ACS Appl. Energy Mater. 2, 4560 (2019).

[26] B. Ravel, and M. Newville, J. Synch. Rad. 12, 537 (2005).

[27] J. J. Rehr, and R. C. Albers, Rev. Mod. Phys. 72, 621 (2000).

[28] J. J. Rehr, J. J. Kas, M. P. Prange, A. P. Sorini, Y. Takimoto, and F. Vila, Compt. Rend. Phys. 10, 548 (2009).

[29] J. J. Rehr, J. J. Kas, F. D. Vila, M. P. Prange, and K. Jorissen, Phys. Chem. Chem. Phys. 12, 5503 (2010).

[30] A. Hoeher, S. Mergelsberg, O. J. Borkiewicz, P. M. Dove, and F. M. Michel, Acta Cryst. Sect. A 75, 758 (2019).

[31] B. H. Toby, and R. B. Von Dreele, J. Appl. Cryst. 46, 544 (2013).

[32] P. Juhás, T. Davis, C. L. Farrow, and S. J. L. Billinge, J. Appl. Cryst. 46, 560 (2013).

[33] X. Qiu, J. W. Thompson, and S. J. L. Billinge, J. Appl. Cryst. 37, 678 (2004).

[34] C. L. Farrow, P. Juhas, J. W. Liu, D. Bryndin, E. S. Božin, J. Bloch, T. Proffen, and S. J. L. Billinge, J. Phys.: Cond. Matter 19, 335219 (2007).

[35] M. R. Linaburg, E. T. McClure, J. D. Majher, and P. M. Woodward, Chem. Mater. 29, 3507 (2017).

[36] T. Proffen, and R. B. Neder, J. Appl. Cryst. 30, 171 (1997).

[37] G. Kresse, and J. Furthmüller, Comp. Mater. Sci. 6, 15 (1996).

[38] G. Kresse, and J. Furthmüller, Phys. Rev. B 54, 11169 (1996).

[39] P. E. Blöchl, Phys. Rev. B 50, 17953 (1994).

[40] J. P. Perdew, A. Ruzsinszky, G. I. Csonka, O. A. Vydrov, G. E. Scuseria, L. A. Constantin, X. Zhou, and K. Burke, Phys. Rev. Lett. 100, 136406 (2008).

[41] C. Freysoldt, B. Grabowski, T. Hickel, J. Neugebauer, G. Kresse, A. Janotti, and C. G. Van de Walle, Rev. Mod. Phys. 86, 253 (2014).

[42] H. J. Monkhorst, and J. D. Pack, Phys. Rev. B 13, 5188 (1976).

[43] J. A. McLeod, Z. Wu, B. Sun, and L. Liu, Nanoscale 8, 6361 (2016).

[44] M. Atanasov, C. Daul, H. U. Güdel, T. A. Wesolowski, and M. Zbiri, Inorg. Chem. 44, 2954 (2005).

Chapter 3

STRUCTURE AND STABILITY OF THE IODIDE ELPASOLITE, CS_2AGBII_6

Reproduced with permission from: Kluherz, K. T.; Mergelsberg, S. T.; De Yoreo, J. J.; Gamelin, D. R. Structure and Stability of the Iodide Elpasolite, Cs_2AgBiI_6. *Manuscript submitted*

3.1 Overview

Iodide elpasolites (or double perovskites, $A_2B'B''I_6$, B' = M^+, B" = M^{3+}) are predicted to be promising alternatives to lead-based perovskite semiconductors for photovoltaic and optoelectronic applications, but no iodide elpasolite has ever been definitively prepared or structurally characterized. Iodide elpasolites are widely predicted to be unstable due to favorable decomposition to the competing $A_3B_2I_9$ (B = M^{3+}) phase. Here, we report the results of synchrotron XRD and X-ray total scattering measurements on putative Cs_2AgBiI_6 nanocrystals made via anion exchange from parent $Cs_2AgBiBr_6$ nanocrystals. Rietveld refinement of XRD and PDF data shows that these nanocrystals indeed exhibit a tetragonal (I4-m) elpasolite structure, making them the first example of a structurally characterized iodide elpasolite. A series of experiments probing structural relaxation and the effects of surface ligation or grain size all point to the critical role of surface free energy in stabilizing the iodide elpasolite phase in these nanocrystals.

3.2 Introduction

Lead-halide perovskites ($APbX_3$) have been extensively studied due to their excellent optoelectronic properties and many potential applications, including photovoltaics, lighting, and X-ray detection.[1,2] Recently, attention has turned to the possibility that elpasolites (or double perovskites, $A_2B'B''I_6$, where B' = M^+, B" = M^{3+}) may serve as promising lead-free alternatives to the lead-halide perovskites.[3] Although elpasolites generally do not exhibit the excellent emissive properties of the lead-halide perovskites, some do show long carrier lifetimes and broad absorption, making them potentially suitable for applications in photovoltaics.[3-6] Some elpasolites also exhibit superior thermal and water stability compared to lead-halide perovskites, making them also potentially attractive for devices that experience high temperatures under standard operation.[7-10] Numerous theoretical studies of elpasolites have predicted that iodide elpasolites in particular should exhibit the most suitable band gaps for photovoltaic applications.[4,11-17]

Despite this broad interest and motivation, iodide elpasolites remarkably remain almost entirely unexplored experimentally. In fact, a recent review article[11] has highlighted that to date there have been no "structurally characterized" iodide elpasolites reported at all, asserting that their successful synthesis has so far been elusive. Computational models generally predict that iodide elpasolites are thermodynamically unstable relative to competing phases, explaining the paucity of experimental results. Although their enthalpies of formation may be favorable (e.g., ΔH_f = -0.86 eV/atom for $2\,CsI + BiI_3 + AgI \longrightarrow Cs_2AgBiI_6$),[18] they also appear to suffer from favorable decomposition to the $A_3B_2X_9$ (B = M^{3+}) or A_3BX_6 phases[11,18] (e.g., ΔH_f = -0.41 eV/atom for $2\,Cs_2AgBiI_6 \longrightarrow Cs_3Bi_2I_9 + 2\,AgI + CsI$).[4] The XRD patterns of these primary competing phases can appear very similar to those of the elpasolites, complicating experimental analysis.[8,19,20] We note that the thermodynamic properties of elpasolite nanocrystals likely differ significantly from these bulk estimates, but to our knowledge, no theoretical investigations have yet examined the stabilities of nanoscale

elpasolites.

Nevertheless, syntheses of a few iodide elpasolites have been claimed, suggesting that it may be possible to stabilize this family of materials under specific circumstances. Cs_2NaLaI_6 was reported by Glodo *et al*[21] in 2006 and by Gundiah *et al.*[22] in 2014, but the lack of structural characterization leaves unclear whether the material was actually an elpasolite. Zhang *et al.* reported powder XRD (pXRD) data for Cs_2NaBiI_6 in 2018,[23] along with Zheng *et al.* in 2022,[24] but in both cases the clear presence of a $Cs_3Bi_2I_9$ contaminant and the strongly overlapping peaks of the two phases made definitive structural identification uncertain. Rb_2AgBiI_6 was reported by Bhorde *et al.* in 2021,[25] but with poor agreement between the experimental pXRD and the diffraction pattern calculated from a DFT model. Shadabroo *et al.*[26] reported formation of MA_2AgBiI_6 in 2021, and Cs_2AgBiI_6 nanocrystals were reported by our group in 2018,[8] but both were only structurally characterized with pXRD data that was insufficient to unambiguously identify them as iodide elpasolites. As a cautionary note, a thorough structural study of another potential iodide elpasolite, Cu_2AgBiI_6, using 100 K single-crystal XRD measurements found this material to exhibit a non-elpasolite trigonal R3-m structure with layers of 2D edge-sharing octahedra alternating with vacant octahedral sites.[20,27] The authors proposed that this alternating layer structure provides stability over the elpasolite structure in this case. Overall, there is thus little to no unambiguous evidence for the existence of any bone fide iodide elpasolites, making this family a remarkable void in the composition space of this important class of materials.

Here, we follow up on our previous claim[8] of Cs_2AgBiI_6 elpasolite nanocrystals by reporting rigorous structural characterization of these nanocrystals via Rietveld refinement of synchrotron high-energy XRD (heXRD) data, analyzed in tandem with X-ray total scattering data. The data and analysis presented here yield the first unambiguous structure model of an iodide elpasolite, showing these nanocrystals to adopt the tetragonal I4-m structure. We further demonstrate the critical role of nanostructuring, and especially of surface ligation,

in stabilizing this phase and preventing decomposition to the competing $Cs_3Bi_2I_9$ product. These results firmly establish the existence of iodide elpasolites, a family of materials predicted to excel in optoelectronics applications but never previously available for experimental investigation. More broadly, these results highlight the power of chemistries unique to the nanoscale for accessing unprecedented compositions of matter.

3.3 Experimental

3.3.1 Materials

$Bi(OAc)_3$, Ag(OAc), Cs(OAc), trimethylsilyl iodide (TMSI), trimethylsilyl bromide (TMSBr), octadecene (90%), oleic acid (OA) (90%), oleylamine (OLA) (70%), 3-(N,N-dimethyl-octadecylammonio)-propanesulfonate (sulfobetaine, >99%), benzyl alcohol (anhydrous, 99.8%), didodecyl-dimethylammonium bromide (DDDMABr), and trioctylphosphine (TOP, anhydrous, 90%) were purchased from Sigma Aldrich and used without further purification. Hydrated reagents (OA, OLA, sulfobetaine, DDDMABr) were dried under vacuum for 4 h then transferred into a glovebox before use in small-molecule addition experiments.

3.3.2 Synthesis and anion exchange

$Cs_2AgBiBr_6$ nanocrystals (NCs) were synthesized using the procedure we reported previously (see ref. [8] for details). Cs_2AgBiI_6 NCs were made from these $Cs_2AgBiBr_6$ NCs via anion exchange using TMSI.[8,28] In a standard complete anion-exchange reaction, 1 mL of neat TMSI was added to 5 mL of a ~10 μM $Cs_2AgBiBr_6$ NC solution in hexanes and the reaction vial sealed for 1 day. The solution changed color from yellow to dark brown-red within ~10 s, but was allowed to sit to ensure complete anion exchange. Absorption, XRD, and EDX data were collected to monitor reaction progress. Thin-film samples of $Cs_2AgBiBr_6$ were prepared by thermal evaporation as described previously.[29] Films were initially characterized in ambient atmosphere. For anion-exchange reactions, films were exposed to aliquots of TMSI

vapor in a sealed glass vessel under inert atmosphere. For sequential TMSI exposures, the vessel's atmosphere was flushed with nitrogen between exposures. For both NC and thin-film heating experiments, samples (on Si and glass substrates) were heated directly on a temperature-controlled hot plate in a nitrogen glovebox.

3.3.3 Small-molecule additions

Small-molecule additions were performed in the following way: 5, 10, 20, or 100 μmol of the selected compound (OA, OLA, benzyl alcohol, sulfobetaine, DDDMABr, and TOP) was added to 0.5 mL of 10 μM Cs_2AgBiX_6 (X = Br, I) NC solutions in hexanes, briefly stirred, then allowed to react overnight ($\sim$20 h). With the exception of sulfobetaine, which was added as a solid powder, 0.1 M solutions of each compound in hexanes were used for these reactions. We primarily report results of the 20 μmol additions. After additions, $Cs_2AgBiBr_6$ samples were characterized using UV-Vis absorption, XRD, and TEM, then exposed to 100 μL TMSI for anion exchange.

3.3.4 Sample Characterization

Absorption spectra were collected using an Agilent Cary 60. Benchtop powder XRD data were measured using a Bruker D8 Discover with a high-efficiency IμS microfocus X-ray source for Cu Kα radiation operating at 50,000 mW (50 kV, 1 mA). NC samples were prepared by drop-casting NC stock solutions on silicon substrates. Samples were measured under Kapton film to prevent air exposure during measurement. TEM images were acquired using an FEI Tecnai G2 F20 supertwin microscope operating at 200 kV. A C2 aperture of 70 μm was used to minimize beam damage. TEM EDX measurements were acquired using an EDAX-Elite-T detector. TEM measurements with in situ heating were performed using a FEI Titan 80-300 Environmental Transmission Electron Microscope (ETEM) with image correction. A Gatan double-tilt, furnace-based heating holder (Model 646) was used for sample heating. Samples

were first imaged, then heated to 100 or 120°C for 10-30 min, then cooled to 30°C before further imaging to avoid beam damage. NC stock solutions (10 μM) were diluted by about one-fifth, and 5 μL of the solution was deposited onto ultrathin carbon Type A 400 Cu grids from TED Pella, Inc. SEM images were taken using an Apreos-S, and EDX mapping was performed at 10 kV, 800 pA, with a 100 ms dwell time.

3.3.5 PDF measurements

X-ray total scattering data were collected using beamline 11-ID-B at the Advanced Photon Source at Argonne National Laboratory.[30] Solutions of NC samples were measured at room temperature in quartz or Kapton capillaries using monochromatic X-rays with energy ~86.7 keV (λ = 0.1432 Å). Using a Perkin Elmer 1621 a-Si area detector (200 μm^2 pixel size), the sample-to-detector distance and detector non-orthogonality were calibrated with a CeO2 standard (NIST 674a) diluted with glassy carbon. X-ray total scattering data were integrated using the GSAS-II software[31] and a radial bin size of 1396, 1200, or 1000 for sample-to-detector distances of 250, 1000, and 1500 mm, respectively. Background subtraction and PDF processing were performed using the PDFgetX3 software.[32] For PDF processing, a Qmax of 28 $Å^{-1}$ and rmax of 30 Å were used. The PDFgui package[33] was used to determine the instrument parameters of q_{damp} = 0.025 and q_{broad} = 0.047, and to run r-space refinements to the PDF data. Rietveld refinements were calculated using the GSAS-II software,[31] with an analytic Hessian algorithm run for 3 cycles for each refinement. Unit cell, background (chebyschev-1 function, 9 to 15 terms), atom positions, and thermal parameters were refined. Fourier transforms of the backgrounds show no significant contribution of the elpasolite or secondary crystalline phases (Fig. B.4).

3.4 Results and Analysis

3.4.1 Structural Characterization

Figure 3.1 shows XRD and TEM data collected for Cs_2AgBiI_6 NC samples prepared by the method we reported previously.[8] As noted in ref. 8, Cs_2AgBiI_6 NCs will not form by direct hot-injection synthesis under our reaction conditions, and they are instead prepared via anion exchange from parent $Cs_2AgBiBr_6$ NCs that can be synthesized directly. The XRD data in Fig. 3.1a are consistent with the predicted XRD pattern for the Cs_2AgBiI_6 elpasolite phase (Fig. B.2),[8] and notably show no identifiable peaks from the competing $Cs_3Bi_2I_9$ phase. The TEM data in Fig. 1b show cubic or near-cubic particles with an average edge length of ∼14 nm (Fig. 3.1c) measured across ∼200 particles. Overall, these data are essentially indistinguishable from the results we reported previously, demonstrating reproducibility of the synthesis methods from Creutz et al,8 and indicating that the findings of this study are applicable to the materials reported in that previous study.

Although compelling, the XRD data in Fig. 3.1a are insufficient to unambiguously determine the structure of Cs_2AgBiI_6 NCs. In particular, the data do not allow distinction among the three variants of elpasolites, the cubic (Fm-3m), tetragonal (I4-m), and trigonal (R-3m) structures. More powerful structural data were therefore obtained. Figure 3.2 shows high-energy X-ray scattering data collected for the same Cs_2AgBiI_6 NCs using a synchrotron source at the APS. Using these data, we calculated Rietveld refinement structure fits to the cubic, tetragonal, and trigonal elpasolite structures using GSAS-II.[31] The trigonal structural model yielded a poor fit with an overall weighted R factor (R_w) of 13.7 (see Fig. B.6) and was not considered further. The cubic Fm-3m structural model gave a better fit, with an R_w of 7.8 and low residual values (see Fig. B.3), but inspection of the computed structure revealed unusually large thermal disorder within the Ag^+ sublattice (Fig. B.3c). To test the effect of these thermal parameters on the Fm-3m fit, we performed a second Rietveld refine-

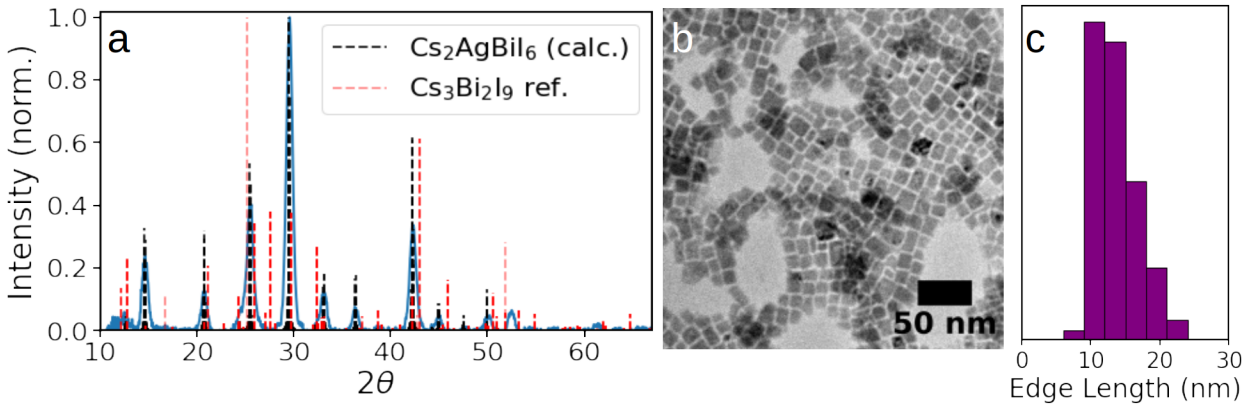

Figure 3.1: **(a)** Powder XRD data collected for Cs_2AgBiI_6 nanocrystals prepared by anion exchange from $Cs_2AgBiBr_6$ nanocrystals. A calculated pattern based on a hypothesized cubic (Fm-3m) Cs_2AgBiI_6 unit cell was used for initial identification. $Cs_3Bi_2I_9$ was selected for comparison as the most similar known competing phase. **(b)** TEM image of Cs_2AgBiI_6 nanocrystals. **(c)** Histogram of Cs_2AgBiI_6 nanocrystal sizes measured from TEM images of ∼200 nanocrystals.

ment fixing these values to the literature thermal parameters found for Ag^+ in $Cs_2AgBiBr_6$ (ICSD# 239875), which is known to be cubic (Fm-3m).[34] This restriction yielded a substantially poorer fit (Fig. B.5), with $R_w = 12.9$, and generated notable new residual peaks around 1.8 $Å^{-1}$ and 3.1 $Å^{-1}$. Close inspection found these large residuals to correlate with low-symmetry splittings of the (3,1,1) and (5,3,1) peaks, pointing to a lower-symmetry structure. Rietveld refinement using a tetragonal I4-m structure (Fig. 3.2a) yielded an improved fit ($R_w = 6.7$) to the data. Notably, the lower R_w relative to the Fm-3m fit correlates with thermal parameters closer to computed values for all atoms (Fig. 3.2c), consistent with values found in other elpasolite structures in the ICSD (Coll. Codes 239875, 11523, 18989, 21475, 32193). We therefore conclude that our Cs_2AgBiI_6 NCs are best described by a tetragonal I4-m elpasolite structure. This structure (Fig. 3.2b) is characterized by lattice parameters of a = b = 8.535(4) Å and c = 12.080(4) Å, a unit cell volume of 880 $Å^3$, and a distorted Bi-I octahedron with Bi-I bond distances of 2.91 (4 bonds) and 3.03 Å (2 bonds). The full structural details have been deposited in the Inorganic Crystal Structure Database hosted by the Cambridge Crystallographic Data Centre (CCDC). To our knowledge, these results represent the first complete structural characterization of any iodide elpasolite.

To supplement the above analysis of the Cs_2AgBiI_6 structure, we additionally investigated the structure's evolution during conversion of the NCs from cubic $Cs_2AgBiBr_6$ to tetragonal Cs_2AgBiI_6 by anion exchange. Figure 3.3 presents the heXRD and pair distribution functions (PDF) from X-ray total scattering data collected for a series of intermediate anion-exchange reactions. Dashed lines in Fig. 3.3b trace the progression of peak positions across the sample series for ease of viewing. Figure 3.3c,d summarizes these data by plotting formula unit volume (Vf) and PDF peak positions vs the fractional iodide content x in $Cs_2AgBi(Br_{1-x}I_x)_6$ measured by EDX. All of these data show a linear dependence on x, increasing to accommodate the larger iodide anions. Both the heXRD and the PDF (Fig. 3.3a,b) data thus reveal continuous shifts in feature positions across the entire sample set, with no abrupt or

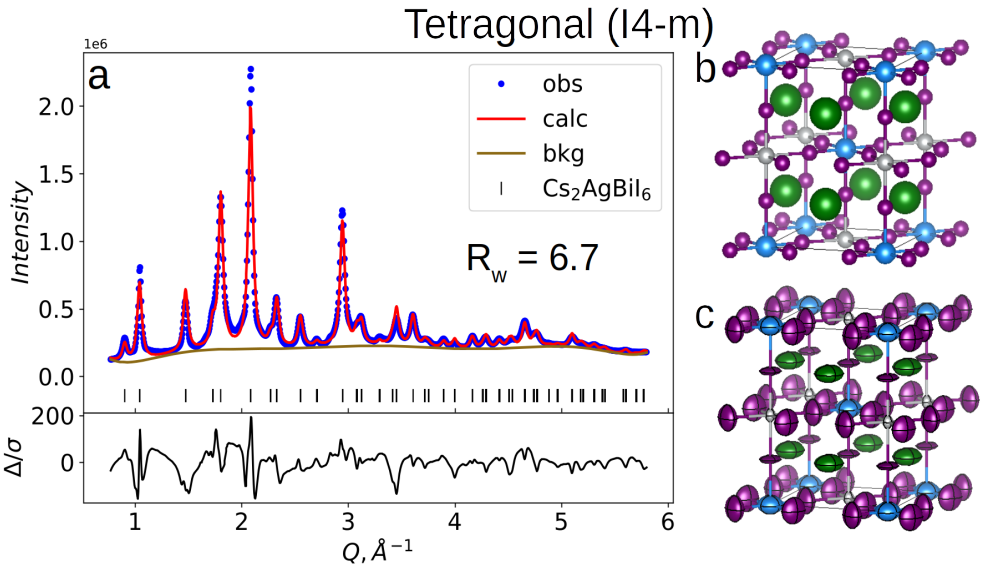

Figure 3.2: Rietveld refinement results using synchrotron X-ray scattering data for Cs_2AgBiI_6 nanocrystals suspended in hexanes solution. (a) Data (blue dots), calculated pattern (red curve), background (brown curve), predicted peak positions (vertical black lines), and residual of fit (Δ/σ) obtained using tetragonal I4-m structure. (b) Tetragonal I4-m structure model. Silver: Ag^+; blue: Bi^{3+}; green: Cs^+; purple: I^-. (c) Structure model produced from (b), showing 95% atomic-displacement parameters refined using PDF data.

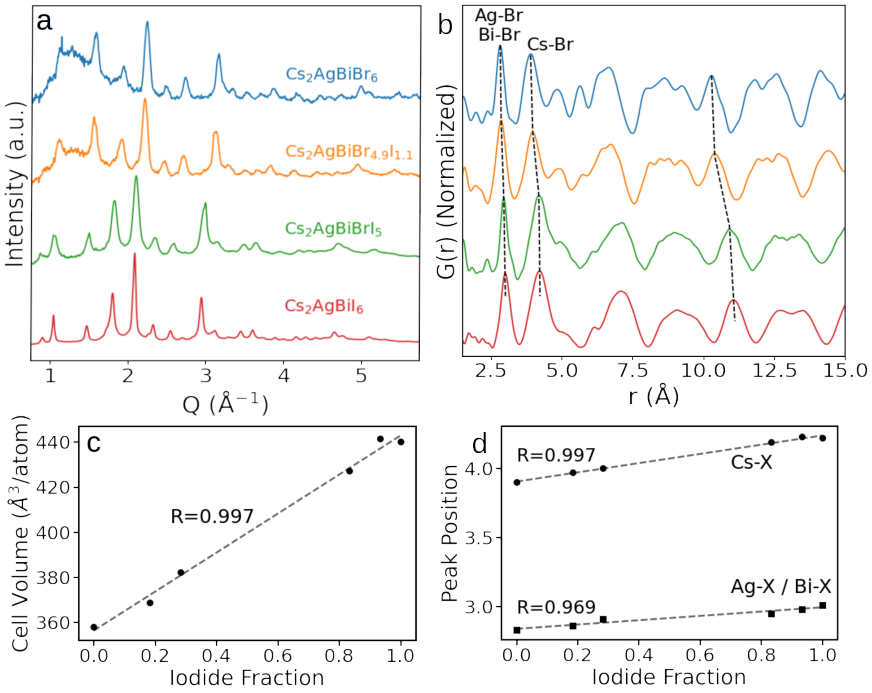

Figure 3.3: (a) High-energy XRD data for select $Cs_2AgBi(Br_{1-x}I_x)_6$ nanocrystal samples from a stepwise anion-exchange reaction series, plotted in Q-space. (b) Atomic Pair Distribution Functions (PDFs, G(r)) for the same nanocrystal series, calculated from X-ray total scattering data. Specific peaks in the short-range order of $Cs_2AgBiBr_6$ are labelled. Dashed lines trace peak positions across multiple samples. Fourier noise shows up as minor ripples in the PDF data. (c) Formula unit volumes obtained from Rietveld refinements of the full series of anion-exchanged samples, plotted as a function of fractional iodide content x in $Cs_2AgBi(Br_{1-x}I_x)_6$, where x is determined independently by EDX measurements. (d) Positions of the first two peaks (Ag-X/Bi-X and Cs-X) in the PDF data of panel (b), plotted as a function of fractional iodide content x. R values and linear best fits are shown for linear regressions to each peak.

discontinuous transitions between the two end points. PDF is especially useful in analysis of this conversion due to its high sensitivity to the presence of minority phases, which appear as new peaks or shoulders in G(r) regardless of crystallinity.[35-37] Notably, the data in Fig. 3.3b show no new peaks emerging during anion exchange, again supporting a gradual structural evolution with anion exchange. Minor signal fluctuations in the PDF data of some of the intermediate compositions are attributable to Fourier noise. The data in Fig. 3.3 thus show no evidence of mixed-phase or exsolved-phase compositions at any of the intermediate stages of anion exchange, and we conclude that these materials transition continuously from the cubic $Cs_2AgBiBr_6$ structure to the tetragonal Cs_2AgBiI_6 structure via incremental lattice expansion during anion exchange. This conclusion is similar to that drawn for lead-halide perovskite NCs (CsPbX3), which also convert from chloride to bromide to iodide compositions with no detectable intermediate or exsolved phases.[28,38-40] Importantly, the gradual evolution of these data in conjunction with the fact that $Cs_2AgBiBr_6$ is a well-established elpasolite structure bolsters our conclusion that Cs_2AgBiI_6 retains an elpasolite structure as well.

3.4.2 Stability of the iodide elpasolite structure

After establishing that these iodide NCs form the tetragonal I4-m elpasolite structure, we turn to the question of phase stability, in view of the absence of any other structurally characterized iodide elpasolites and the theoretical predictions that these structures should spontaneously decompose into more stable phases.[4,6,10,12] We may consider two general hypotheses: (1) this iodide elpasolite structure is kinetically trapped, perhaps as a result of anion exchange from a parent bromide elpasolite, and (2) this iodide elpasolite structure is thermodynamically stable, but only because of its surface free energy when prepared at the nanoscale. On one hand, our unsuccessful attempts to prepare Cs_2AgBiI_6 NCs directly via hot-injection synthesis using TMSI[8] leave anion exchange from the corresponding bromide

NCs as the only synthesis route, which could suggest that the Cs_2AgBiI_6 composition is kinetically trapped. On the other hand, it is difficult to reconcile the notion of a kinetic barrier to ion reorganization with the observation of high ion mobility in these materials during anion exchange. This consideration could suggest instead that the iodide elpasolite NCs are thermodynamically favorable but their direct synthesis is impeded by other kinetically competitive processes, mainly $Cs_3Bi_2I_9$ formation.[8] Stabilization of metastable polymorphs at the nanoscale is well known,[41-43] generally resulting from increased importance of surface free energy, and Cs_2AgBiI_6 may be a new example of this phenomenon.

Investigating the possibility that surface energy stabilizes these Cs_2AgBiI_6 NCs, we considered two potential sources: structural relaxation at the surface, and reduction in interfacial free energy due to ligand adsorption. We therefore sought to test both of these hypotheses. To investigate the first, we performed fits to the PDF data for both the tetragonal and cubic structural models (see SI, Fig. B.8, B.9) and examined these for evidence of structural relaxation. These fits show the greatest differences in the short-range order, consistent with greater deviation from periodicity at the surfaces (which contribute disproportionately to the short-range order for 14 nm NCs), hence suggesting lattice relaxation associated with the crystallite surfaces. We thus hypothesize that surface relaxation may play an important role in stabilizing the elpasolite phase on the nanoscale, despite its expected thermodynamic instability in bulk.[12]

If reduction in interfacial free energy due to ligand adsorption enhances the stability of these iodide elpasolite NCs, then their stability might be expected to depend on the types and quantities of surface ligands present. To investigate the influence of surface ligation, we performed a series of small-molecule addition experiments in conjunction with the anion-exchange reactions described above, monitored by a combination of XRD, absorption spectroscopy, and TEM. For reference, Fig. 3.4 highlights key contrasts between the absorption spectra and XRD patterns of Cs_2AgBiI_6 and its primary decomposition product, $Cs_3Bi_2I_9$.

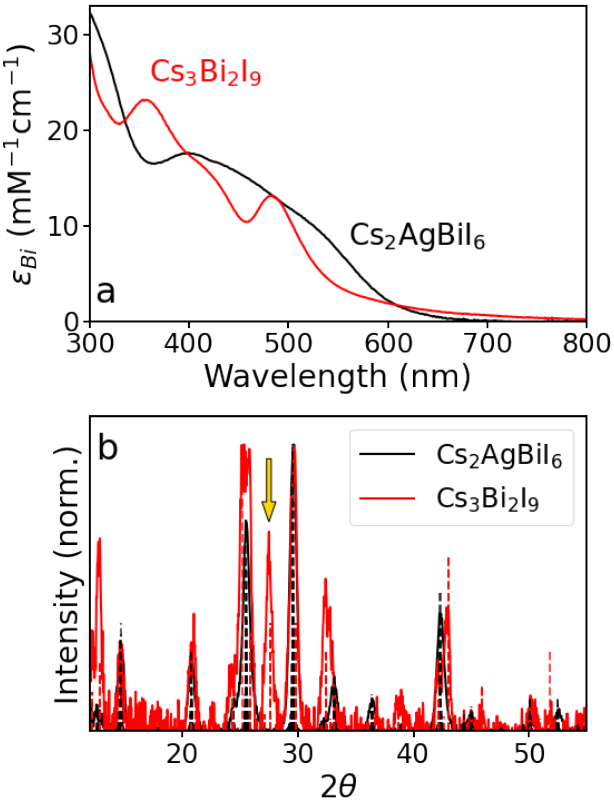

Figure 3.4: Comparison of (a) absorption spectra (with molar extinction coefficients referenced to Bi^{3+}) and (b) XRD patterns for Cs_2AgBiI_6 and $Cs_3Bi_2I_9$ nanocrystals, both made via hot-injection. The absorption spectra show clear differences in peak positions and shapes between the two compositions. Note that there is some uncertainty in the precise extinction coefficients due to potential error from determination of the Bi^{3+} concentrations. The arrow in (b) highlights a major reflection present in $Cs_3Bi_2I_9$ that is lacking in Cs_2AgBiI_6. These contrasts can be used to distinguish between these two phases.

The Cs_2AgBiI_6 absorption spectrum is characterized by a broad onset with shoulders at 390 and 530 nm, whereas $Cs_3Bi_2I_9$ shows more pronounced peaks at 356 and 481 nm, along with a shoulder around 420 nm. As noted previously,[8] Cs_2AgBiI_6 and $Cs_3Bi_2I_9$ XRD patterns are very similar, due to their similar unit cells, but a signature peak at 27.5° can be used to identify the presence of $Cs_3Bi_2I_9$. Such contrasts help to distinguish between these two compounds and to track any NC decomposition.

Figure 3.5 shows XRD data for representative anion-exchange and small-molecule addition reactions, and additional data are provided in the SI. Figure 3.5a shows results from anion exchange using TMSI (i.e., $Cs_2AgBiBr_6$ + TMSI → Cs_2AgBiI_6 + TMSBr)[8,28] followed by addition to the NC solution of one of a set of small molecules investigated that included OA, OLA, sulfobetaine, DDDMABr, and benzyl alcohol. Our NC synthesis was performed in the presence of a mixture of OA and OLA, and further additions of each of these native ligands were thus tested. Sulfobetaine was chosen as a zwitterionic ligand based on its effectiveness in binding to lead-halide perovskite NC surfaces.[44] DDDMABr was selected as an example of a quaternary ammonium species that binds strongly to the surfaces of $CsPbBr_3$ NCs.[45] Benzyl alcohol has been reported to influence ligand binding in perovskite NCs,[46] and may remove surface ligands.[47] Each of these compounds was added to 1 μM NC solutions at concentrations ranging from 1 to 100 μM. For comparison, Fig. 3.5b shows results from inverting the sequence of additions, i.e., small-molecule addition to a $Cs_2AgBiBr_6$ NC solution, followed by anion exchange. From these data, we observe that the $Cs_2AgBiBr_6$ NCs retain their elpasolite structure upon exposure to all of the compounds tested here, whereas the Cs_2AgBiI_6 NCs are far more sensitive, retaining the elpasolite phase with OA or sulfobetaine but transforming to other phases for all other additives examined. The data for the $Cs_2AgBiBr_6$ NCs did show small impurity peaks after exposure to OLA (Fig. B.14), but these NCs were substantially more stable than the Cs_2AgBiI_6 NCs against degradation by this ligand even at high OLA concentrations, and the dominant phase remained the elpa-

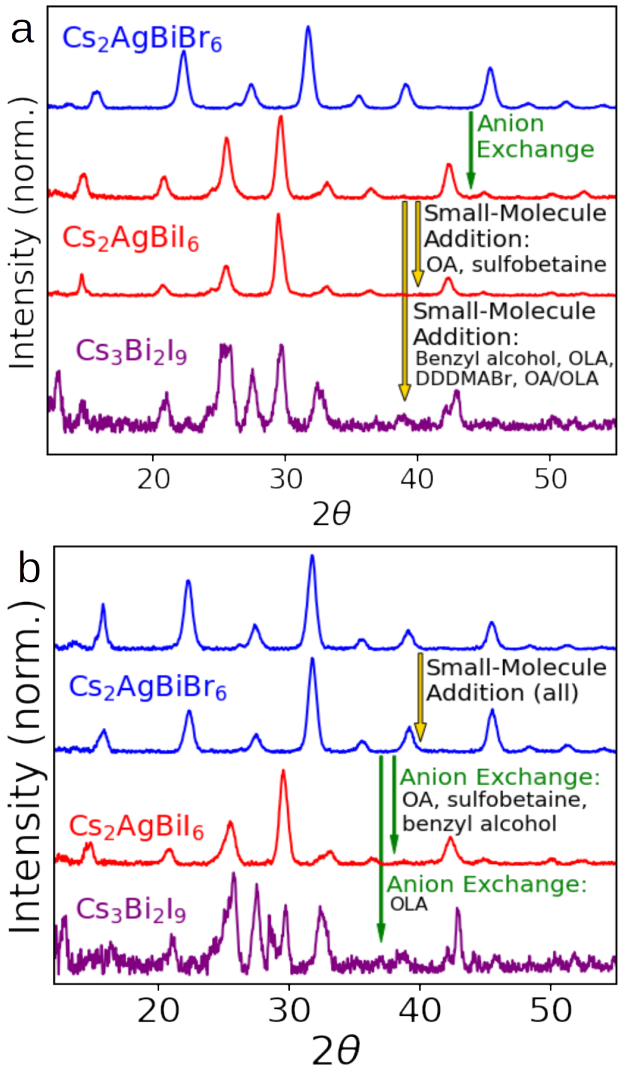

Figure 3.5: Representative XRD data describing the results of anion-exchange and small-molecule addition reactions involving Cs_2AgBiX_6 (X = Br, I) nanocrystals. (a) Anion exchange followed by small-molecule addition. Addition of oleic acid (OA) or sulfobetaine to Cs_2AgBiI_6 nanocrystals retains the elpasolite structure, but addition of oleylamine (OLA), 50:50 (mol) OA:OLA, benzyl alcohol, or didodecyl-dimethylammonium bromide (DDDMABr) transforms the Cs_2AgBiI_6 elpasolite nanocrystals into $Cs_3Bi_2I_9$ nanocrystals. (b) Small-molecule additions followed by anion exchange. $Cs_2AgBiBr_6$ nanocrystals retain the elpasolite structure following additions of all small molecules investigated here. Anion exchange for samples with added OA, sulfobetaine, or benzyl alcohol yields elpasolite Cs_2AgBiI_6 nanocrystals. Anion exchange for samples with added OLA yields $Cs_3Bi_2I_9$ nanocrystals.

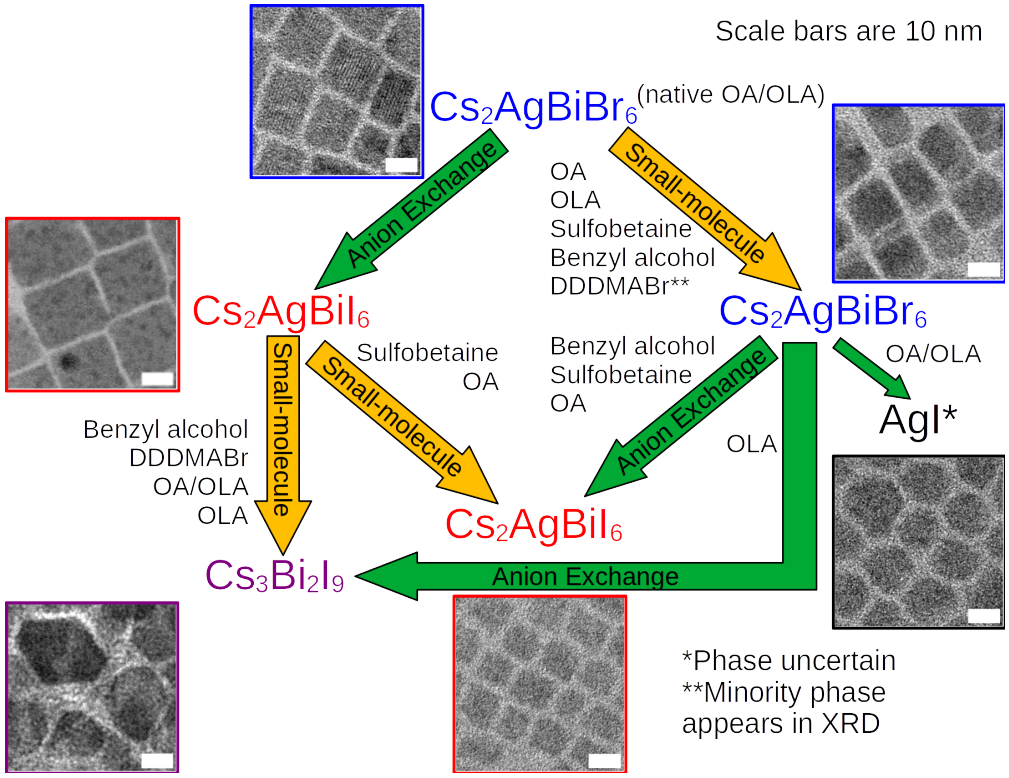

Figure 3.6: Summary of Anion-Exchange and Various Small-Molecule Addition Reactions of Cs_2AgBiX_6 (X = Br, I) Nanocrystals

solite. Additionally, anion exchange in the presence of 50:50 (molar) OA:OLA yielded AgI as the primary product (with evidence of other unidentified minority phases), compared to Cs_2AgBiI_6 when just OA was present.

Scheme 3.6 summarizes the full set of results from these experiments graphically. The arrows denote the reactions that were performed and connect the starting and isolated compositions for each reaction. Small-molecule additives present during each reaction are shown next to the various arrows. This scheme highlights the different susceptibilities of $Cs_2AgBiBr_6$ and Cs_2AgBiI_6 NCs to decomposition. Beginning with the parent $Cs_2AgBiBr_6$ NCs, neither anion exchange nor small-molecule addition causes substantial degradation. From the re-

sulting NCs, however, further chemistry results in a multitude of degradation products. Although $Cs_2AgBiBr_6$ retains its phase upon exposure to the additives examined here, only oleic acid and sulfobetaine preserve the elpasolite structure of Cs_2AgBiI_6. Note the pathway-dependent chemical transformations in the case of benzyl alcohol: its addition to $Cs_2AgBiBr_6$ NCs followed by anion exchange yields Cs_2AgBiI_6 NCs, whereas its addition to Cs_2AgBiI_6 NCs after anion exchange yields a $Cs_3Bi_2I_9$ decomposition product. Additionally, TEM shows the retention of NC size for all reactions, with a morphology change to hexagonal crystals for the hexagonal $Cs_3Bi_2I_9$ decomposition product. We note an apparent correlation between anionic ligands (e.g., oleate and sulfobetaine) and stabilities of Cs_2AgBiI_6 NCs. It is conceivable that the anionic ligands stabilize the iodide elpasolite NCs by passivating surface anion vacancies. Alternatively, although elpasolite decomposition appears to retain the NC size, we cannot neglect the possibility that some of these additives actively drive decomposition through ion-selective microsolvation. Further investigation will be necessary to fully understand the surface chemistry of this new family of nanomaterials. Nonetheless, we conclude from these results that the stability of elpasolite Cs_2AgBiI_6 NCs is indeed highly sensitive to their surface chemistry, and a high surface-to-volume ratio alone is not sufficient to stabilize the elpasolite phase.

In a separate line of interrogation, we then performed a series of experiments aimed at probing the dependence of Cs_2AgBiI_6 stability on temperature and NC size. Thermal stability was probed by both ex situ and in situ measurements. For the ex situ experiments, Cs_2AgBiI_6 NCs were deposited onto Si substrates and their structures were monitored as a function of anaerobic anneal temperature and time using XRD and SEM (Fig. B.18, B.19). The Cs_2AgBiI_6 NCs were stable up to $\sim$100°C, above which they begin to decompose into a mixture of $Cs_3Bi_2I_9$, CsI, and AgI, with $Cs_3Bi_2I_9$ dominating the XRD patterns (Fig. B.18). Full decomposition was observed by 125°C. Moreover, SEM of the $Cs_3Bi_2I_9$ product (Fig. B.19) revealed extensive particle sintering. Heating for 2 h at temperatures below 100°C

caused no decomposition. These results demonstrate that the decomposition of Cs_2AgBiI_6 NCs is thermally activated. Very similar results are obtained from in situ XRD measurements during heating in air (Fig. B.20). We thus hypothesized that this decomposition is linked to the reduced surface-to-volume ratios in the larger crystallites that form, i.e., the reduced influence of surface free energy.

To test this hypothesis, we prepared samples that deliberately contained broad size distributions. For example, Fig. 3.7 shows XRD, TEM, and electron diffraction (ED) data for a sample containing a mixed population of nanocubes (L $\sim$ 15 nm) and nanorods (L $\sim$ 200 nm, W $\sim$ 15 nm). TEM shows that nanorods are the dominant species in this sample, but critically, XRD confirms the presence of only the elpasolite phase (Fig. 3.7a), contrary to the above hypothesis. Electron diffraction (Fig. 3.7c) from the area imaged in Fig. 3.7b shows signature arcs (denoted with red arrows) corresponding to preferential diffraction from the one-dimensional nanorods. These arcs overlay the elpasolite diffraction rings, confirming that these nanorods share the iodide elpasolite structure. There is thus no evidence for a correlation between particle size and phase transformation in this size regime.

We then hypothesized that decomposition may be associated with the combination of heat and particle size. To test this hypothesis, we performed *in situ* heating during TEM measurements of another sample possessing a deliberately broad size distribution (Fig. B.21, B.22). Again, we found no correlation between particle size and decomposition, nor did we generally observe particle sintering upon heating. Some particles transformed and sintered at 100°C while others of the same size persisted as elpasolites even to 120°C (Fig. B.22). Additionally, other NCs decomposed without changing size or sintering with their neighbors. We conclude that phase transformation and particle sintering are *not* linked and instead can occur independently upon heating. Instead, the results suggest that the critical factor in the thermally induced phase transformation of Cs_2AgBiI_6 is likely the loss of surface ligands. In support of this conclusion, we have found that colloidal Cs_2AgBiI_6 NCs retain

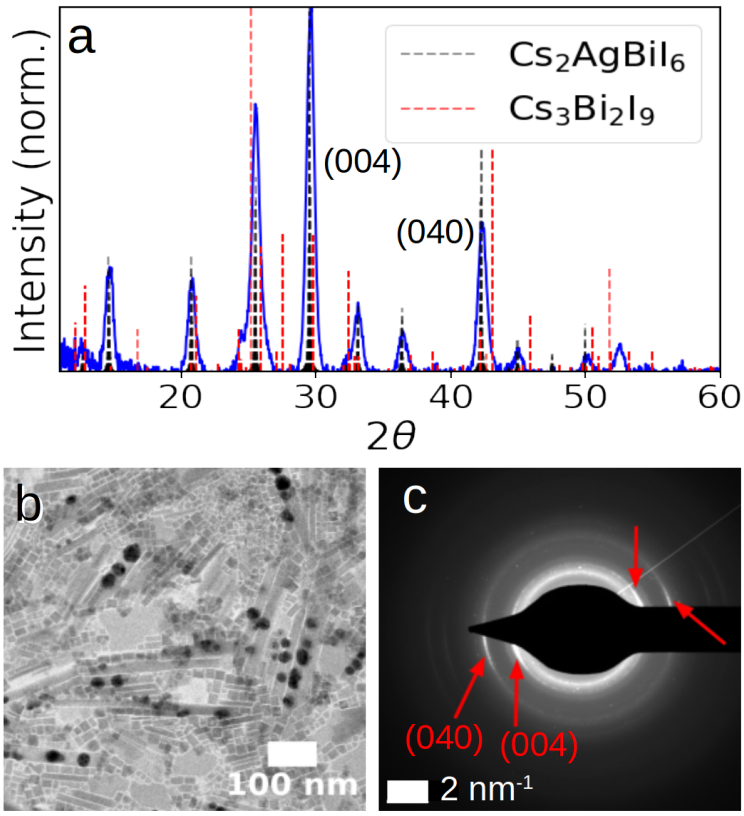

Figure 3.7: (a) XRD, (b) TEM, and (c) electron diffraction (ED) of a Cs_2AgBiI_6 sample with a mixed population of nanocubes and 1D nanorods. The red arrows in (c) identify diffraction arcs corresponding to the nanorods.

the Cs_2AgBiI_6 phase even when heated in solution to 140°C (Fig. B.23), beyond the 100-125°C decomposition temperature of the same NCs on a solid substrate. Collectively, these results provide strong support for the conclusion that surface ligands are a primary factor determining the stability of the Cs_2AgBiI_6 elpasolite phase and preventing its transformation to $Cs_3Bi_2I_9$, and that reduced dimensionality is necessary but not sufficient.

Finally, to test the role of purely kinetic trapping in the formation and stability of this iodide elpasolite, we prepared $Cs_2AgBiBr_6$ polycrystalline thin films (100-200 nm grain sizes, see SI Fig. B.17) by thermal evaporation and attempted to convert these to Cs_2AgBiI_6 by anion exchange, as was done with the NCs. Notably, these grains possess no surface ligands and have much lower surface-to-volume ratios than the colloidal NCs ($\sim$0.04 nm^{-1} vs $\sim$0.40 nm^{-1}), but ion mobility is sufficient for the entire grain volume to remain accessible (see, e.g., refs. 28,48,49 for analogous anion-exchange reactions on lead-halide perovskite films). We previously demonstrated a strong thermodynamic driving force and near-stoichiometric reactivity for TMSX reagents in anion exchange of both perovskites and elpasolites.[8,28] Figure 3.8 presents absorption and XRD data for a representative anion-exchange experiment on one of these thin films. With a single dose (5 molar equivalents) of gas-phase TMSI, the absorption spectrum shows the pronounced low-energy peak decrease in intensity and shift to slightly longer wavelengths, consistent with partial anion exchange. With a second dose of TMSI, this absorption band simply decreases in intensity and the optical quality of the film was observed by eye to degrade, suggesting decomposition. The XRD data in Fig. 3.8b confirm these observations, showing a shift in the elpasolite peak positions with the first dose of TMSI corresponding to anion alloying and formation of $Cs_2AgBi(Br_{0.66}I_{0.34})_6$, but no further movement of the elpasolite peaks is observed upon delivering the second dose of TMSI. Instead, peak broadening is observed, consistent with a decrease in crystallinity. Anion exchange proceeded more slowly in these thin films than in the NCs, and we therefore allowed samples to react for $\sim$24 h to ensure completion after each dose. Additional doses

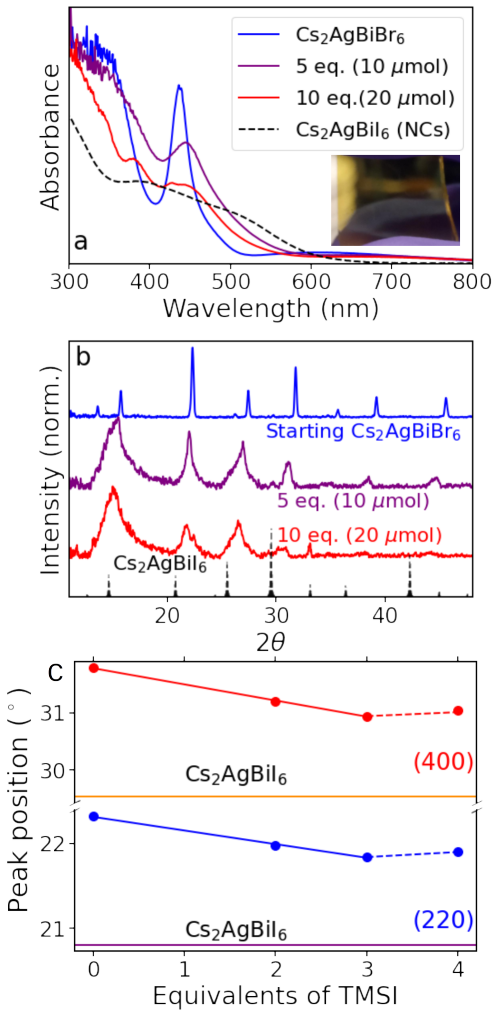

Figure 3.8: (a) Absorption spectra (inset: photograph of starting thin film) and (b) XRD data collected for a thermally evaporated thin film of $Cs_2AgBiBr_6$ at various stages of TMSI addition. A stoichiometric excess of TMSI (10 μmol, similar to the quantities used in the above nanocrystal reactions) was used in both additions and allowed to react for 24 h. Analysis of the XRD peak shifts suggests a terminal composition of $Cs_2AgBi(Br_{0.66}I_{0.34})_6$. (c) Peak positions as a function of equivalents of TMSI. Further anion exchange was not observed beyond 3 equivalents. For reference, the yellow and purple horizontal lines denote the positions of the (400) and (220) peaks in Cs_2AgBiI_6, respectively.

of TMSI or slower dosing with longer reaction times (Fig. 3.8c, S16) both failed to yield any further anion exchange beyond $Cs_2AgBi(Br_{0.66}I_{0.34})_6$. Using an extremely large dose of TMSI (100-fold excess) decomposed the sample to yield a mixture of $Cs_3Bi_2I_9$, AgI, and CsI, with additional minor impurities. Overall these results indicate that the elpasolite structure is stable only up to $Cs_2AgBi(Br_{0.66}I_{0.34})_6$ in these films, and further conversion is not possible. This result provides evidence for rejection of a hypothesis that the iodide elpasolite NCs are achieved solely due to kinetic trapping, and it is consistent with the critical role played by surface free energy in stabilizing the iodide elpasolite phase.

$$2\,Cs_2AgBiI_6 \longrightarrow Cs_3Bi_2I_9 + 2\,AgI + CsI \tag{3.1}$$

One possible balanced chemical reaction describing Cs_2AgBiI_6 decomposition is given by eq. 3.1. The free-energy driving force for this reaction at the nanoscale ($\Delta G_{rxn,NC}$) involves contributions from the lattice (taken as $\Delta G_{rxn,bulk}$), from the change in ligand binding between reactants and products (ΔG_{ligand}), and from any change in intrinsic surface free energies between reactants and products ($\Delta G_{surface}$). The data presented here argue that the magnitude of $\Delta G_{ligand} + \Delta G_{surface}$ must exceed that of $\Delta G_{rxn,bulk}$ for at least some of the ligands examined here. A quantitative analysis of these free energies is complicated by the fact that the thermodynamics of ligand binding to Cs_2AgBiI_6, $Cs_3Bi_2I_9$, AgI, and CsI NCs are not documented. Additionally, decomposition does not generally yield the stoichiometric ratio of crystalline products described by eq. 3.1 (*e.g.*, Scheme 3.6), indicating that additional product species must be accounted for. A full thermodynamic analysis of Cs_2AgBiI_6 NC decomposition will thus require careful experimentation to quantify these many contributing factors.

3.5 Conclusion

The data and analysis presented here provide the first robust structural characterization of any iodide elpasolite. Rietveld refinement of high-energy XRD and PDF data collected from Cs_2AgBiI_6 nanocrystals shows them to exhibit an elpasolite structure with tetragonal (I4-m) symmetry. High-energy XRD and PDF measurements show that the elpasolite structure gradually expands during anion exchange from cubic $Cs_2AgBiBr_6$ to tetragonal Cs_2AgBiI_6 as the lattice accommodates the larger iodide ions. Fitting the PDF data using the refined structure model reveals evidence of surface relaxation, and additional experiments probing the effects of surface ligation and grain size strongly support the conclusion that the elpasolite structure of Cs_2AgBiI_6 is stabilized by the surface free energy of these nanocrystals. The detailed structural characterization presented here, along with the characterization of factors influencing stability of the elpasolite phase, provides a valuable foundation for future exploration and application of this and future members of the extremely rare iodide elpasolite family of compounds. These results further emphasize the unique opportunities that exist for developing this family of compounds when working at the nanoscale.

3.6 Acknowledgements

This research was primarily supported by the UW Molecular Engineering Materials Center, an NSF Materials Research Science and Engineering Center (Grant No. DMR-1719797). Synchrotron X-ray data analysis was supported by the DOE Office of Science, Office of Basic Energy Sciences, Chemical Sciences, Geosciences, and Biosciences Division, Geosciences Program at Pacific Northwest National Laboratory (PNNL) under FWP 56674. PNNL is a multiprogram national laboratory operated for the DOE by Battelle Memorial Institute under Contract DE-AC05-76RL0-1830. Part of this work was conducted at the Molecular Analysis Facility, a National Nanotechnology Coordinated Infrastructure (NNCI) site at the University of Washington, which is supported in part by funds from the National Science

Foundation (awards NNCI-2025489 and NNCI-1542101), the Molecular Engineering & Sciences Institute, and the Clean Energy Institute. We acknowledge Scott Braswell for his assistance with SEM & EDX measurements. TEM heating data using an in situ heating holder were collected in the William R. Wiley Environmental Molecular Sciences Laboratory (EMSL), a national scientific user facility sponsored by DOE's Office of Biological and Environmental Research and located at Pacific Northwest National Laboratory. We thank Libor Kovarik for his assistance with these experiments. This research used resources of the Advanced Photon Source, a U.S. Department of Energy (DOE) Office of Science User Facility operated for the DOE Office of Science by Argonne National Laboratory under Contract No. DE-AC02-06CH11357. The authors thank Leighanne Gallington and Olaf Borkiewicz from Sector 11 (BL 11-ID-B) for assistance collecting data presented in this manuscript.

3.7 References

(1) Pan, Y.; Zhang, Y.; Kang, W.; Deng, N.; Yan, Z.; Sun, W.; Kang, X.; Ni, J. Progress in the preparation and application of CsPbX3 perovskites. Materials Advances 2022, 3 (10), 4053-4068. DOI: 10.1039/D2MA00100D.

(2) Ling, X.; Yuan, J.; Ma, W. The Rise of Colloidal Lead Halide Perovskite Quantum Dot Solar Cells. Accounts of Materials Research 2022, 3 (8), 866-878. DOI: 10.1021/accountsmr.2c00081.

(3) Nair, S. S.; Krishnia, L.; Trukhanov, A.; Thakur, P.; Thakur, A. Prospect of double perovskite over conventional perovskite in photovoltaic applications. Ceramics International 2022, 48 (23), 34128-34147. DOI: 10.1016/j.ceramint.2022.08.184.

(4) Savory, C. N.; Walsh, A.; Scanlon, D. O. Can Pb-Free Halide Double Perovskites Support High-Efficiency Solar Cells? ACS Energy Letters 2016, 1 (5), 949-955. DOI: 10.1021/acsenergylett.6b00471.

(5) Bartesaghi, D.; Slavney, A. H.; Gélvez-Rueda, M. C.; Connor, B. A.; Grozema, F.

C.; Karunadasa, H. I.; Savenije, T. J. Charge Carrier Dynamics in $Cs_2AgBiBr_6$ Double Perovskite. The Journal of Physical Chemistry C 2018, 122 (9), 4809-4816. DOI: 10.1021/acs.jpcc.8b00572.

(6) Chen, X.; Jia, M.; Xu, W.; Pan, G.; Zhu, J.; Tian, Y.; Wu, D.; Li, X.; Shi, Z. Recent Progress and Challenges of Bismuth-Based Halide Perovskites for Emerging Optoelectronic Applications. Advanced Optical Materials 2023, 11 (3), 2202153. DOI: 10.1002/adom.202202153.

(7) Ghosh, S.; Shankar, H.; Kar, P. Recent developments of lead-free halide double perovskites: a new superstar in the optoelectronic field. Materials Advances 2022, 3 (9), 3742-3765. DOI: 10.1039/D2MA00071G.

(8) Creutz, S. E.; Crites, E. N.; De Siena, M. C.; Gamelin, D. R. Colloidal Nanocrystals of Lead-Free Double-Perovskite (Elpasolite) Semiconductors: Synthesis and Anion Exchange To Access New Materials. Nano Letters 2018, 18 (2), 1118-1123. DOI: 10.1021/acs.nanolett.7b04659.

(9) Sk, M. Recent progress of lead-free halide double perovskites for green energy and other applications. Applied Physics A 2022, 128 (5), 462. DOI: 10.1007/s00339-022-05596-9.

(10) Bello, O. O.; Emetere, M. E. Progress and limitation of lead-free inorganic perovskites for solar cell application. Solar Energy 2022, 243, 370-380. DOI: https://doi.org/10.1016/j.solener.2022.08.018.

(11) Vishnoi, P.; Seshadri, R.; Cheetham, A. K. Why are Double Perovskite Iodides so Rare? The Journal of Physical Chemistry C 2021, 125 (21), 11756-11764. DOI: 10.1021/acs.jpcc.1c02870.

(12) Zhang, T.; Cai, Z.; Chen, S. Chemical Trends in the Thermodynamic Stability and Band Gaps of 980 Halide Double Perovskites: A High-Throughput First-Principles Study. ACS Applied Materials & Interfaces 2020, 12 (18), 20680-20690. DOI: 10.1021/acsami.0c03622.

(13) Rajeev Kumar, N.; Radhakrishnan, R. Electronic, optical and mechanical properties of lead-free halide double perovskites using first-principles density functional theory. Materials Letters 2018, 227, 289-291. DOI: 10.1016/j.matlet.2018.05.082.

(14) Tripathi, M. N.; Saha, A.; Singh, S. Structural, elastic, electronic and optical properties of lead-free halide double perovskite Cs_2AgBiX_6 (X = Cl, Br, and I). Materials Research Express 2019, 6 (11), 115517-115517. DOI: 10.1088/2053-1591/ab48ba.

(15) Zarabinia, N.; Rasuli, R. Electronic and optical properties of halide double-perovskites under strain: a density functional study. Energy Sources, Part A: Recovery, Utilization, and Environmental Effects 2021, 43 (20), 2443-2455. DOI: 10.1080/15567036.2020.1867672.

(16) Anbarasan, R.; Srinivasan, M.; Suriakarthick, R.; Albalawi, H.; Sundar, J. K.; Ramasamy, P.; Mahmood, Q. Exploring the structural, mechanical, electronic, and optical properties of double perovskites of Cs2AgInX6 (X = Cl, Br, I) by first-principles calculations. Journal of Solid State Chemistry 2022, 310, 123025. DOI: 10.1016/j.jssc.2022.123025.

(17) Volonakis, G.; Filip, M. R.; Haghighirad, A. A.; Sakai, N.; Wenger, B.; Snaith, H. J.; Giustino, F. Lead-Free Halide Double Perovskites via Heterovalent Substitution of Noble Metals. The Journal of Physical Chemistry Letters 2016, 7 (7), 1254-1259. DOI: 10.1021/acs.jpclett.6b00376.

(18) Filip, M. R.; Liu, X.; Miglio, A.; Hautier, G.; Giustino, F. Phase Diagrams and Stability of Lead-Free Halide Double Perovskites Cs2BB'X6: B = Sb and Bi, B' = Cu, Ag, and Au, and X = Cl, Br, and I. The Journal of Physical Chemistry C 2018, 122 (1), 158-170. DOI: 10.1021/acs.jpcc.7b10370.

(19) Creutz, S. E.; Liu, H.; E. Kaiser, M.; Li, X.; R. Gamelin, D. Structural Diversity in Cesium Bismuth Halide Nanocrystals. Chemistry of Materials 2019, 31 (13), 4685-4697. DOI: 10.1021/acs.chemmater.9b00640.

(20) Sansom, H. C.; Longo, G.; Wright, A. D.; Buizza, L. R. V.; Mahesh, S.; Wenger, B.; Zanella, M.; Abdi-Jalebi, M.; Pitcher, M. J.; Dyer, M. S.; et al. Highly Absorbing Lead-Free Semiconductor Cu_2AgBiI_6 for Photovoltaic Applications from the Quaternary CuI–AgI–BiI3 Phase Space. Journal of the American Chemical Society 2021, 143 (10), 3983-3992. DOI: 10.1021/jacs.1c00495.

(21) Glodo, J.; van Loef, E. V. D.; Higgins, W. M.; Shah, K. S. Scintillation Properties of Cs2NaLaI6:Ce. 2006, IEEE: Vol. 02472, pp 1208-1211. DOI: 10.1109/NSSMIC.2006.356061.

(22) Gundiah, G.; Brennan, K.; Yan, Z.; Samulon, E. C.; Wu, G.; Bizarri, G. A.; Derenzo,

S. E.; Bourret-Courchesne, E. D. Structure and scintillation properties of Ce3+-activated Cs2NaLaCl6, Cs3LaCl6, Cs2NaLaBr6, Cs3LaBr6, Cs2NaLaI6 and Cs3LaI6. Journal of Luminescence 2014, 149, 374-384. DOI: 10.1016/j.jlumin.2013.09.057.

(23) Zhang, C.; Gao, L.; Teo, S.; Guo, Z.; Xu, Z.; Zhao, S.; Ma, T. Design of a novel and highly stable lead-free Cs_2NaBiI_6 double perovskite for photovoltaic application. Sustainable Energy and Fuels 2018, 2 (11), 2419-2428. DOI: 10.1039/c8se00154e.

(24) Zheng, Y.; Luo, F.; Ruan, L.; Tong, J.; Yan, L.; Sun, C.; Zhang, X. A facile fabrication of lead-free Cs_2NaBiI_6 double perovskite films for memory device application. Journal of Alloys and Compounds 2022, 909, 164613-164613. DOI: 10.1016/j.jallcom.2022.164613.

(25) Bhorde, A.; Waykar, R.; Rondiya, S. R.; Nair, S.; Lonkar, G.; Funde, A.; Dzade, N. Y.; Jadkar, S. Structural, Electronic, and Optical Properties of Lead-Free Halide Double Perovskite Rb_2AgBiI_6: A Combined Experimental and DFT Study. ES Materials & Manufacturing 2021, 12, 43-52. DOI: 10.30919/esmm5f1042.

(26) Shadabroo, M. S.; Abdizadeh, H.; Golobostanfard, M. R. Elpasolite structures based on A2AgBiX6 (A: MA, Cs, X: I, Br): Application in double perovskite solar cells. Materials Science in Semiconductor Processing 2021, 125, 105639-105639. DOI: 10.1016/j.mssp.2020.105639.

(27) Pai, N.; Chatti, M.; Fürer, S. O.; Scully, A. D.; Raga, S. R.; Rai, N.; Tan, B.; Chesman, A. S. R.; Xu, Z.; Rietwyk, K. J.; et al. Solution Processable Direct Bandgap Copper-Silver-Bismuth Iodide Photovoltaics: Compositional Control of Dimensionality and Optoelectronic Properties. Advanced Energy Materials 2022, 12 (32), 2201482. DOI: 10.1002/aenm.202201482.

(28) Creutz, S. E.; Crites, E. N.; De Siena, M. C.; Gamelin, D. R. Anion Exchange in Cesium Lead Halide Perovskite Nanocrystals and Thin Films Using Trimethylsilyl Halide Reagents. Chemistry of Materials 2018, 30 (15), 4887-4891. DOI: 10.1021/acs.chemmater.8b02100.

(29) Kroupa, D.; Crane, M.; Gamelin, D. Single-source flash sublimation of metal-halide semiconductors; SPIE, 2019. DOI: 10.1117/12.2528622.

(30) Hoeher, A.; Mergelsberg, S.; Borkiewicz, O. J.; Dove, P. M.; Michel, F. M. A new

method for in situ structural investigations of nano-sized amorphous and crystalline materials using mixed-flow reactors. Acta Crystallographica Section A 2019, 75 (5), 758-765. DOI: doi:10.1107/S2053273319008623.

(31) Toby, B. H.; Von Dreele, R. B. GSAS-II: the genesis of a modern open-source all purpose crystallography software package. Journal of Applied Crystallography 2013, 46 (2), 544-549. DOI: 10.1107/S0021889813003531.

(32) Juhás, P.; Davis, T.; Farrow, C. L.; Billinge, S. J. L. PDFgetX3 : a rapid and highly automatable program for processing powder diffraction data into total scattering pair distribution functions. Journal of Applied Crystallography 2013, 46 (2), 560-566. DOI: 10.1107/S0021889813005190.

(33) Farrow, C. L.; Juhas, P.; Liu, J. W.; Bryndin, D.; Božin, E. S.; Bloch, J.; Proffen, T.; Billinge, S. J. L. PDFfit2 and PDFgui: computer programs for studying nanostructure in crystals. Journal of Physics: Condensed Matter 2007, 19 (33), 335219-335219. DOI: 10.1088/0953-8984/19/33/335219.

(34) Filip, M. R.; Hillman, S.; Haghighirad, A. A.; Snaith, H. J.; Giustino, F. Band Gaps of the Lead-Free Halide Double Perovskites Cs2BiAgCl6 and Cs2BiAgBr6 from Theory and Experiment. The Journal of Physical Chemistry Letters 2016, 7 (13), 2579-2585. DOI: 10.1021/acs.jpclett.6b01041.

(35) Billinge, S. J. L.; Kanatzidis, M. G. Beyond crystallography: the study of disorder, nanocrystallinity and crystallographically challenged materials with pair distribution functions. Chemical Communications 2004, (7), 749-749. DOI: 10.1039/b309577k.

(36) Egami, T.; Billinge, S. J. L. Underneath the Bragg peaks : structural analysis of complex materials; Pergamon, 2012.

(37) Billinge, S. J. L.; Levin, I. The problem with determining atomic structure at the nanoscale. Science 2007, 316 (5824), 561-565. DOI: 10.1126/science.1135080.

(38) Li, M.; Zhang, X.; Lu, S.; Yang, P. Phase transformation, morphology control, and

luminescence evolution of cesium lead halide nanocrystals in the anion exchange process. RSC Advances 2016, 6 (105), 103382-103389. DOI: 10.1039/C6RA22070C.

(39) Nedelcu, G.; Protesescu, L.; Yakunin, S.; Bodnarchuk, M. I.; Grotevent, M. J.; Kovalenko, M. V. Fast Anion-Exchange in Highly Luminescent Nanocrystals of Cesium Lead Halide Perovskites (CsPbX3 , X = Cl, Br, I). Nano Letters 2015, 15 (8), 5635-5640. DOI: 10.1021/acs.nanolett.5b02404.

(40) Fu, Y.; Wu, T.; Wang, J.; Zhai, J.; Shearer, M. J.; Zhao, Y.; Hamers, R. J.; Kan, E.; Deng, K.; Zhu, X. Y.; et al. Stabilization of the Metastable Lead Iodide Perovskite Phase via Surface Functionalization. Nano Lett 2017, 17 (7), 4405-4414. DOI: 10.1021/acs.nanolett.7b01500.

(41) Tappan, B. A.; Brutchey, R. L. Polymorphic Metastability in Colloidal Semiconductor Nanocrystals. ChemNanoMat 2020, 6 (11), 1567-1588. DOI: 10.1002/cnma.202000406.

(42) Soni, U.; Arora, V.; Sapra, S. Wurtzite or zinc blende? Surface decides the crystal structure of nanocrystals. CrystEngComm 2013, 15 (27), 5458-5463. DOI: 10.1039/c3ce40267c.

(43) Mahler, B.; Lequeux, N.; Dubertret, B. Ligand-Controlled Polytypism of Thick-Shell CdSe/CdS Nanocrystals. Journal of the American Chemical Society 2010, 132 (3), 953-959. DOI: 10.1021/ja9034973.

(44) Krieg, F.; Ochsenbein, S. T.; Yakunin, S.; ten Brinck, S.; Aellen, P.; Süess, A.; Clerc, B.; Guggisberg, D.; Nazarenko, O.; Shynkarenko, Y.; et al. Colloidal CsPbX3 (X = Cl, Br, I) Nanocrystals 2.0: Zwitterionic Capping Ligands for Improved Durability and Stability. ACS Energy Letters 2018, 3 (3), 641-646. DOI: 10.1021/acsenergylett.8b00035.

(45) Stelmakh, A.; Aebli, M.; Baumketner, A.; Kovalenko, M. V. On the Mechanism of Alkylammonium Ligands Binding to the Surface of $CsPbBr_3$ Nanocrystals. Chemistry of Materials 2021, 33 (15), 5962-5973. DOI: 10.1021/acs.chemmater.1c01081.

(46) Veldhuis, S. A.; Tay, Y. K. E.; Bruno, A.; Dintakurti, S. S. H.; Bhaumik, S.; Muduli, S. K.; Li, M.; Mathews, N.; Sum, T. C.; Mhaisalkar, S. G. Benzyl Alcohol-Treated CH3NH3PbBr3 Nanocrystals Exhibiting High Luminescence, Stability, and Ultralow Amplified Spontaneous

Emission Thresholds. Nano Letters 2017, 17 (12), 7424-7432. DOI: 10.1021/acs.nanolett.7b03272.

(47) Sun, J.-K. K.; Huang, S.; Liu, X.-z. Z.; Xu, Q.; Zhang, Q.-H. H.; Jiang, W.-J. J.; Fang, X. X.-h. X. H. X.-h.; Zhong, H.-Z. Z.; Hu, J.-S. S.; Wan, L.-J. J.; et al. Polar Solvent Induced Lattice Distortion of Cubic CsPbI3 Nanocubes and Hierarchical Self-Assembly into Orthorhombic Single-Crystalline Nanowires. Journal of the American Chemical Society 2018, 140 (37), 11705-11715. DOI: 10.1021/jacs.8b05949.

(48) Li, G.; Ho, J. Y.-L.; Wong, M.; Kwok, H. S. Reversible Anion Exchange Reaction in Solid Halide Perovskites and Its Implication in Photovoltaics. The Journal of Physical Chemistry C 2015, 119 (48), 26883-26888. DOI: 10.1021/acs.jpcc.5b09300.

(49) Hoffman, J. B.; Schleper, A. L.; Kamat, P. V. Transformation of Sintered $CsPbBr_3$ Nanocrystals to Cubic CsPbI3 and Gradient CsPbBrxI3–x through Halide Exchange. Journal of the American Chemical Society 2016, 138 (27), 8603-8611. DOI: 10.1021/jacs.6b04661.

Chapter 4

PROBING YB^{3+} STRUCTURE IN CRX_3:YB^{3+} (X = CL, BR, I) USING EXAFS

4.1 Introduction

The chromium trihalides, particularly CrI_3, have recently emerged as interesting 2D magnetic materials, displaying magnetic ordering even down to the single monolayer.[1,2] Our group recently demonstrated Yb^{3+}-doping of bulk CrI_3.[3] Remarkably, we observed that Yb^{3+} PL can be controlled by controlling CrI_3 magnetism, attributed to the effects of strong in-plane Yb^{3+}-Cr^{3+} superexchange coupling. Yb^{3+} is believed to be a substitutional point defect in these materials based on single-crystal x-ray diffraction studies of ∼5% Yb^{3+}-doped CrI_3, but the exact location of the Yb^{3+} sites remains unknown. Identifying the structure of this point defect will enable improved understanding of structure-property relationships in this material and will facilitate analysis of the electronic and magnetic structures of Yb^{3+}-doped CrX_3 materials. Herein, we report the use of EXAFS spectroscopy for the study of Yb^{3+} and Cr^{3+} sites in CrX_3:Yb^{3+} (X = Cl, Br, I), and show Yb^{3+} to be exclusively substituting at Cr^{3+} sites. Relative to Cr^{3+} in CrI_3, Yb^{3+} in CrI_3 shows local bond distances that are elongated by ∼0.3 Å.

4.2 Methods

4.2.1 XAS measurements

X-ray absorption near edge structure (XANES) and extended x-ray absorption fine structure (EXAFS) spectra were collected at beamline 20-BM at the Advanced Photon Source at

Argonne National Laboratory. Yb L_3 edge (8944 eV) and Cr K edge (5989 eV) data were collected in fluorescence mode for single crystals of each sample at room temperature under helium atmosphere with active purging. Samples were sealed in Kapton tape under inert atmosphere to prevent air exposure prior to loading in the beamline holder. A Si(111) double-crystal monochromator was used to select the incident energy with He/N_2-filled ion chambers to monitor the flux. The monochromator was calibrated using Cr foil. The pre-edge region was collected from 150 to 20 eV below the edge with a step size of 10 eV and a collection time of 0.4 s at each step. From 20 eV below the edge to 30 eV above the edge, data were collected in 0.5 eV steps for 0.4 s at each step. Post-edge data were collected to 9.6 keV (for Yb) or 7 keV (for Cr) and obtained with a 0.05 keV step size and a collection time of 0.4 s per step. Data normalization and energy calibration were performed using ATHENA software.[4] Data were normalized to low energy region of interest.

4.2.2 XAS data analysis

EXAFS equation fits to the Fourier-transformed data in R-space for each sample were performed with ARTEMIS software, with fit parameters for amplitude, energy (wavenumber) alignment, path half-lengths, and Debye-Waller factors.[4] Theoretical scattering paths for each proposed structure were calculated using FEFF6[5-7] via the ARTEMIS software.[4] A window from 3 to 12 $Å^{-1}$ with a dk value of 1 $Å^{-1}$ and an R-space range from 1 to 3 Å was used for shell-by-shell fitting. This fully encompasses all the features observed in our data. R-space EXAFS data were then corrected in Artemis using a halide (Cl, Br, or I) single scattering path taken from the CrX_3 host lattice structure at the same temperature. For the sake of clarity, we use R + ΔR to denote the corrected radial distance axis in the EXAFS data.

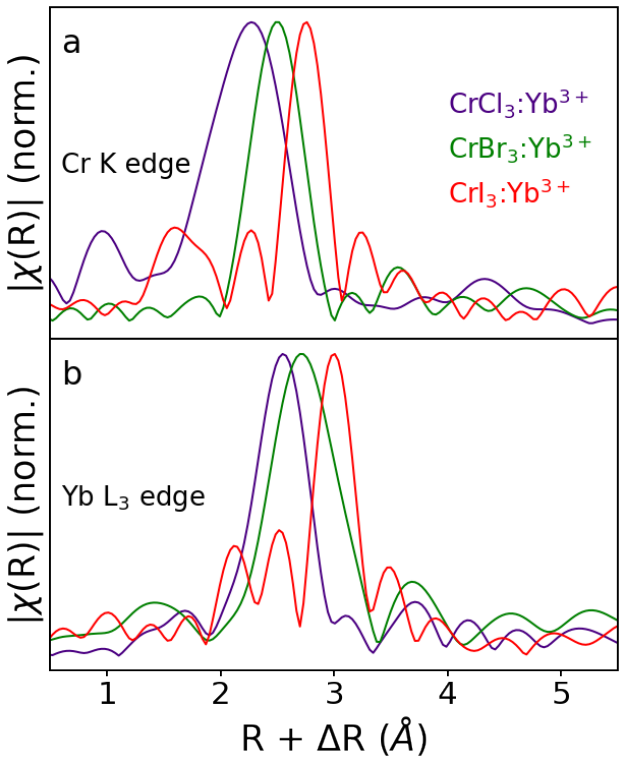

Figure 4.1: Cr K edge (a) and Yb L_3 edge (b) Fourier transform (real space) EXAFS spectra for CrX_3:Yb^{3+} (X = Cl, Br, I) samples. Data are phase-corrected using respective primary halide scattering paths from fits and normalized for straightforward comparison of peak shapes and positions. Smaller features in data are consistent with their respective calculated single-scattering paths.

4.3 Results

Figure 4.1 shows Cr K edge and Yb L_3 edge EXAFS data for CrX_3:Yb^{3+} (X = Cl, Br, I) samples, plotted as Fourier-transform (real-space) spectra. Both edges were measured for each sample at room temperature, and the data were phase-corrected with their respective single scattering paths. A single dominant peak is clear in each spectrum, with a consistent

peak shape across samples, and no other major peaks observed. The position of the peak increases moving down the halide series from the chloride lattice to the iodide lattice. For each sample, the peak in the Yb L_3 edge data exhibits a very similar peak shape to the peak in the Cr K edge data, but is shifted to higher R-values, indicating a greater Yb-X bond distance. For both edges, the CrI_3:Yb^{3+} data show a greater number of minority features. A fitting analysis found these to be attributable to the iodide single scattering path behavior.

Figure 4.2 compares the experimental R-space EXAFS data (a) from the Yb L_3 edge in $CrCl_3$:Yb^{3+} with calculated scattering paths for Yb L_3 edges in three different hypothesized Yb^{3+} sites: (b) substitutional Yb^{3+} in a Cr^{3+} site, (c) Yb^{3+} dopant in an empty 'pocket' site between Cr^{3+} sites, and two potential interlayer sites in the $CrCl_3$ C2-m layered structure at room temperature: (d) Yb^{3+} in line with Cr^{3+} columns, and (e) Yb^{3+} in line with the pocket spaces between Cr^{3+} sites. Each of these is a simple structure model (insets) based on reported structural data, with no geometry optimization. The C2-m layered structure was chosen because it is consistent across all three compositions at room temperature. Detailed views of the interlayer site structures are shown in Figure 4.3. The interlayer sites exhibit several scattering peaks that are not observed in the data, and initial fits using these structures yielded very poor results. In contrast, the scattering path from the Cr^{3+} site closely resembles the experimental data, and this path yields an excellent fit with no anomalous fit parameters and an R-factor of 0.017. These data provide strong evidence indicating that Yb^{3+} almost exclusively occupies Cr^{3+} sites in the CrX_3 lattice. The data show no evidence of any other Yb^{3+} speciation.

Figure 4.4 shows fit results for EXAFS equation fits to the Cr K edge (top row) and Yb L_3 edge (bottom row) data for each sample, using the respective nearest-neighbor halide scattering paths. Fits are shown on top of the data in black dashed lines. A very close visual match between the fit and the single feature in the data can be seen for each sample. For all six spectra, the features are well fit using just the single-scattering paths of

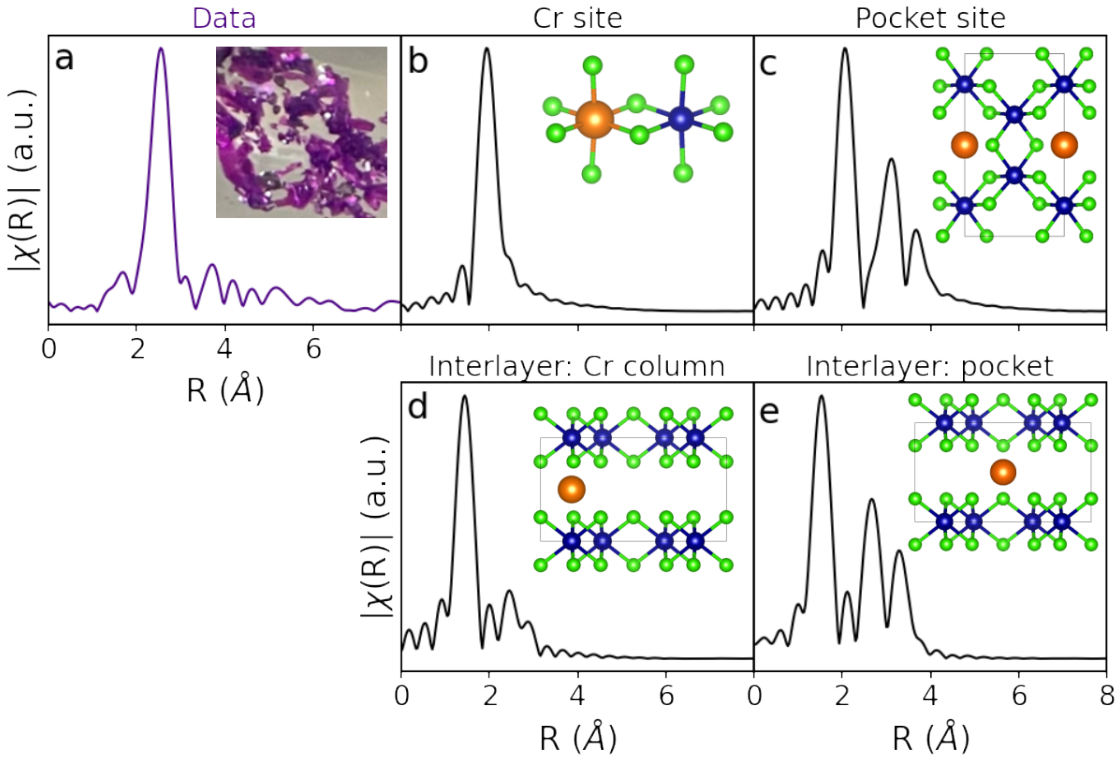

Figure 4.2: R-space EXAFS for Yb in various sites. (a) Experimental data for Yb L_3 edge in $CrCl_3$:Yb^{3+}. (b-d) Calculated scattering paths for five hypothesized Yb^{3+} sites: (b) Yb^{3+} at a Cr^{3+} site; (c) Yb^{3+} in an empty 'pocket' site between Cr^{3+} sites; an interlayer Yb^{3+} in the $CrCl_3$ layered structure in line with (d) Cr^{3+} column and (e) pocket spaces between Cr^{3+}. Single scattering paths for the nearest-neighbor scatterers were calculated using FEFF. Inset for (a) shows a photograph of $CrCl_3$:Yb^{3+} crystals; insets for (b-e) show structure models of hypothesized Yb^{3+} (orange) locations in the $CrCl_3$ lattice (Cr: blue; Cl: green).

nearest-neighbor halide ions. No other scattering paths were needed. These results indicate a (pseudo)octahedral coordination environment around the scattering ion. The smaller features in each spectrum, particularly evident in the spectra of CrI_3:Yb^{3+}, are also consistent with the calculated spectra using single scattering paths. Table 4.1 summarizes the fitting

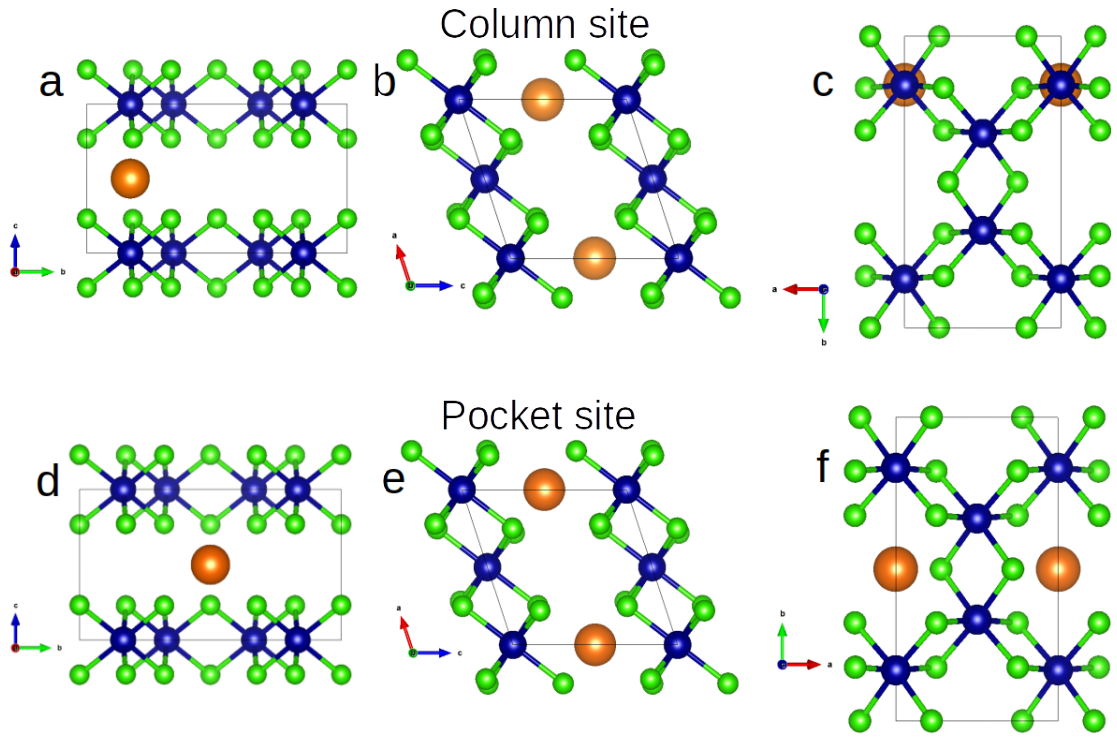

Figure 4.3: Detailed view of interlayer Yb^{3+} sites in $CrCl_3$ C2-m structure. (a-c) show Yb in-line with Cr columns, viewed along the a (a), b (b), and c (c) crystallographic axes. (d-f) show Yb in-line with 'pocket' spaces between Cr sites in the $CrCl_3$ layers, viewed along the a (d), b (e), and c (f) crystallographic axes.

parameters and bond distances obtained from this analysis. These results show systematically increasing Cr-X and Yb-X bond distances moving down the periodic table. In each compound, the Yb-X bonds are longer than the Cr-X bonds. These trends are consistent with the trend in halide ionic radius and, in the case of Cr^{3+}, with XRD data for the parent CrX_3 compounds. Notably, the Yb-X bond distances found here agree very well with those found in other lattices (*e.g.*, Yb^{3+}-doped $CsPbCl_3$).[8-10] Overall, the goodness of these fits when using an identical coordination environment for both Cr^{3+} and Yb^{3+} provides strong

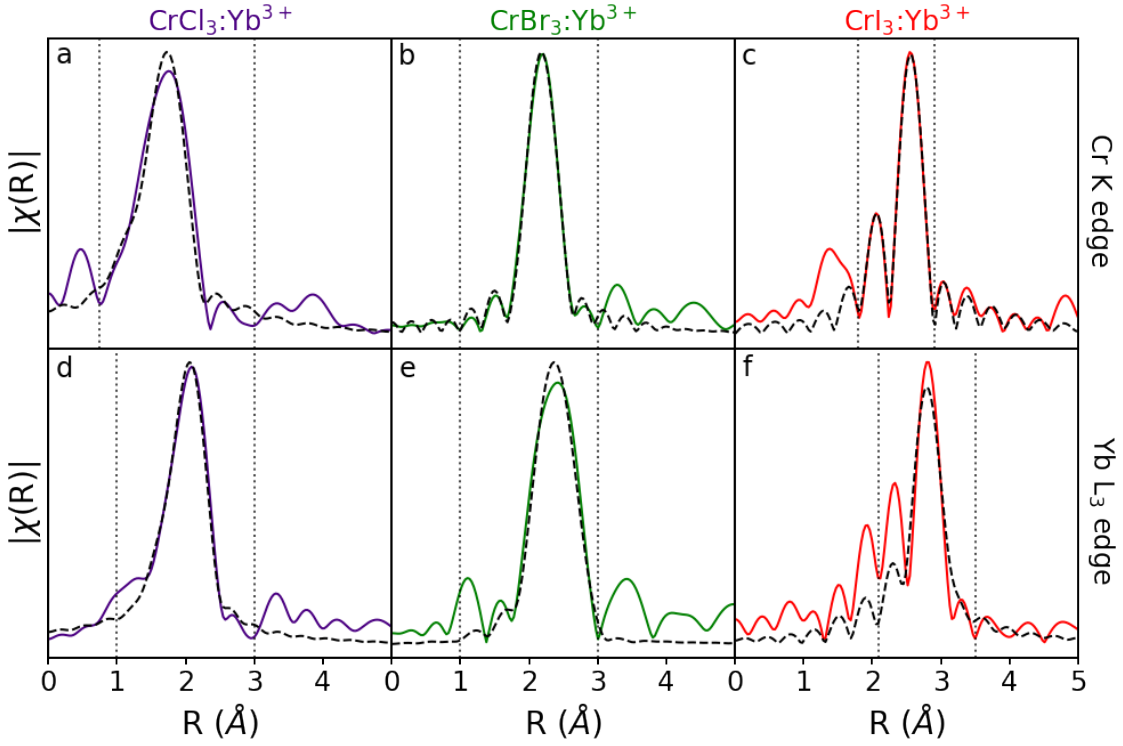

Figure 4.4: Fourier-transform (real-space) EXAFS data and fits (black dashed lines) using the nearest-neighbor halide scatterers for the Cr K edge (top row) and Yb L_3 edge (bottom row) for each sample. (a,d) $CrCl_3$:Yb^{3+} data (purple); (b,e) $CrBr_3$:Yb^{3+} data (green); (c,f) CrI_3:Yb^{3+} data (red). Vertical dotted lines in each panel mark the fitting windows used, in R-space. Note the radial distances have not been corrected for phase shift, in order to compare with the fits.

evidence for substitution of Yb^{3+} at Cr^{3+} sites, and an increase in Yb-X bond distances relative to Cr-X.

Table 4.1: Fitting parameters and bond distances for optimized shell-by-shell fits of EXAFS data for CrX_3:Yb^{3+} (X = Cl, Br, I) single-crystal samples.

	R-factor	χ^2	χ^2_{red}	Debye-Waller	Bond Distance (Å)
Cr K edge					
$CrCl_3$:Yb^{3+}	0.016	1380	239	0.0113	2.252 ±0.015
$CrBr_3$:Yb^{3+}	0.001	69	7	0.0033	2.494 ±0.002
CrI_3:Yb^{3+}	0.008	39	18	0.0036	2.715 ±0.006
Yb L_3 edge					
$CrCl_3$:Yb^{3+}	0.017	624	88	0.0108	2.541 ±0.013
$CrBr_3$:Yb^{3+}	0.012	42	11	0.0068	2.806 ±0.019
CrI_3:Yb^{3+}	0.007	16	4	0.0040	2.945 ±0.005

4.4 Acknowledgements

This research was primarily supported by the UW Molecular Engineering Materials Center, an NSF Materials Research Science and Engineering Center (Grant No. DMR-1719797). This research used resources of the Advanced Photon Source, a U.S. Department of Energy (DOE) Office of Science User Facility operated for the DOE Office of Science by Argonne National Laboratory under Contract No. DE-AC02-06CH11357. We acknowledge Steve Heald and Shelly Kelly from APS Sector 20 (BL 20-BM) (GUP 77348) for collecting these data sets and assistance with data processing. We also thank Sebastian Mergelsberg, Micah Prange, and Sarah Saslow for assistance with EXAFS theory and analysis.

4.5 References

(1) De Siena, M. C.; Creutz, S. E.; Regan, A.; Malinowski, P.; Jiang, Q.; Kluherz, K. T.; Zhu, G.; Lin, Z.; De Yoreo, J. J.; Xu, X.; et al. Two-Dimensional van der Waals Nanoplatelets

with Robust Ferromagnetism. Nano Letters 2020, 20 (3), 2100-2106.

(2) Niu, B.; Su, T.; A. Francisco, B.; Ghosh, S.; Kargar, F.; Huang, X.; Lohmann, M.; Li, J.; Xu, Y.; Taniguchi, T.; et al. Coexistence of Magnetic Orders in Two-Dimensional Magnet CrI_3. Nano Letters 2019, 20 (1), 553-558.

(3) Pressler, K.; Snoeren, T. J.; Walsh, K. M.; Gamelin, D. R. Magnetic Amplification at Yb^{3+} "Designer Defects" in the van der Waals Ferromagnet CrI3. Nano Letters 2023, 23, 1320-1326.

(4) Ravel, B.; Newville, M. ATHENA, ARTEMIS, HEPHAESTUS: Data analysis for X-ray absorption spectroscopy using IFEFFIT. Journal of Synchrotron Radiation 2005, 12 (4), 537-541.

(5) Rehr, J. J.; Albers, R. C. Theoretical approaches to x-ray absorption fine structure. Reviews of Modern Physics 2000, 72 (3), 621-654.

(6) Rehr, J. J.; Kas, J. J.; Prange, M. P.; Sorini, A. P.; Takimoto, Y.; Vila, F. Ab initio theory and calculations of X-ray spectra. Comptes Rendus Physique 2009, 10 (6), 548-559.

(7) Rehr, J. J.; Kas, J. J.; Vila, F. D.; Prange, M. P.; Jorissen, K. Parameter-free calculations of X-ray spectra with FEFF9. Physical Chemistry Chemical Physics 2010, 12 (21), 5503-5513.

(8) Kluherz, K. T.; Mergelsberg, S. T.; Sommer, D. E.; Roh, J. Y. D.; Saslow, S. A.; Biner, D.; Krämer, K. W.; Dunham, S. T.; De Yoreo, J. J.; Gamelin, D. R. Defect structure in quantum-cutting Yb^{3+}-doped $CsPbCl_3$ perovskites probed by x-ray absorption and atomic pair distribution function analysis. Physical Review Materials 2022, 6 (7), 074601-074601.

(9) Sommer, D. E.; Gamelin, D. R.; Dunham, S. T. Defect formation in Yb-doped $CsPbCl_3$ from first principles with implications for quantum cutting. Physical Review Materials 2022, 6 (2), 025404-025404.

(10) Atanasov, M.; Daul, C.; Güdel, H. U.; Wesolowski, T. A.; Zbiri, M. Ground States, Excited States, and Metal-Ligand Bonding in Rare Earth Hexachloro Complexes: A DFT-

Based Ligand Field Study. Inorganic Chemistry 2005, 44 (8), 2954-2963.

Appendix A

SUPPLEMENTAL MATERIAL FOR: DEFECT STRUCTURE IN QUANTUM-CUTTING YB^{3+}-DOPED $CSPBCL_3$ PEROVSKITES PROBED BY X-RAY ABSORPTION AND ATOMIC PAIR DISTRIBUTION FUNCTION ANALYSIS

Reproduced with permission from:

Kluherz, K. T.; Mergelsberg, S. T.; Sommer, D. E.; Roh, J. Y. D.; Saslow, S. A.; Biner, D.; Krämer, K. W.; Dunham, S. T.; De Yoreo, J. J.; Gamelin, D. R. Defect Structure in Quantum-Cutting Yb^{3+}-Doped $CsPbCl_3$ Perovskites Probed by X-Ray Absorption and Atomic Pair Distribution Function Analysis. *Phys. Rev. Mater.* **2022**, 6 (7), 074601. https://doi.org/10.1103/PhysRevMaterials.6.074601.

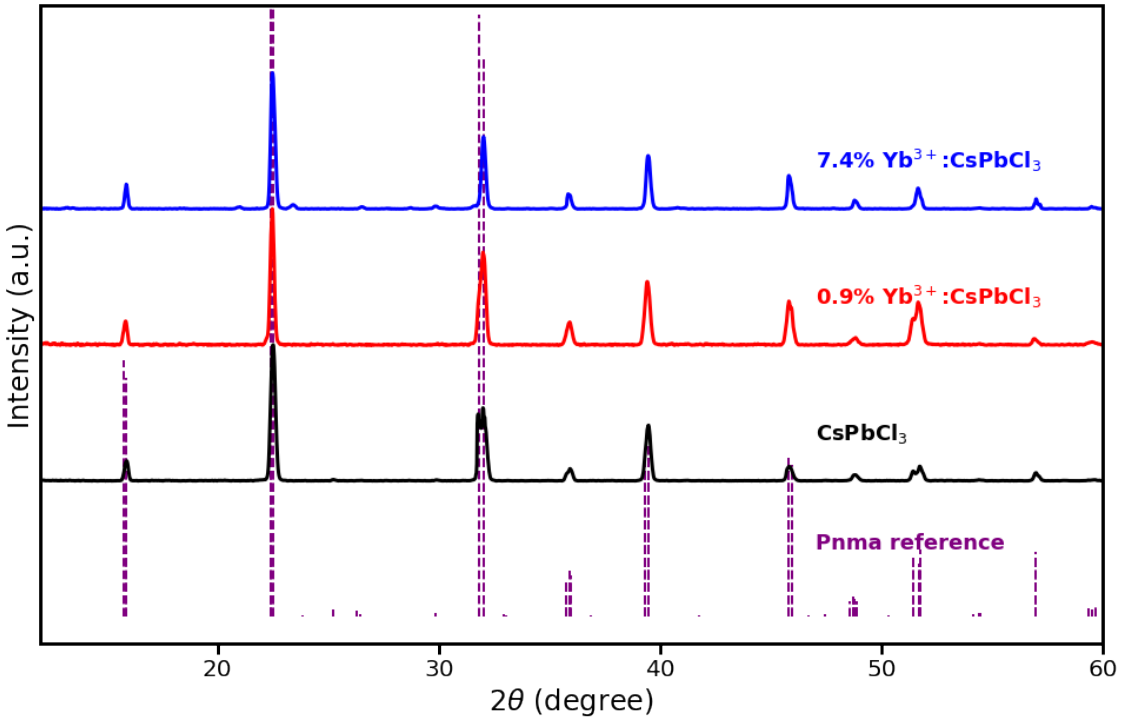

Figure A.1: Powder XRD of powdered single-crystal samples. $CsPbCl_3$ Pnma reference is shown for comparison. XRD shows the same periodic structure between the undoped and Yb^{3+}-doped samples. Small peaks in the 7.4% sample, most notably between 20° and 30°, primarily correspond to the Pnma reference structure. Peaks above and below the major peak at 22°, however, indicate a reduced cell symmetry and possible twinning resulting from higher doping.

Table A.1: Fitting parameters and bond distances for optimized EXAFS shell-by-shell fits of each DFT Yb^{3+} defect structure to the 7.4% Yb^{3+}:$CsPbCl_3$ single-crystal Yb L_3 edge EXAFS data. The number of chloride single scattering pathways (Cl SS paths) considered for each fit is based on the predicted Yb^{3+} site structure. The linear $[Yb_{Pb}\text{-}V_{Pb}\text{-}Yb_{Pb}]^0$ structure has 3 distinct Cl single scattering pathways, the bent $[Yb_{Pb}\text{-}V_{Pb}\text{-}Yb_{Pb}]^0$ and $[Yb_{Pb}\text{-}V_{Pb}]^-$ have 2, and the $[Yb_{Pb}]^+$ has only 1.

7.4% Yb^{3+}:$CsPbCl_3$	Fit Parameters				Cl SS paths	
Defect	R factor	χ^2	χ^2_{red}	Debye-Waller	Coordination Number	Bond distance (Å)
$[Yb_{Pb}]^+$	0.044	2255	444	0.013	6	2.55
$[Yb_{Pb}\text{-}V_{Pb}]^-$	0.027	1402	344	0.009	1 5	2.35 2.55
$[Yb_{Pb}\text{-}V_{Pb}\text{-}Yb_{Pb}]^0$ (linear)	0.030	1539	430	0.009	1 4 1	2.34 2.53 2.59
$[Yb_{Pb}\text{-}V_{Pb}\text{-}Yb_{Pb}]^0$ (bent)	0.030	1552	339	0.010	1 5	2.34 2.55

Table A.2: Fitting parameters and bond distances for optimized EXAFS shell-by-shell fits of each DFT Yb^{3+} defect structure to the 0.9% Yb^{3+}:$CsPbCl_3$ single-crystal Yb L_3 edge EXAFS. The number of chloride single scattering pathways (Cl SS paths) considered for each fit is based on the predicted Yb^{3+} site structure.

0.9% Yb^{3+}:$CsPbCl_3$	Fit Parameters				Cl SS paths	
Defect	R factor	χ^2	χ^2_{red}	Debye-Waller	Coordination Number	Bond distance (Å)
$[Yb_{Pb}]^+$	0.031	643	145	0.020	6	2.52
$[Yb_{Pb}\text{-}V_{Pb}]^-$	0.021	434	127	0.016	1 5	2.31 2.52
$[Yb_{Pb}\text{-}V_{Pb}\text{-}Yb_{Pb}]^0$ (linear)	0.018	365	118	0.009	1 4 1	2.35 2.55 2.38
$[Yb_{Pb}\text{-}V_{Pb}\text{-}Yb_{Pb}]^0$ (bent)	0.020	507	124	0.016	1 5	2.31 2.52

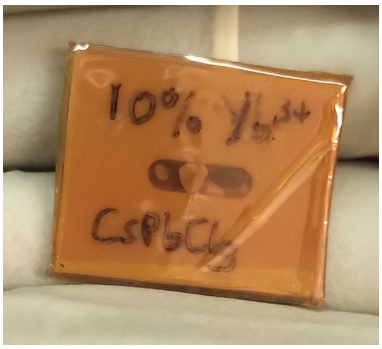

Figure A.2: Photograph of 7.4% Yb^{3+}:$CsPbCl_3$ single-crystal sample sealed in a Teflon mount for air-free EXAFS measurements. The crystal's edge lengths are ca. 1.5 mm. The crystal is centered in the Teflon mount, in the center of the image. $CsPbCl_3$ and 0.9% Yb^{3+}:$CsPbCl_3$ samples were mounted similarly.

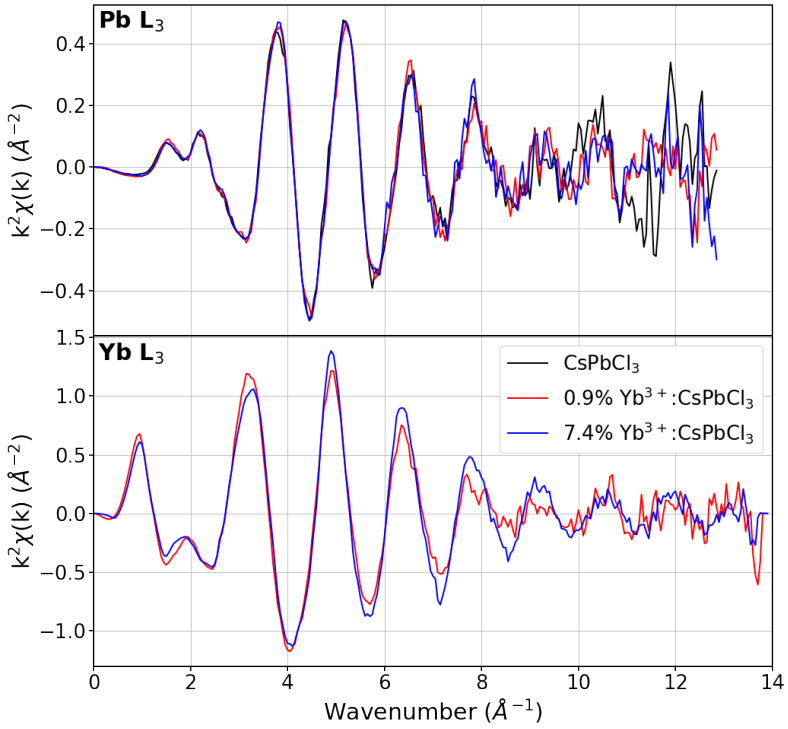

Figure A.3: k-space EXAFS spectra from the Pb L_3 (top) and Yb L_3 (bottom) edges for $CsPbCl_3$ (black), 0.9% (red), and 7.4% (blue) Yb^{3+}:$CsPbCl_3$ single-crystal samples, plotted with a k-weight of 2. A window from 2.5 $Å^{-1}$ to 11 $Å^{-1}$ with a dk value of 1 $Å^{-1}$ was used for shell-by-shell fitting in Artemis. The Yb L_3 signals were weaker for the 0.9% sample than the 7.4% sample.

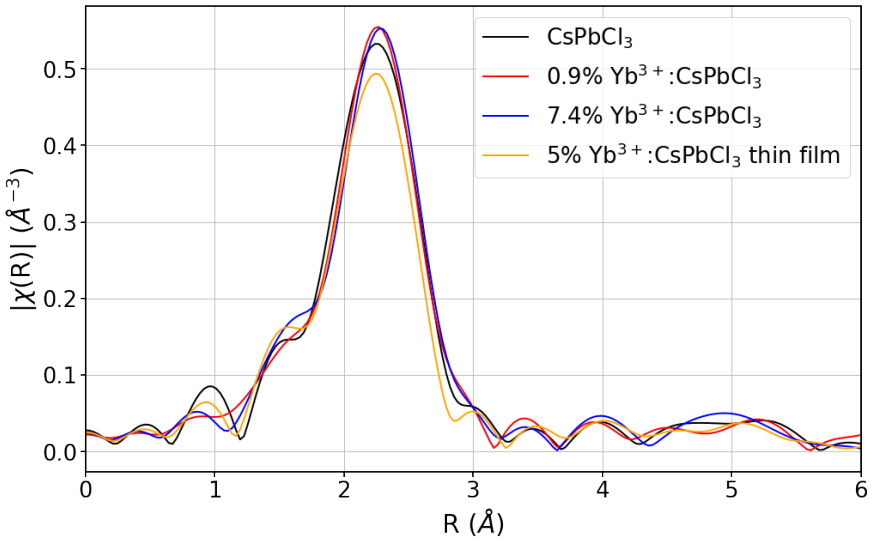

Figure A.4: Fourier-transform (real space) EXAFS spectra from the Pb L_3 edge for undoped $CsPbCl_3$, 0.9% and 7.4% Yb^{3+}-doped $CsPbCl_3$ single crystals, and a 5% Yb^{3+}-doped $CsPbCl_3$ evaporated thin film. The data all show the same peak, indicating that the average Pb^{2+} local environment does not change upon Yb^{3+} doping. Furthermore, no difference was observed between the thin film and the single crystals, indicating that surface sites have no measurable effect on the Pb^{2+} local environment.

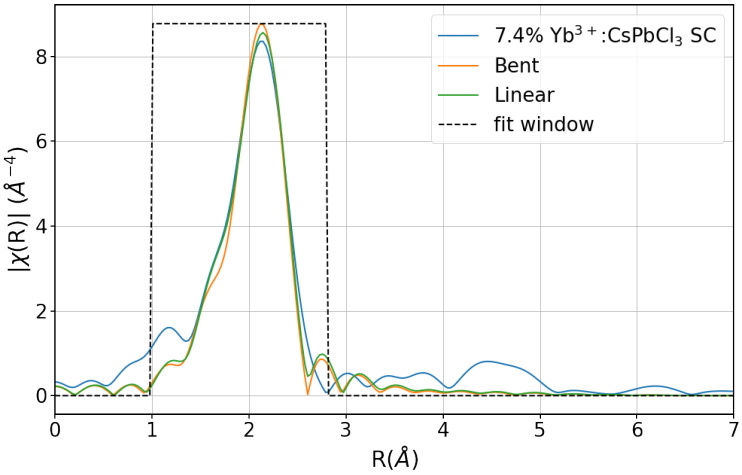

Figure A.5: Optimized EXAFS shell-by-shell fits of the two computed $[Yb_{Pb}\text{-}V_{Pb}\text{-}Yb_{Pb}]^0$ dimer structures to 7.4% Yb^{3+}:$CsPbCl_3$ single-crystal Yb L_3 edge EXAFS data. All fits were performed using the nearest-neighbor Cl^- single scattering paths only, calculated with FEFF. The fitting procedure was insensitive to the starting configuration, suggesting that either configuration is equally likely in the data. Variations between the dimer fits are within the normal fit variation parameters, particularly when accounting for the goodness of fit parameters. This result indicates that neither structure is a better fit to the data than the other. The fitting window was chosen to encompass only the primary Cl^- peak in the data. Additional fits using an extended window and additional scattering paths yielded poorer results (not shown).

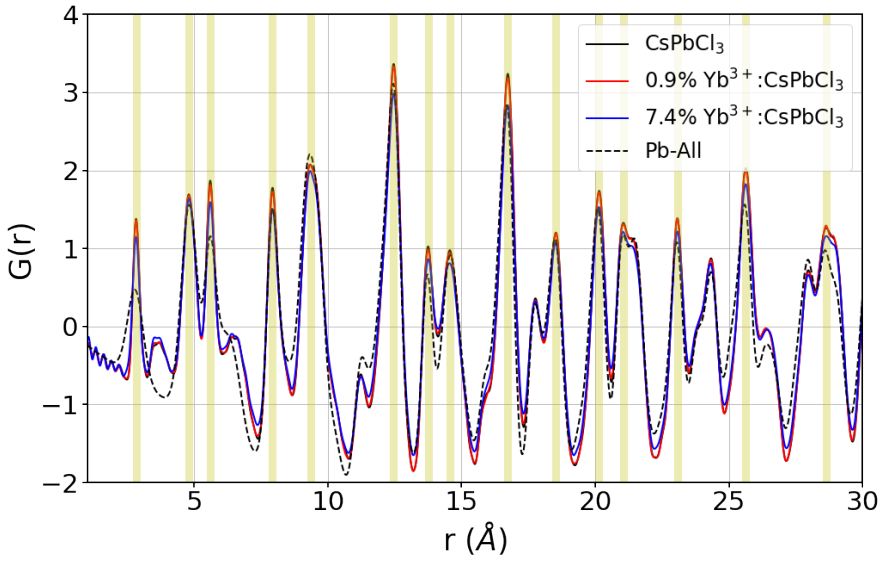

Figure A.6: PDF profiles for all powdered single-crystal samples plotted alongside the calculated Pb-atom partial PDF (Pb-All). Pb-All represents all atom pairs that include a Pb^{2+} site in the idealized $CsPbCl_3$ Pnma structure. Pb-related peaks that show a change in intensity upon Yb^{3+} doping are highlighted in yellow. The Pb partial PDF shown here consistently overlaps the peaks showing intensity changes between the $CsPbCl_3$ and Yb^{3+}-doped $CsPbCl_3$ samples, indicating that these changes come from changes in the B-site Pb^{2+} sublattice.

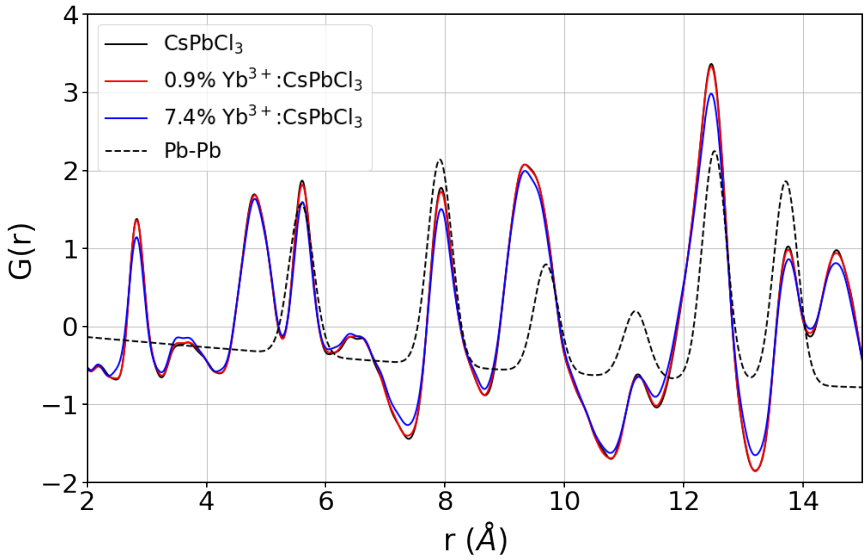

Figure A.7: PDFs of all powdered single-crystal samples plotted alongside the calculated Pb-Pb-pair partial PDF (Pb-Pb). Pb-Pb represents all Pb-Pb ion pairs in the idealized $CsPbCl_3$ Pnma lattice. Note that beyond 6 Å (limit of short-range order in this material), peak intensities may include contributions from Pb-Pb pairs but are not solely dependent on them. The Pb-Pb partial PDF was used to select peaks for analysis of Pb^{2+} vacancies resulting from Yb^{3+} doping.

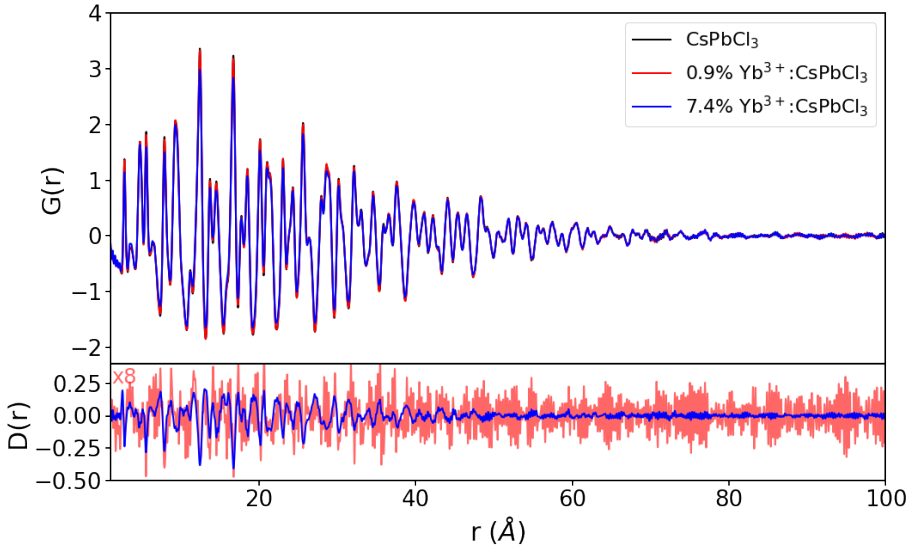

Figure A.8: Full r-range PDFs and dPDFs for $CsPbCl_3$, 0.9% Yb^{3+}:$CsPbCl_3$, and 7.4% Yb^{3+}:$CsPbCl_3$ powdered single-crystal samples. 0.9% D(r) data have been scaled by a factor of 8 to account for the difference in Yb^{3+} doping. The data show a drop-off in peak intensity beginning around 20 Å , attributed to the increasing contribution of surfaces in these powders.

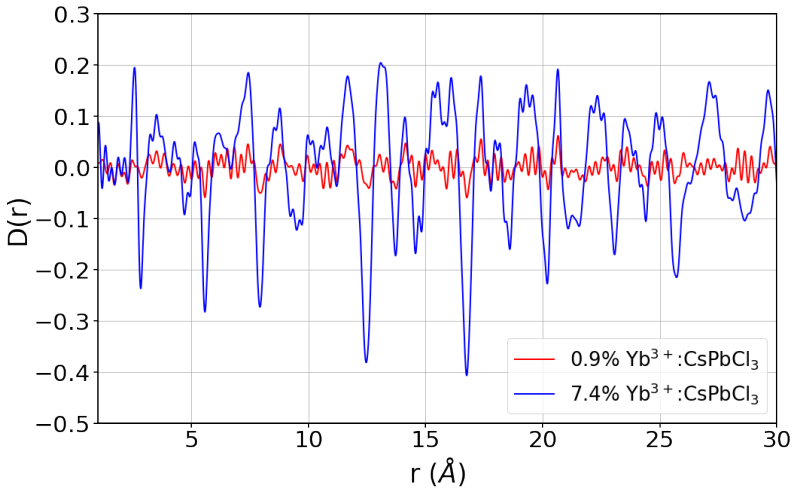

Figure A.9: Unscaled differential PDFs (dPDF, D(r)) of the 0.9% and 7.4% Yb^{3+}:$CsPbCl_3$ powdered single-crystal samples, plotted from 2 to 30 Å . The 0.9% data show substantially greater Fourier noise due to much smaller differences between these and the undoped $CsPbCl_3$ data.

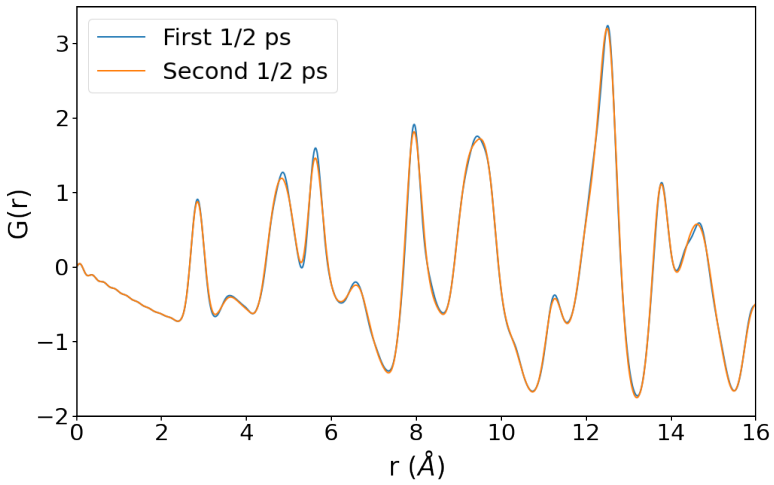

Figure A.10: Comparison of PDF profiles calculated from first (blue) and second (orange) halves of a 1 ps AIMD trajectory of a DFT-optimized $CsPbCl_3$ structure. The two time slices were compared to check for possible sampling bias within the trajectory.

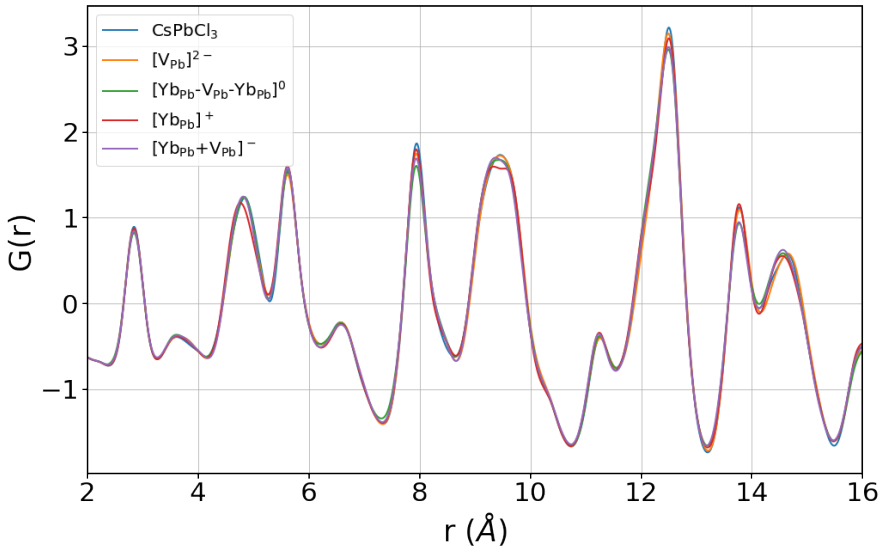

Figure A.11: Calculated PDFs based on 1 ps AIMD trajectories of DFT-optimized Yb^{3+}-induced defect structures. Curves for the two $[Yb_{Pb}\text{-}V_{Pb}\text{-}Yb_{Pb}]^0$ dimer structures shown in main-text Figure 3 were averaged into a single structure for ease of simulation. An additional Pb vacancy defect, $[V_{Pb}]^{2-}$, is included for comparison.

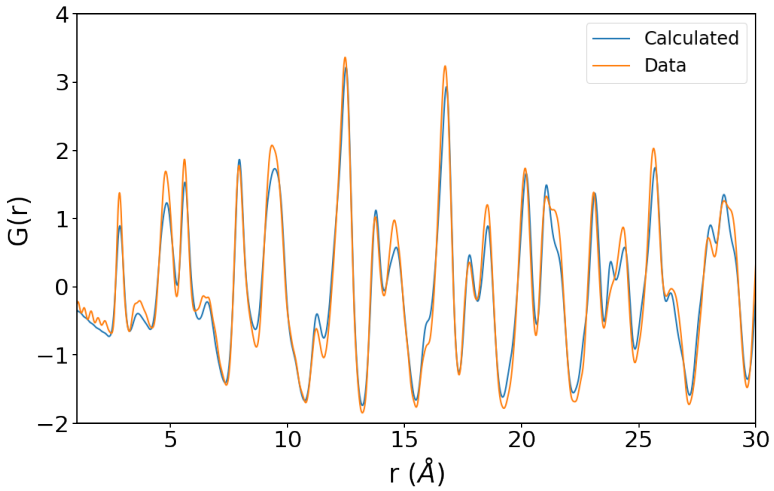

Figure A.12: Calculated $CsPbCl_3$ PDF from a 1 ps AIMD trajectory of the DFT-optimized bulk structure (blue), plotted alongside the experimental data for the $CsPbCl_3$ powdered single-crystal sample. The peak positions are reproduced by the calculations, with slight inaccuracies in the peak shapes and intensities.

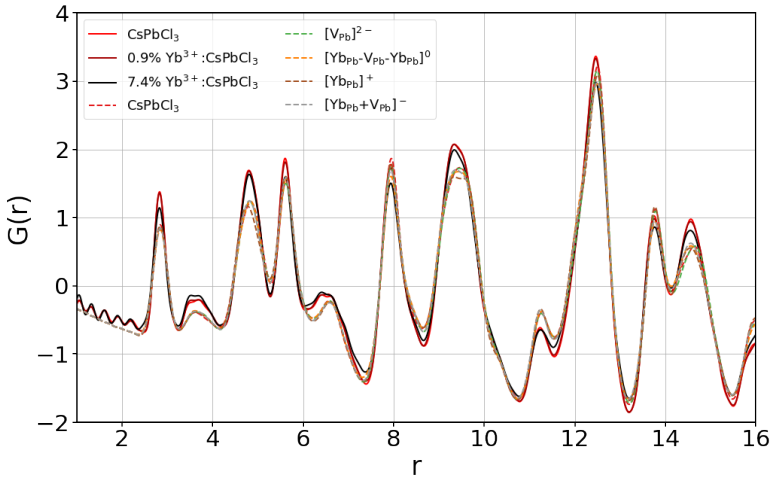

Figure A.13: Calculated PDFs based on 1 ps AIMD trajectories of DFT-optimized Yb^{3+}-induced defect structures (dashed lines) alongside PDF data collected for $CsPbCl_3$ and 0.9% and 7.4% Yb^{3+}:$CsPbCl_3$ samples.

Appendix B

SUPPLEMENTAL MATERIAL FOR: STRUCTURE AND STABILITY OF THE IODIDE ELPASOLITE, CS_2AGBII_6

Table B.1: Residuals after last Rietveld refinement for each structure considered here.

		Reduced χ^2		
Structure	R_w	250 mm	1000 mm	1500 mm
Fm-3m	7.8	2.5478	2.1691	2.3527
I4-m	6.7	1.7386	1.6154	1.7935
R-3m	13.7	6.0920	6.5109	7.7594

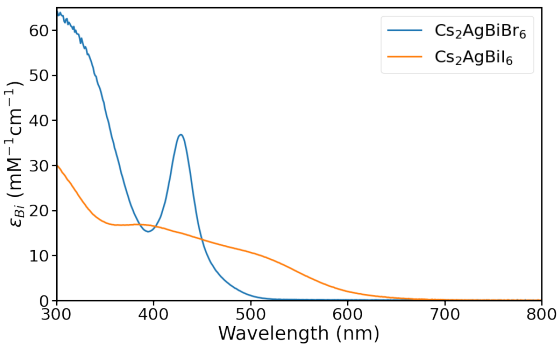

Figure B.1: Absorbance of $Cs_2AgBiBr_6$ nanocrystals (blue) and anion-exchanged Cs_2AgBiI_6 nanocrystals (orange) used for X-ray total scattering measurements. Note that there is some uncertainty in the precise extinction coefficients due to potential error in determination of the Bi^{3+} concentrations.

Table B.2: Water contents of select compounds and solvents measured using Karl-Fischer titration.

Reagent	Hexanes (dry)	Hexanes	Benzyl Alcohol	Oleic Acid	Oleylamine	DDDMABr
Water Content (ppm)	0.0	58.3	86	74.2	86.1	13.4

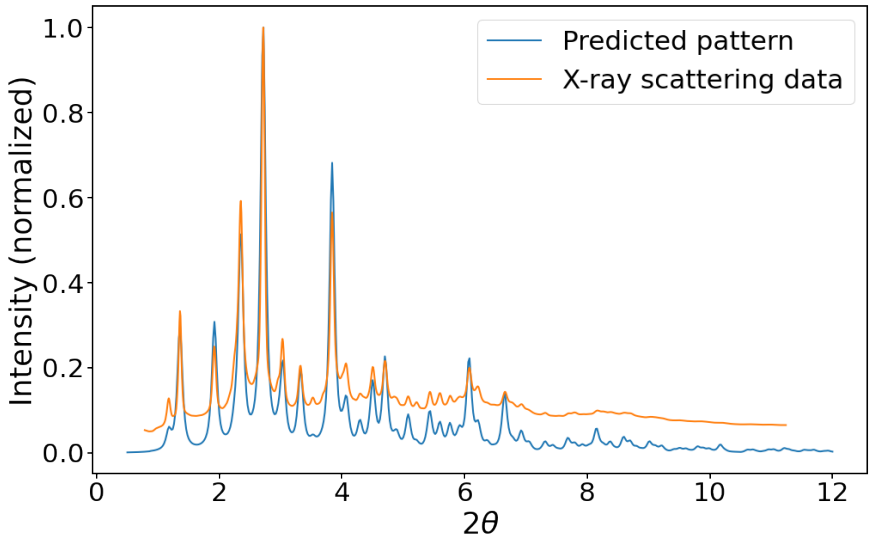

Figure B.2: X-ray scattering data (orange) collected for Cs_2AgBiI_6 nanocrystals in hexanes compared with predicted scattering pattern (blue) from a simple cubic (Fm3m) model made by replacing Br in $Cs_2AgBiBr_6$ with I and expanding the unit cell.

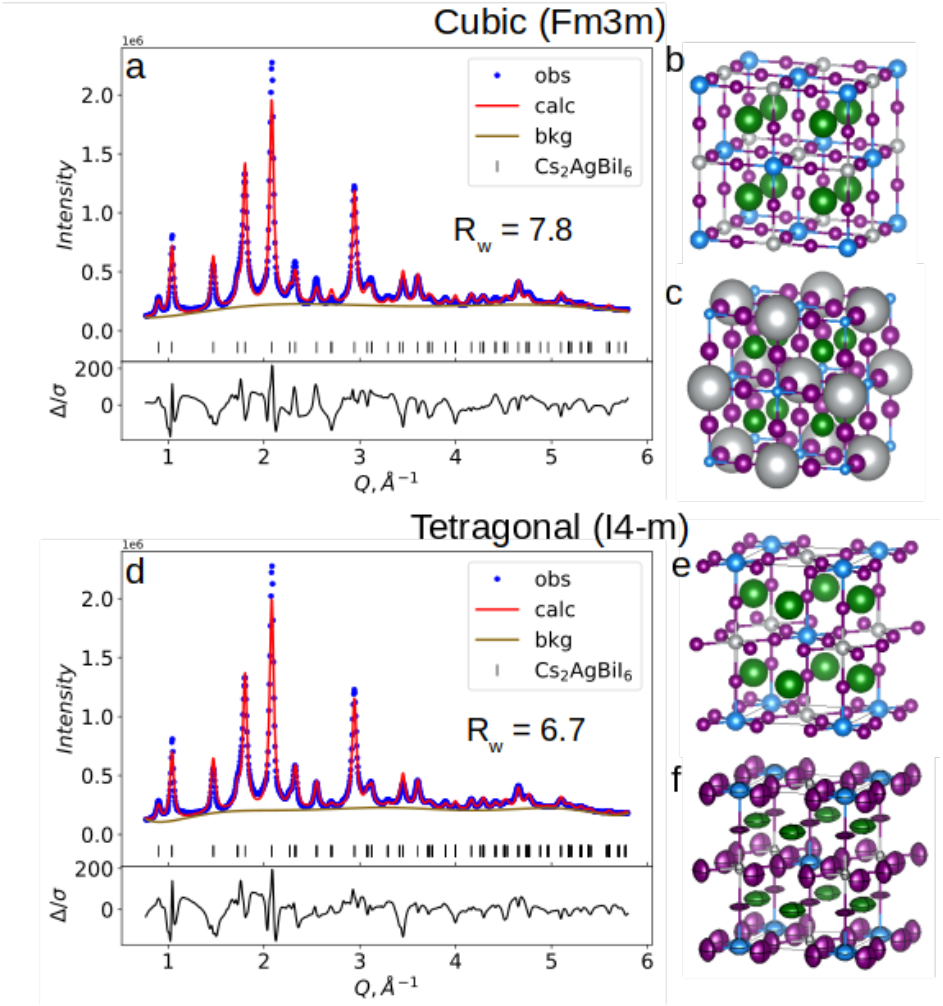

Figure B.3: Comparison of Rietveld refinement results using synchrotron X-ray scattering data for Cs_2AgBiI_6 nanocrystals in hexanes solution. (a) Data (blue dots), calculated pattern (red curve), background (brown curve), predicted peak positions (vertical black lines), and residual of fit (Δ/σ) obtained using cubic Fm-3m structure. R_w is the overall weighted R-factor for the refinement. (b) Cubic Fm-3m structure model. Silver: Ag^+; blue: Bi^{3+}; green: Cs^+; purple: I^-. (c) Structure model produced from (a) showing 95% atomic displacement parameters (ADPs). Note the very large displacements of Ag^+ atoms (0.45 Å). (d) Data (blue dots), calculated pattern (red curve), background (brown curve), predicted peak positions (vertical black lines), and residual of fit (Δ/σ) obtained using tetragonal I4-m structure. (e) Tetragonal I4-m structure model. (f) Structure model produced from (e) showing 95% ADPs refined using PDF data.

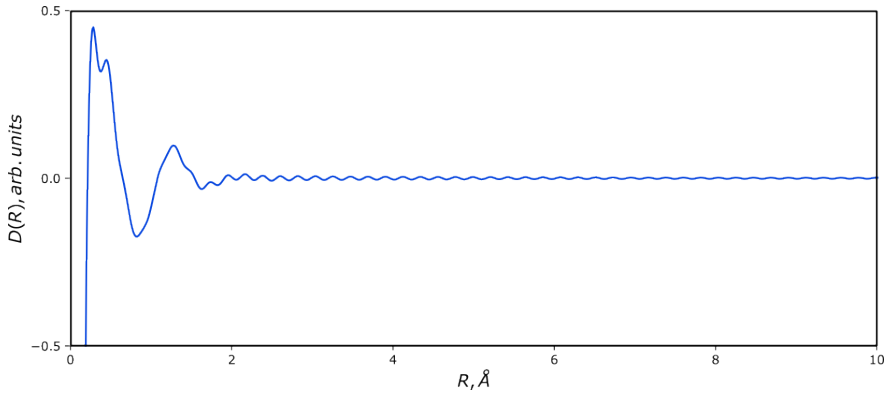

Figure B.4: Example radial distribution function of the residuals from the Rietveld refinements. The two prominent peaks are below 2 Å , indicating no significant contribution of the elpasolite or secondary crystalline phases. The broad peak between 1 and 2 Å likely corresponds to C-C, C-O, and C-N atom pairs of the ligands and the ligand-solvent interface.

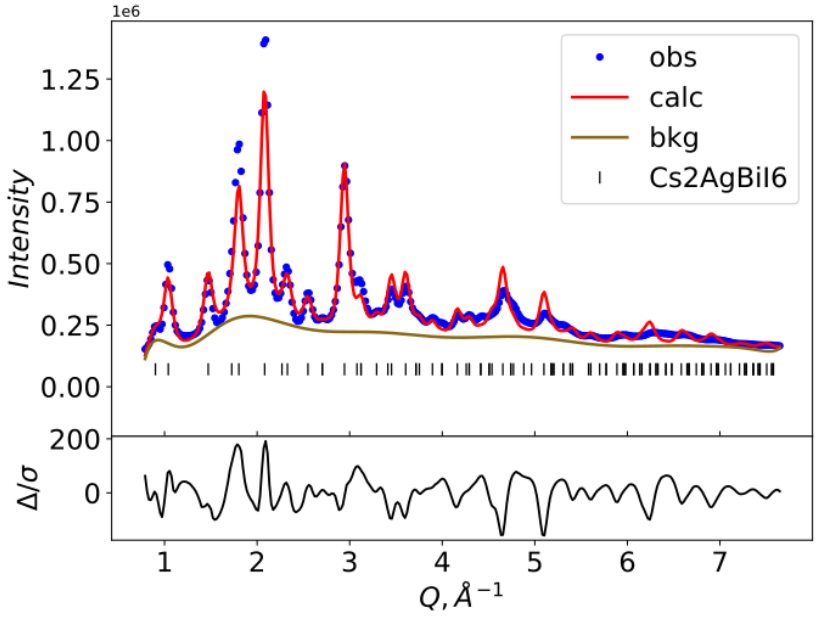

Figure B.5: Rietveld refinement results using synchrotron X-ray scattering data. Data, calculated pattern, background, predicted peaks, and residual of fit using cubic Fm-3m structure with Ag U_{iso} parameter reset to 0.02 and not refined. Weighted residual R_w = 12.9. Note additional peaks in the residual.

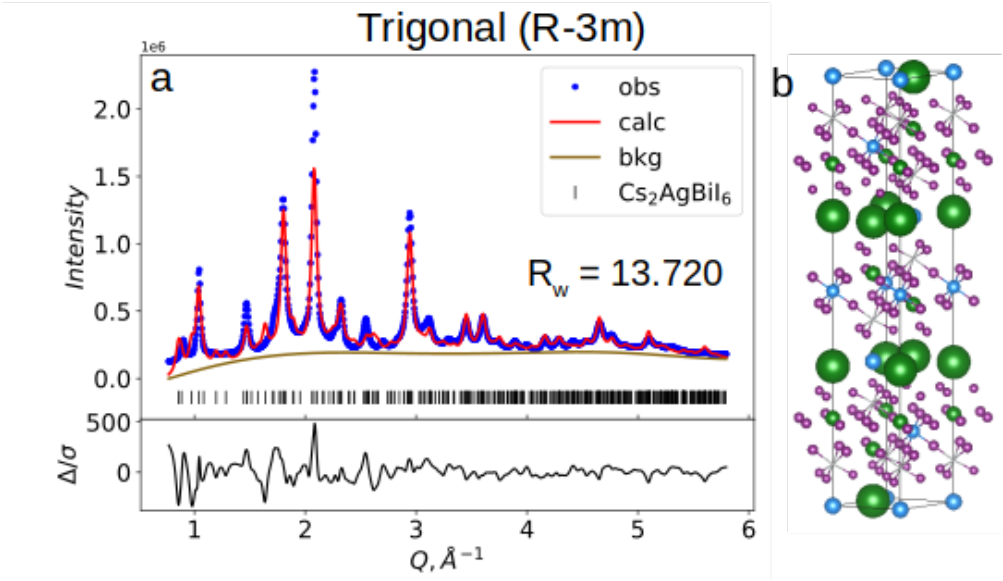

Figure B.6: Rietveld refinement results using synchrotron X-ray scattering data. (a) Data, calculated pattern, background, predicted peaks, and residual of fit using trigonal R-3m structure. Weighted residual $R_w = 13.7$. (b) Trigonal structure model showing 95% atomic displacement parameters (ADPs) from fit. Silver: Ag^+; blue: Bi^{3+}; green: Cs^+; purple: I^-.

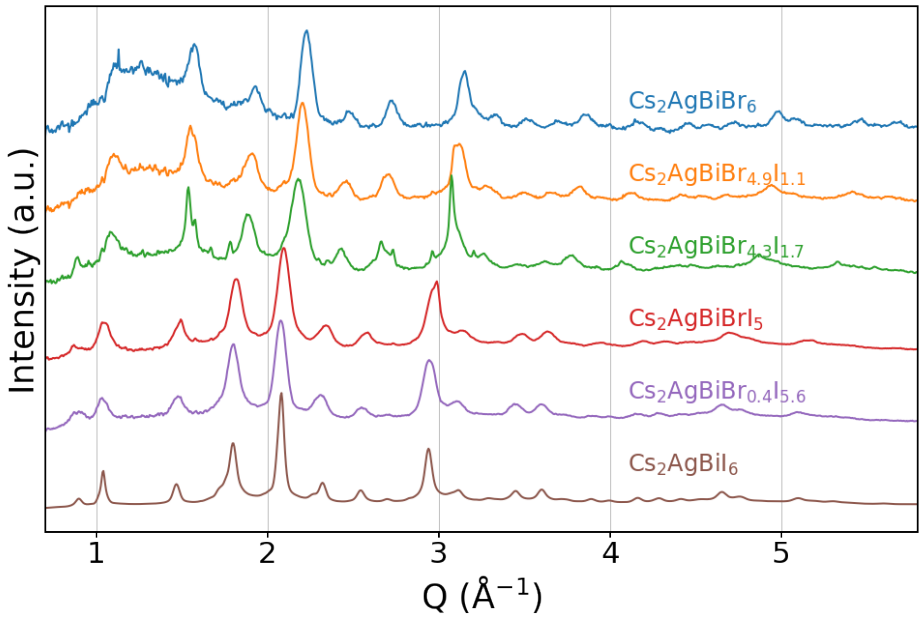

Figure B.7: Synchrotron XRD patterns for each sample in a series from Cs_2AgBiI_6 to Cs_2AgBiI_6 plotted in Q-space. Greater noise in the $Cs_2AgBiBr_6$, $Cs_2AgBiBr_{4.3}I_{1.7}$, and $Cs_2AgBiBr_{4.9}I_{1.1}$ patterns is due to the lower signal-to-noise ratio for those samples. Weighted residuals for each fit from $Cs_2AgBiBr_6$ to $Cs_2AgBiBr_{0.4}I_{5.6}$, respectively: R_w = 7.84, 8.32, 9.86, 6.68, 6.06.

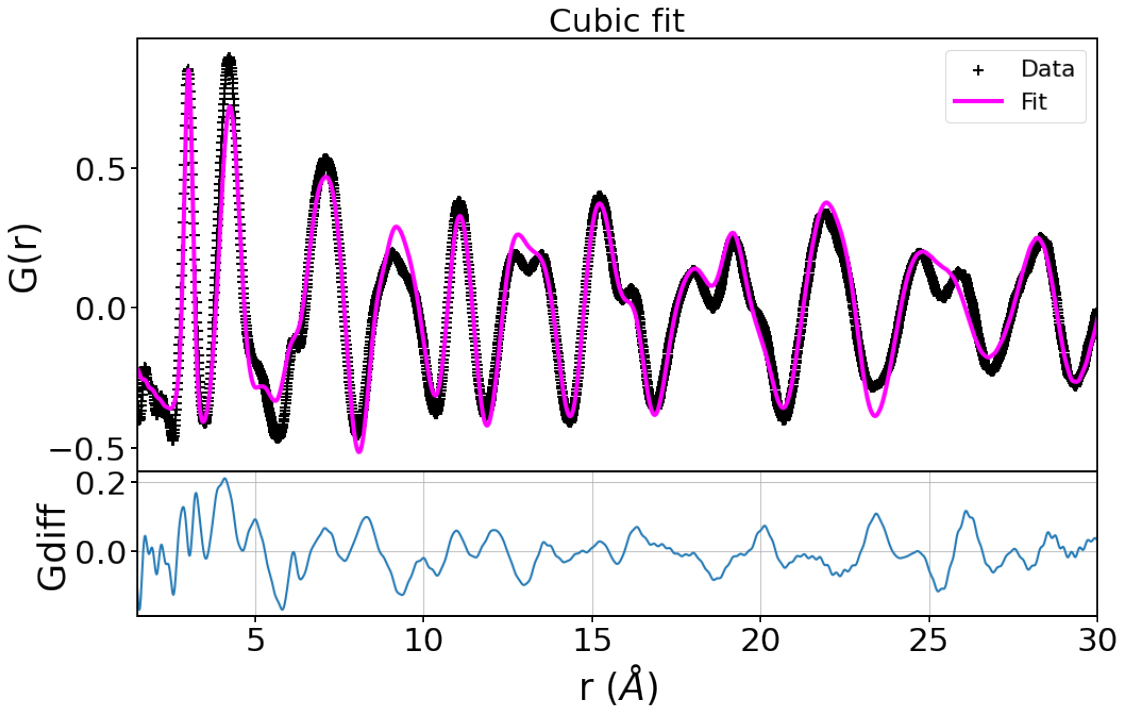

Figure B.8: Real-space fit to the Cs_2AgBiI_6 PDF data using a cubic (Fm-3m) structural model, run using pdfgui. Gdiff shows the difference between the fit and the data. R_w = 0.227, reduced $\chi^2 = 0.0035$.

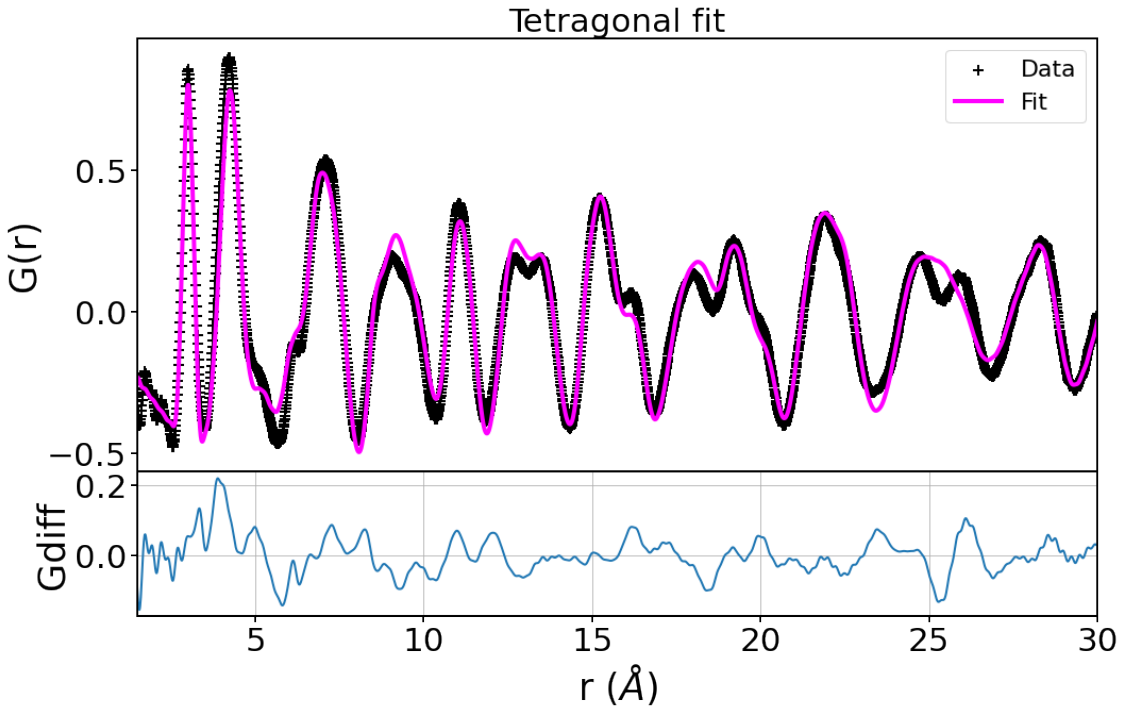

Figure B.9: Real-space fit to the Cs_2AgBiI_6 PDF data using a tetragonal (I4-m) structural model, run using pdfgui. Gdiff shows the difference between the fit and the data. R_w = 0.207, reduced $\chi^2 = 0.0030$.

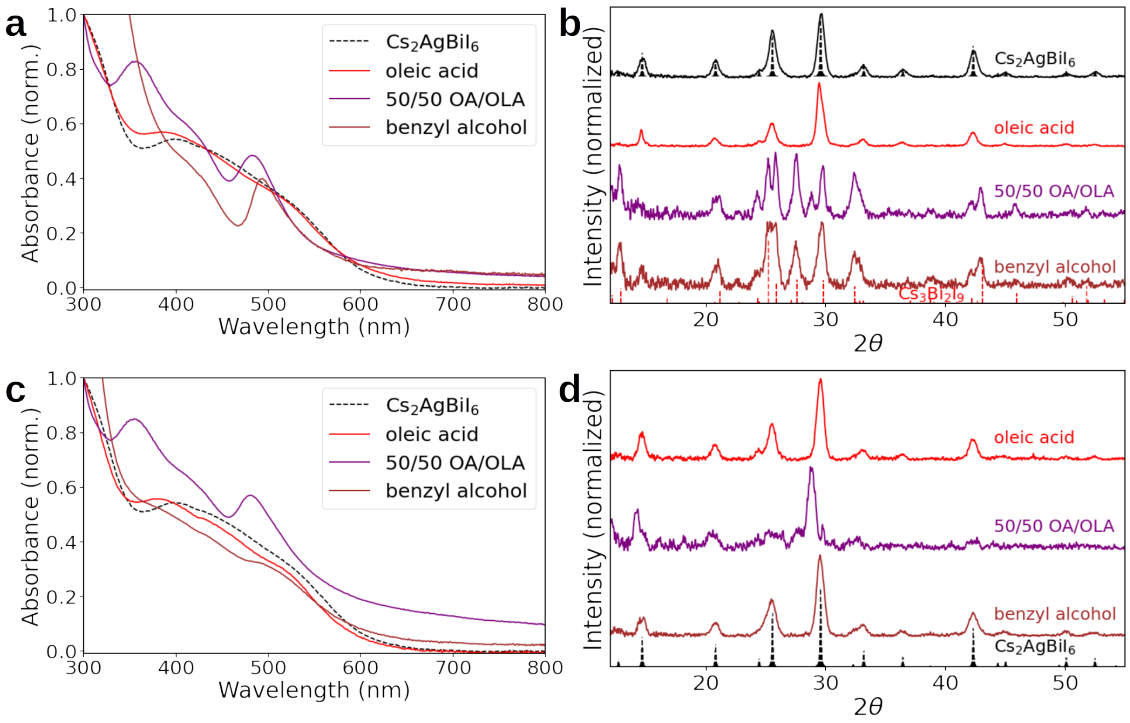

Figure B.10: Absorption spectra and XRD patterns for Cs_2AgBiI_6 nanocrystals exposed to oleic acid, 50:50 (mol %) oleic acid (OA) and oleylamine (OLA), and benzyl alcohol. (a,b) Data from samples in which $Cs_2AgBiBr_6$ nanocrystals were first converted to Cs_2AgBiI_6 by anion exchange, and the resulting Cs_2AgBiI_6 nanocrystals were then exposed to the respective ligands. (c,d) Data from samples in which $Cs_2AgBiBr_6$ nanocrystals were first exposed to these ligands, and then converted to Cs_2AgBiI_6 (or decomposition products) by anion exchange.

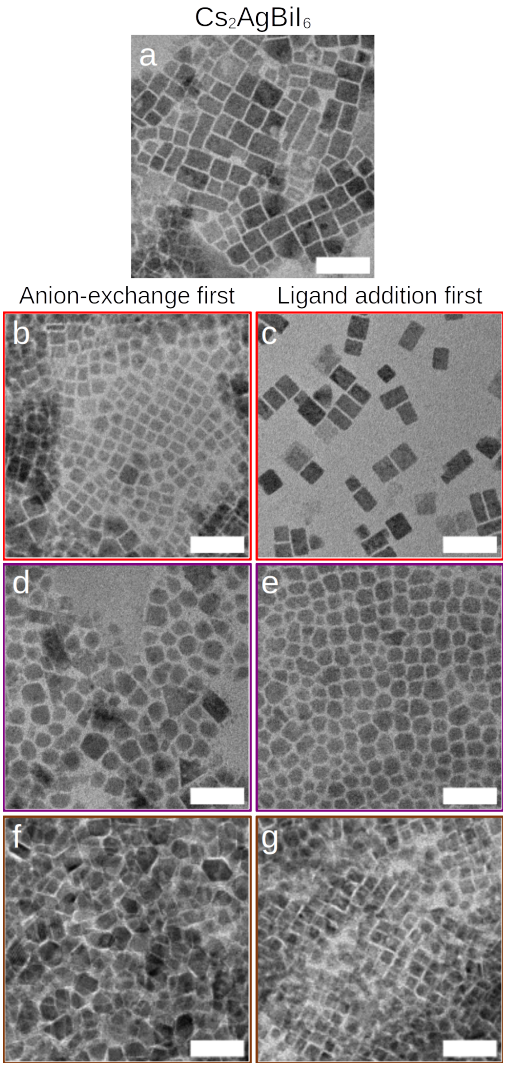

Figure B.11: TEM images of Cs_2AgBiX_6 (X = Br, I) nanocrystals exposed to various small molecules, as described in above Fig. S10. (a) As-made Cs_2AgBiI_6 nanocrystals. (b,d,f) Cs_2AgBiI_6 nanocrystals exposed to organic compounds. (c,e,g) $Cs_2AgBiBr_6$ nanocrystals exposed to organics then subsequently converted to Cs_2AgBiI_6 (or decomposition products) by anion exchange. Organic compounds added are as follows: (b) and (c) oleic acid; (d) and (e) 50:50 mol % OA:OLA; (f) and (g) benzyl alcohol. Scale bars are 50 nm.

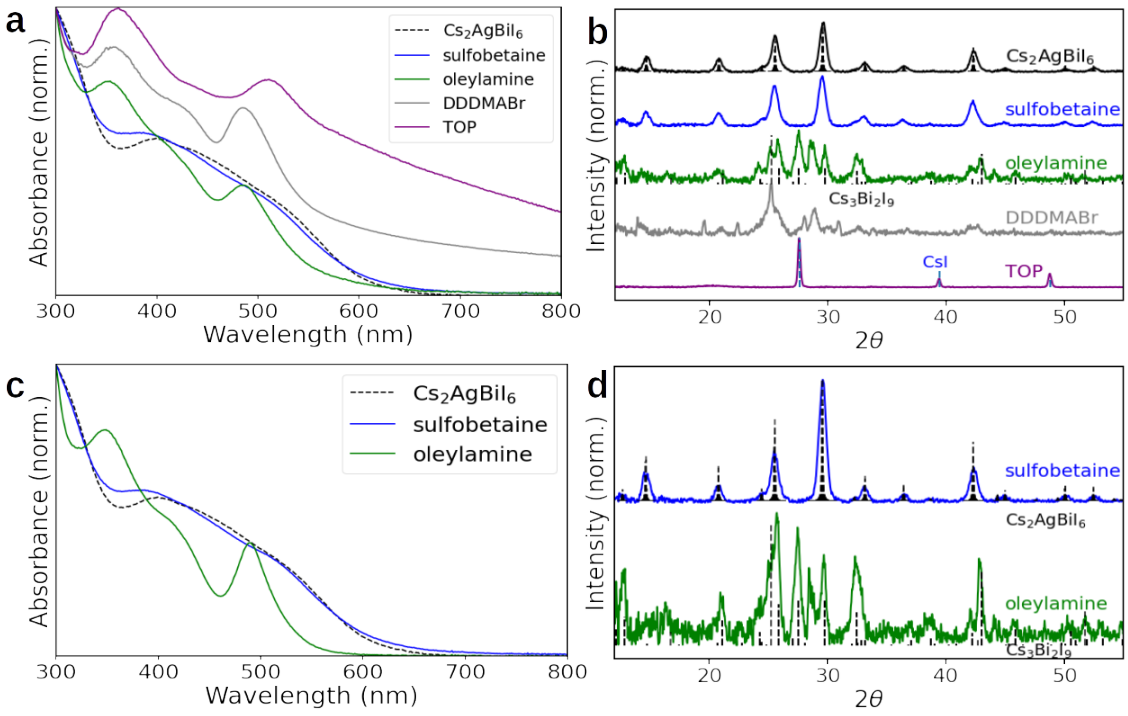

Figure B.12: Absorption (a, c) and XRD (b, d) data for Cs_2AgBiI_6 nanocrystals exposed to sulfobetaine, oleylamine, DDDMABr, and TOP. (a) and (b): Cs_2AgBiI_6 nanocrystals directly exposed to the respective organics. (c) and (d): $Cs_2AgBiBr_6$ nanocrystals exposed to organics, then anion-exchanged to Cs_2AgBiI_6 using a standard anion-exchange procedure.

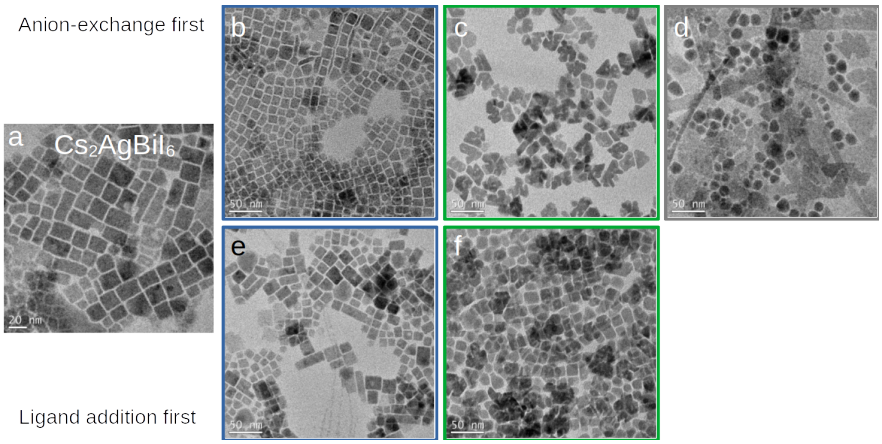

Figure B.13: TEM images of Cs_2AgBiX_6 (X = Br, I) nanocrystals in Fig. B.12. (a) As-made Cs_2AgBiI_6. Top row (b,c,d) Cs_2AgBiI_6 nanocrystals exposed to select small molecules. Bottom row (e,f) $Cs_2AgBiBr_6$ nanocrystals exposed to small molecules then subsequently anion-exchanged to Cs_2AgBiI_6. Small molecules added are as follows: (b) and (e): sulfobetaine; (c) and (f): oleylamine; (d) DDDMABr. Scale bars are 50 nm.

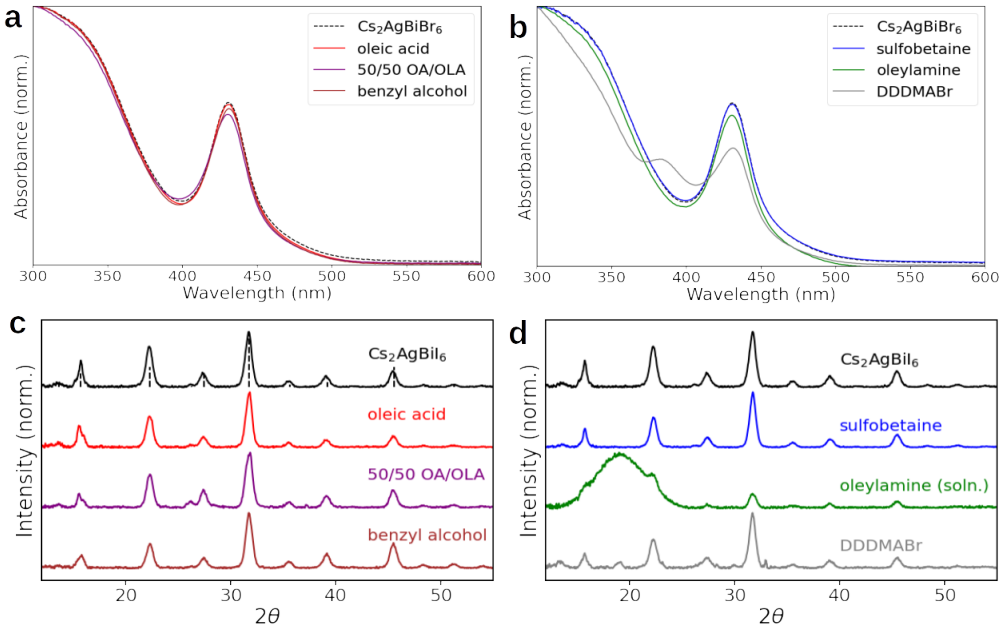

Figure B.14: Absorption (a, b) and XRD (c, d) data for $Cs_2AgBiBr_6$ nanocrystals exposed to various small molecules. (a/c) Oleic acid, 50/50 mol/mol oleic acid (OA) and oleylamine (OLA), and benzyl alcohol. (b/d) sulfobetaine (3-(N,N-dimethyl-octadecylammonio)-propanesulfonate), oleylamine, and DDDMABr (didodecyl-dimethylammonium bromide). Oleylamine data in (d) were measured in solution for a more accurate comparison with anion exchange conditions. It was found that oleylamine-exposed $Cs_2AgBiBr_6$ nanocrystals were unstable once solvent evaporated.

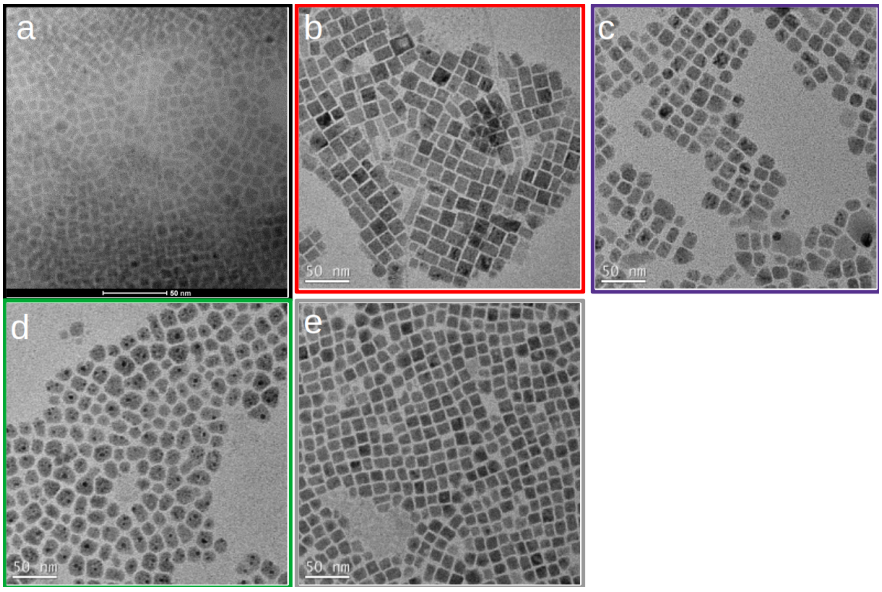

Figure B.15: TEM images of above $Cs_2AgBiBr_6$ nanocrystals exposed to select small molecule compounds. (a) Starting $Cs_2AgBiBr_6$. $Cs_2AgBiBr_6$ exposed to: (b) Oleic acid. (c) 50/50 OA/OLA. (d) OLA. (e) DDDMABr.

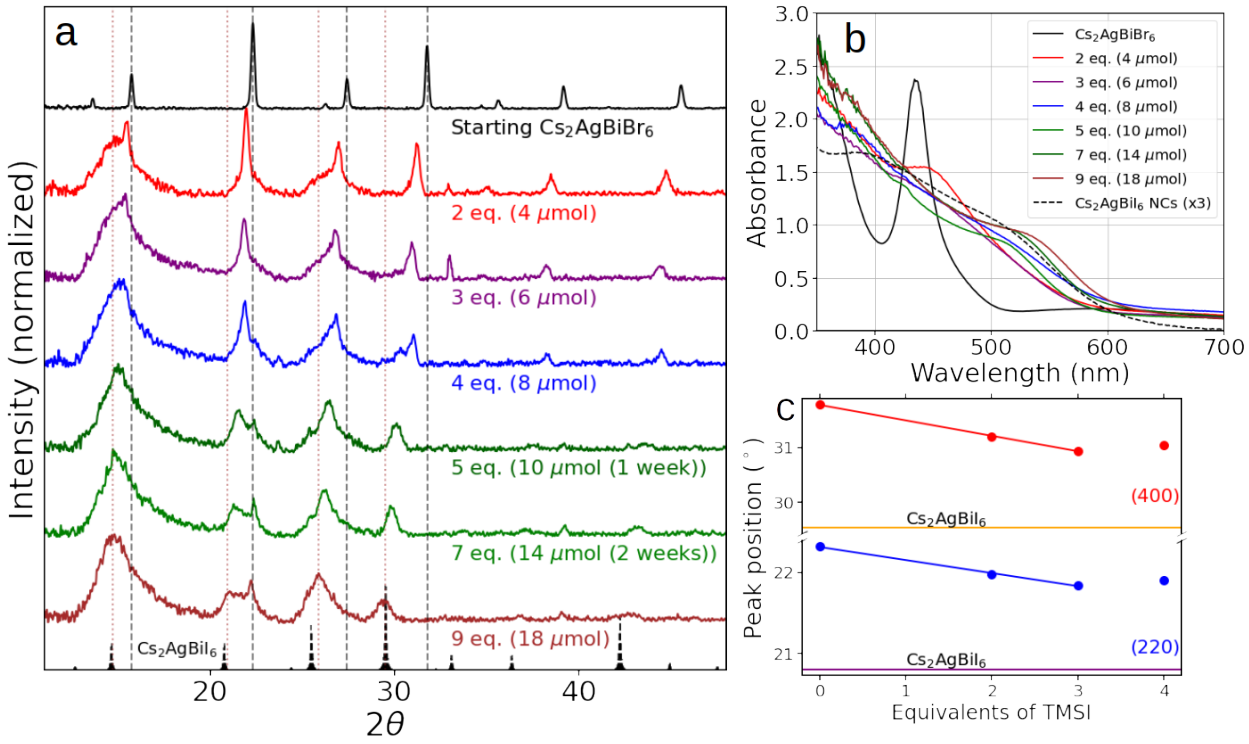

Figure B.16: Gradual anion exchange of a thermally evaporated thin film of $Cs_2AgBiBr_6$ using TMSI vapors. (a) XRD patterns of thin film after each TMSI exposure, given in molar equivalents and µmol quantities. Unless otherwise specified, films were allowed to react for 24 h before stopping the reaction. (b) Absorption spectra of each thin film exposed to identical conditions to those shown in (a). (c) Scatter plot of peak positions of the (400) and (220) peaks in (a) for the first 4 films. A linear trend was observed for the first 2 TMSI additions. After 4 equivalents, it becomes unclear whether the film can still be considered an elpasolite, thus the peaks were not identified.

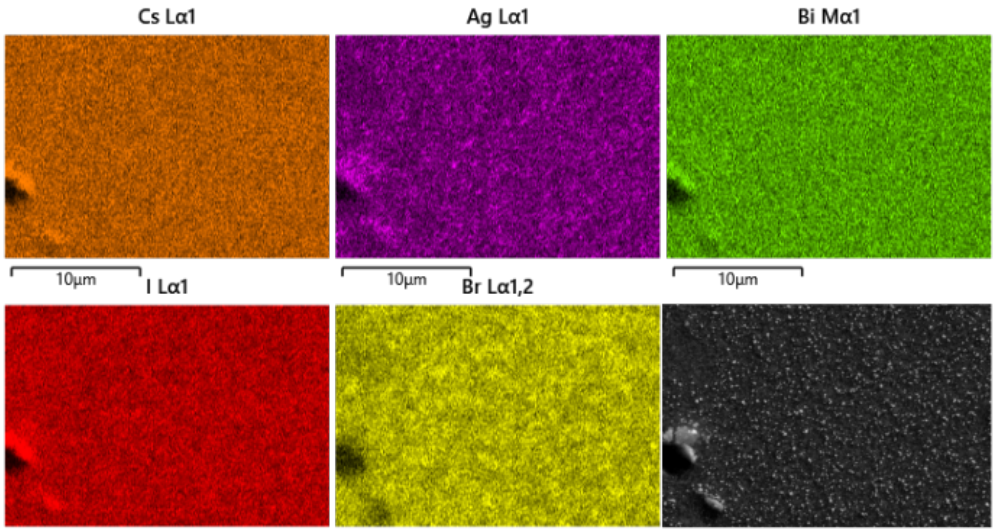

Figure B.17: SEM EDX mapping of final exposure $Cs_2AgBiBr_6$ polycrystalline thin film from slow anion-exchange reaction series. Maps for I, Cs, Br, Bi, and Ag are shown, along with the base SEM image. Grain sizes were observed to be in the range of 100-200 nm.

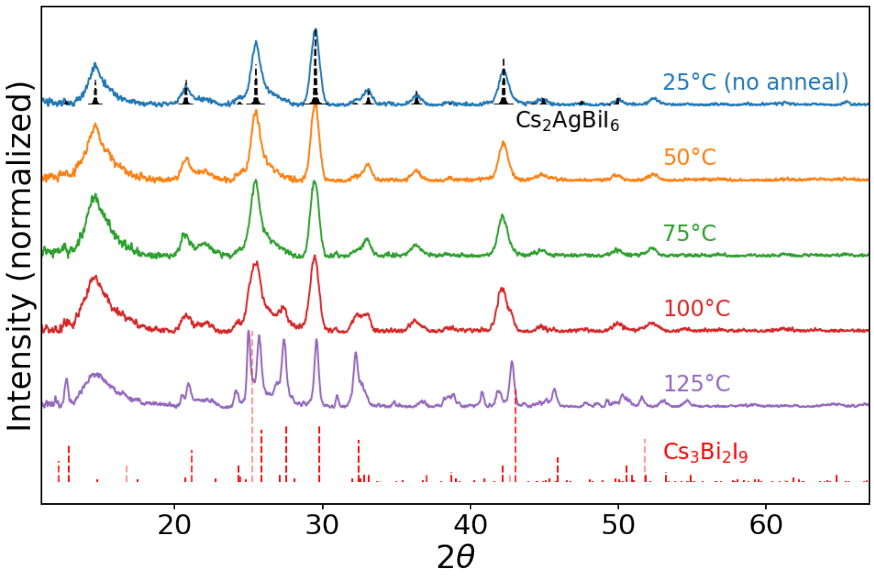

Figure B.18: XRD patterns of Cs_2AgBiI_6 nanocrystal film samples heated to various temperatures under nitrogen atmosphere for 30 min (*ex situ*). Measurements were collected in air promptly after cooling the samples.

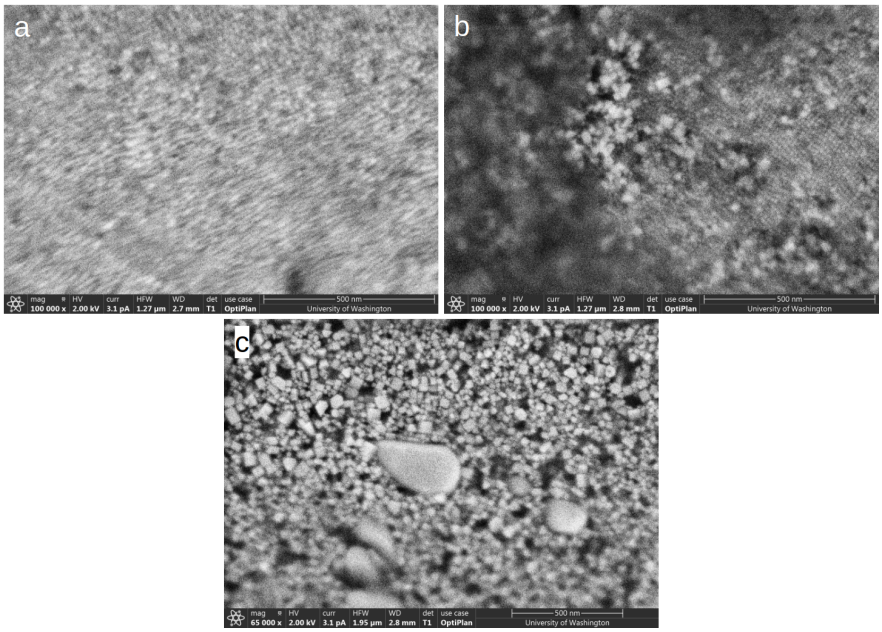

Figure B.19: SEM images of Cs_2AgBiI_6 nanocrystal thin films before (a) and after (b,c) heating (*ex situ*). (a) Initial nanocrystal thin film, with nanoparticles generally too small for SEM to resolve. (b) Same film after heating to 100 °C. Note appearance of some larger particles. (c) Film after heating to 125 °C. A dominant population of larger particles is now observed.

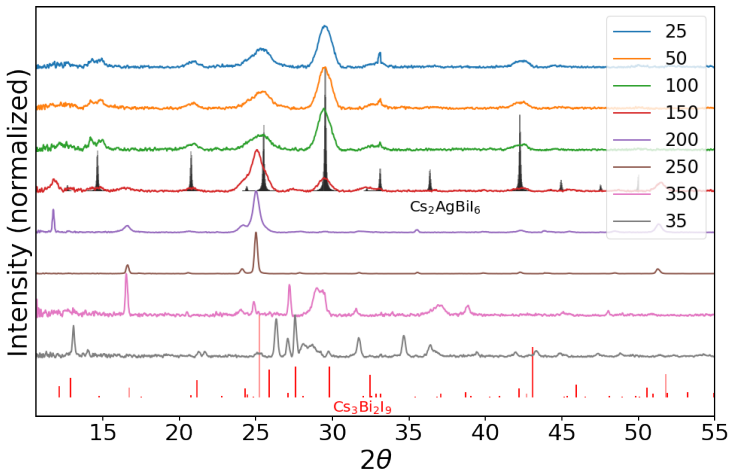

Figure B.20: *In situ* XRD data for a film of Cs_2AgBiI_6 nanocrystals heated in air. The temperature was gradually increased from 25 - 350 °C at a rate of 5 °C/min using a heating stage, then a pattern was measured at steady temperature for ∼10 min. The 35 °C data were collected after the previous heating steps. Reference pattern for $Cs_3Bi_2I_9$ taken from ICSD.

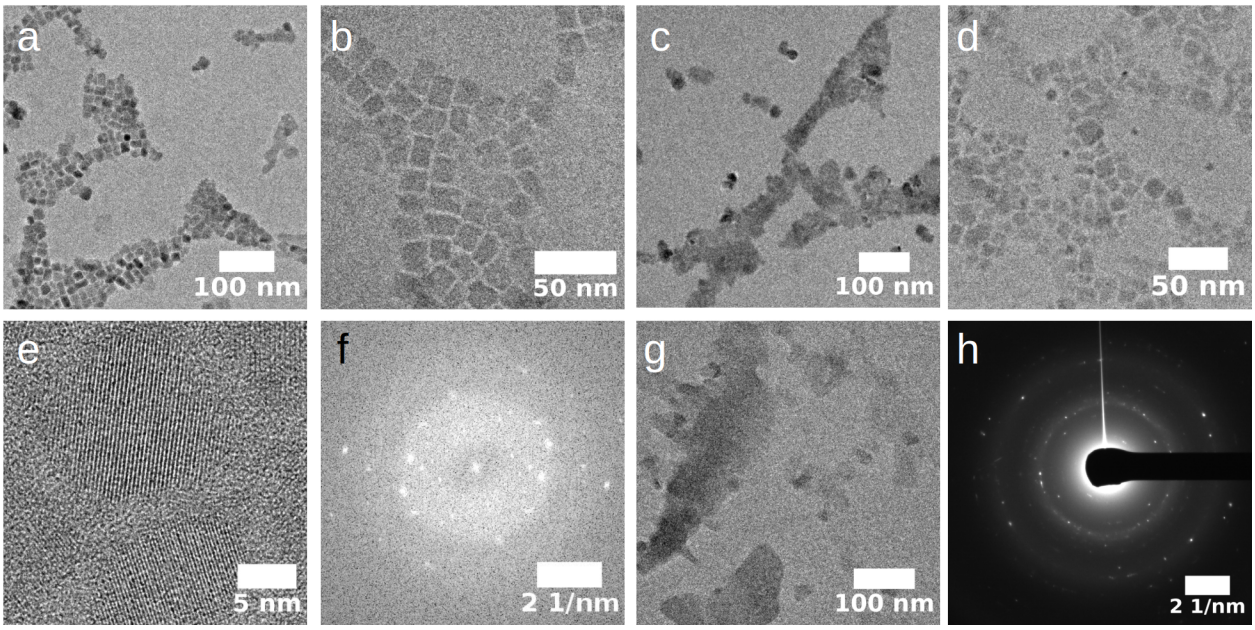

Figure B.21: TEM images of *in situ* heating experiments on Cs_2AgBiI_6 nanocrystals. Sample was heated to 100 °C, held for 10 min, then cooled to 30 °C for imaging. Attempts were made to image at high temperature, but rapid beam damage prevented useful data collection. Various products were observed upon heating: (a) Varied population of NCs, with some sintering while others appear preserved. (b) NCs with preserved morphology after heating. (c) NCs showing evidence of sintering/melting after heating. (d) NCs with persistent morphology after heating to 120 °C. (e) HRTEM of preserved Cs_2AgBiI_6 NCs. (f) FFT of (e), showing elpasolite pattern. (g) Area of NCs that fused upon heating. (h) Electron diffraction of area shown in (g), showing $Cs_3Bi_2I_9$ hexagonal reflections.

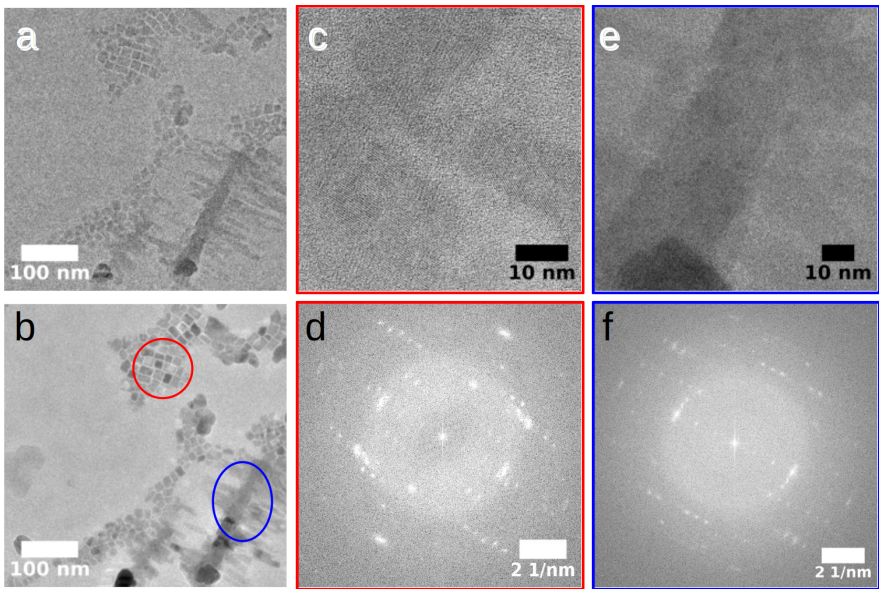

Figure B.22: Additional TEM images of *in situ* heating experiments on Cs_2AgBiI_6 nanocrystals with deliberately broad size distribution, including large branched nanorods. (a) Mixed population of Cs_2AgBiI_6 nanocubes and nanorods prior to heating. (b) The same sample area shown in (a) after heating. (c) HRTEM of individual NCs post-heating. (d) FFT of (c), showing elpasolite pattern. (e) HRTEM image of nanorods post-heating. (f) FFT of (e), showing elpasolite pattern. We were unable to find evidence of correlation between starting NC size and likelihood of transformation during heating.

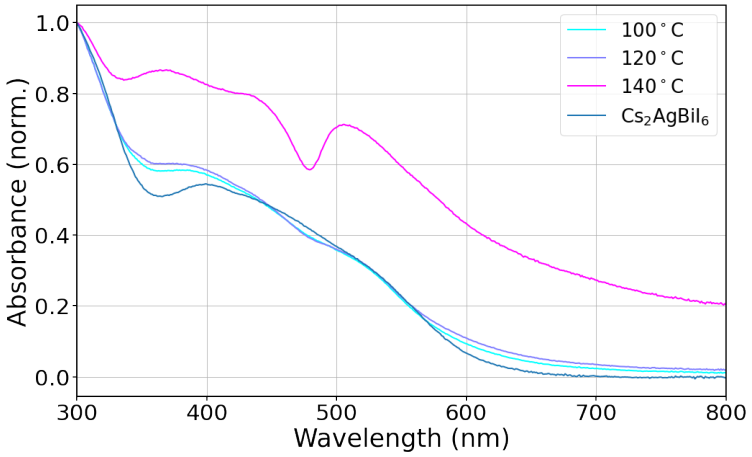

Figure B.23: Absorption spectra of Cs_2AgBiI_6 nanocrystals heated in hexanes solution. Heating to 140 °C resulted in evaporation of hexanes solvent, even in a sealed container.